THE UNIVERSITY OF CHICAGO

TARGETING THE N^6-METHYLADENOSINE PATHWAY FOR CANCER IMMUNOTHERAPY

A DISSERTATION SUBMITTED TO
THE FACULTY OF THE DIVISION OF THE PHYSICAL SCIENCES
IN CANDIDACY FOR THE DEGREE OF
DOCTOR OF PHILOSOPHY

DEPARTMENT OF CHEMISTRY

BY
LINDA ZHANG

CHICAGO, ILLINOIS
AUGUST 2023

Table of Contents

Chapter 4

Chapter 5

List of Figures

List of Tables

Acknowledgements

I am beyond grateful to be a graduate student under the guidance of Prof. Chuan He. Chuan has offered exciting ideas and opportunities and entrusted me to explore new directions. His patience and support led me through many challenges while navigating the projects. Chuan has also connected me with many experts in different fields for collaborations.

I thank all my labmates in the He Lab. I am fortunate to work with talented people who fostered a safe environment for me to learn and grow. Dr. Phillip Hsu was my first mentor in the lab. Phil generously trained me in all the basic experiments I continued to perform throughout my graduate study. I also thank Dr. Zhong Zheng and Dr. Thomas Lu for teaching me mouse handling and immunology experiments. Dr. Zhong Zheng also offered tremendous effort in managing all the experimental mice. I want to thank Dr. Qing Dai for his discussion and help with the inhibitor screening project, Dr. Wenlong Li for optimizing the inhibitor with his expertise in medicinal chemistry, and Dr. Xiaoyang Dou for data analysis. I also thank Dr. Huilung Sun, Dr. Jun Liu, Dr. Chang Liu, Dr. Yu Xiao, and Dr. Tong Wu for helpful scientific discussions and support. I have also shared many enjoyable moments with many lab members, and I greatly appreciate their company.

I also want to thank Dr. Laura Hua Liang and Dr. Liangliang Wang from the Weichselbaum Lab for their expertise in cancer immunology. They provided many valuable suggestions for my intratumoral Treg study. I thank Dr. Anuradha Roy and Dr. David Johnson at the University of Kansas for performing the high-throughput screening and cheminformatics analysis. I am also grateful for the flow cytometry, NGS sequencing, and animal facility staff.

I thank my thesis committee, Prof. Bryan Dickinson and Prof. Ralph Weichselbaum, for their time and suggestions.

I thank my parents for providing the best they could afford and encouraging me to pursue bigger dreams. I thank my sister for being my best role model growing up and the most supportive and understanding friend in the past few years. I am also fortunate to have my cousin's family with me in Chicago. Witnessing the birth of their daughter Chloe and watching her grow up have been the most memorable moments of my time in Chicago. Nan Pon, Matt Zajac, and Cooper Taylor have been my best friends in graduate school since the very first day. Thank you for carrying me through many difficult times and inspiring me with your enthusiasm and optimism. I would also like to thank my friends that I grew up with, who constantly supported me and reminded me to enjoy life outside of the lab.

Abstract

Immune cells, derived from hematopoietic stem cells, undergo a series of cell stage transitions tightly regulated by dynamic changes in the transcriptome. Rapid transcriptome changes also allow for precise immune responses in different contexts. Extensive studies have attributed the transcriptome changes to the activity of transcription factors. However, my doctoral work revealed the role of N^6-methyladenosine (m^6A) modifications in assisting these rapid transcriptome changes in immune cells. In developing B cells, we discovered that m^6A modifications on mRNAs accelerate the decay through recognition by m^6A binding protein, YTHDF2, during the transition from pro-B cell to large pre-B cell and pre-B cell proliferation. Additionally, in intratumoral regulatory T (Treg) cells, m^6A modifications on transcripts of NF-kB negative regulators indirectly perturb NF-kB mediated transcription to impact immune response in the tumor microenvironment. The discovery of these regulatory mechanisms highlights the m^6A pathway as a promising target for manipulating immune cell function and enhancing anti-tumor immune response. To further explore the therapeutic potentials, we initiated a study to identify small molecule inhibitors of YTHDF2. Successful inhibitors targeting the m^6A pathway would have tremendous clinical value.

List of Publications Based on Work Presented in this Thesis[†]

1. **Linda Zhang**, Jiangbo Wei, Zhongyu Zou, and Chuan He. Targeting RNA modification systems in therapies, *Nat Rev Drug Discov.*, in review.
2. **Linda Zhang**, Xiaoyang Dou, Zhong Zheng, Chang Ye, Thomas X Lu, Hua L Liang, Liangliang Want, Ralph R Weichselbaum, and Chuan He. YTHDF2/m^{6}A/NF-κB axis controls anti-tumor immunity by regulating intratumoral Tregs, *EMBO J.*, e113126 (2023)
3. Liangliang Wang, Xiaoyang Dou, Shijie Chen, Xianbin Yu, Xiaona Huang, **Linda Zhang**, Yantao Chen, Jiaai Wang, Kaiting Yang, Jason Bugno, Sean Pitroda, Xingchen Ding, Andras Piffko, Wei Si, Chao Chen, Hualiang Jiang, Bing Zhou, Steven J Chmura, Cheng Luo, Hua L Liang, Chuan He, and Ralph R Weichselbaum. YTHDF2 inhibition potentiates radiotherapy antitumor efficacy, *Cancer Cell*, (2020) https://doi.org/10.1016/j.ccell.2023.04.019
4. Hideki Terajima, Mijia Lu, **Linda Zhang**, Qi Cui, Yanhong Shi, Jianrong Li, and Chuan He. *N*^{6}-methyladenosine promotes induction of ADAR1-mediated A-to-I RNA editing to suppress aberrant antiviral innate immune responses, *PLoS Biol.*, 19(7), e3001292 (2021)
5. Ane Olazagoitia-Garmendia, **Linda Zhang**, Paula Mera, Julie K Godbout, Maialen Sebastian-DelaCruz, Iraia Garcia-Santisteban, Luis Manuel Mendoza, Alain Huerta, Iñaki Irastorza, Govind Bhagat, Peter H Green, Laura Herrero, Dolors Serra, Jose Antonio Rodriguez, Elena F Verdu, Chuan He, Jose Ramon Bilbao, and Ainara Castellanos-Rubio. Gluten-induced RNA methylation changes regulate intestinal inflammation via allele-specific *XPO1* translation in epithelial cells, *Gut*, 71(1), 68-76 (2021)

[†] The following chapters of the dissertation contain sections and figures adopted from the listed publications with modifications. Chapter 1 and 5: publication 1; chapter 2: publication 8; chapter 3: publication 2.

6. Jie Du, Wang Liao, Weicheng Liu, Dilip K. Deb, Lei He, Phillip J. Hsu, Tivoli Nguyen, **Linda Zhang**, Marc Bissonnette, Chuan He, and Yan Chun Li. N^6-Adenosine Methylation of *Socs1* mRNA Is Required to Sustain the Negative Feedback Control of Macrophage Activation, *Dev Cell*, 55(6), 737-753.e7 (2020)
7. Thomas X Lu, Zhong Zheng, **Linda Zhang**, Hui-Lung Sun, Marc Bissonnette, Haochu Huang, and Chuan He. A New Model of Spontaneous Colitis in Mice Induced by Deletion of an RNA m^6A Methyltransferase Component METTL14 in T Cells, *Cell Mol Gastroenterol Hepatol.*, 10(4), 747-761 (2020)
8. Zhong Zheng, **Linda Zhang**, Xiao-Long Cui, Xianbin Yu, Phillip J Hsu, Ruitu Lyu, Haiyan Tan, Malay Mandal, Michelle Zhang, Hui-Lung Sun, Arantxa Sanchez Castillo, Junmin Peng, Marcus R Clark, Chuan He, and Haochu Huang. Control of Early B Cell Development by the RNA N^6-Methyladenosine Methylation, *Cell Rep.*, 31(13), 107819 (2020)

Chapter 1

Introduction: *N*^{6}-methyladenosine (m^{6}A): Orchestrator of immune response and therapeutic opportunities

1.1 RNA metabolism regulated by RNA m^{6}A modifications

Since the discovery of pseudouridine as the first RNA modification in 1957[1], over 170 modifications have been identified across all RNA species[2]. Similar to epigenetic modifications on histone and DNA, these RNA modifications can perturb gene expression without changing the DNA or RNA sequence. However, unlike epigenetic marks, which have already guided the discovery of successful anti-cancer drugs[3], the biological implication of many RNA modifications was left unknown for a long time. The studies of RNA modification effector proteins, specifically those involved in *N*^{6}-methyladenosine (m^{6}A), in the 2010s led to rapid growth in the field[4–6]. Proteins that were able to install and remove modifications imply the dynamic functions of RNA modifications during organism development and in response to stimuli. Further, advances in detection technology also allow for the accurate quantification and transcriptome-wide mapping of RNA modifications[7]. While most modifications are sparse in the transcriptome, they could exhibit specific functions, with numerous biological events affected by diverse RNA modifications[8–12]. Studies revealed that post- and co-transcriptional modifications on RNA alter RNA structure, processing, translation, and degradation[13–18]. Beyond RNA metabolism and translation, RNA modifications also tune the formation of RNA:DNA duplexes[19], as well as global chromatin state and transcription[20].

m^{6}A is the most abundant internal modification in mammalian mRNA (Figure 1.1). On average, each mammalian transcript has three m^{6}A modifications within a consensus sequence of

RRm^{6}ACH (R=A/G, H=A/C/U)[21]. m^{6}A methylation can cover every region of mRNAs with enrichment towards 3' UTR and a peak near the stop codon[4]. METTL3 and METTL14 are key components of the main RNA m^{6}A methyltransferase "writer" complex that deposits m^{6}A[22,23]. METTL3 and METTL14 form the core stable heterodimer. The discovery of m^{6}A erasers fat mass and obesity-associated protein (FTO) and alkB homolog 5 (ALKBH5) in 2011 and 2013[5,24], respectively, revealed that RNA m^{6}A can be actively demethylated.

m^{6}A modifications regulate gene expression through m^{6}A binding proteins. The most well-studied readers are the YT521-B homology (YTH) domain-containing family proteins, YTHDF1, YTHDF2, YTHDF3, YTHDC1, and YTHDC2[25]. These readers regulate the processing of m^{6}A methylated transcripts to dictate biological functions. The conserved C-terminal YTH domain has a hydrophobic pocket with tryptophan residues for m^{6}A binding. The diverse N-terminal allows for the unique interaction with other proteins and localization, leading to different functions of these proteins[25]. YTHDF1 promotes the translation of its m^{6}A target transcripts through interactions with translation machineries[26]. YTHDF2 binds m^{6}A labeled mRNAs, recruits CCR4-NOT deadenylase complex, and localizes to processing bodies to facilitate degradation[27]. Partnering with YTHFD1 and YTHDF2, YTHDF3 can regulate both the translation and decay of m^{6}A mRNAs[17]. YTHDC1 and YTHDC2 are nuclear m^{6}A binding proteins. YTHDC1 is known to regulate pre-mRNA splicing and export through interactions with splicing and export factor SRSF3[14]. It also regulates chromosome-associated regulatory RNAs to tune chromatin accessibility and transcription in embryonic stem cells[28]. YTHDC2 facilitates the translation and decay of m^{6}A transcripts[29].

m^{6}A is also bound by insulin-like growth factors 2 mRNA-binding proteins (IGF2BPs), IGF2BP1, IGF2BP2, and IGF2BP3. IGF2BPs have the hnRNP-K homology (KH) domain that recognizes m^{6}A to stabilize m^{6}A-modified transcripts and promote translation[30]. Changes in RNA structure induced by m^{6}A modifications are recognized and bound by heterogeneous nuclear ribonucleoprotein C (HNRNPC), HNRNPG, and HNRNPA2B1 to regulate alternative splicing and pri-miRNA processing[13,31,32].

The physiological roles of m^{6}A and its readers have been identified in various biological processes, such as embryonic stem cell differentiation[8], hematopoietic stem cell development[33–36], and immune responses[37–39]. These studies collectively supported the proposed role of m^{6}A as an mRNA chemical mark that allows cells to group hundreds to thousands of transcripts for coordinated modulation in translation or degradation in response to cellular and environmental signals[40,41].

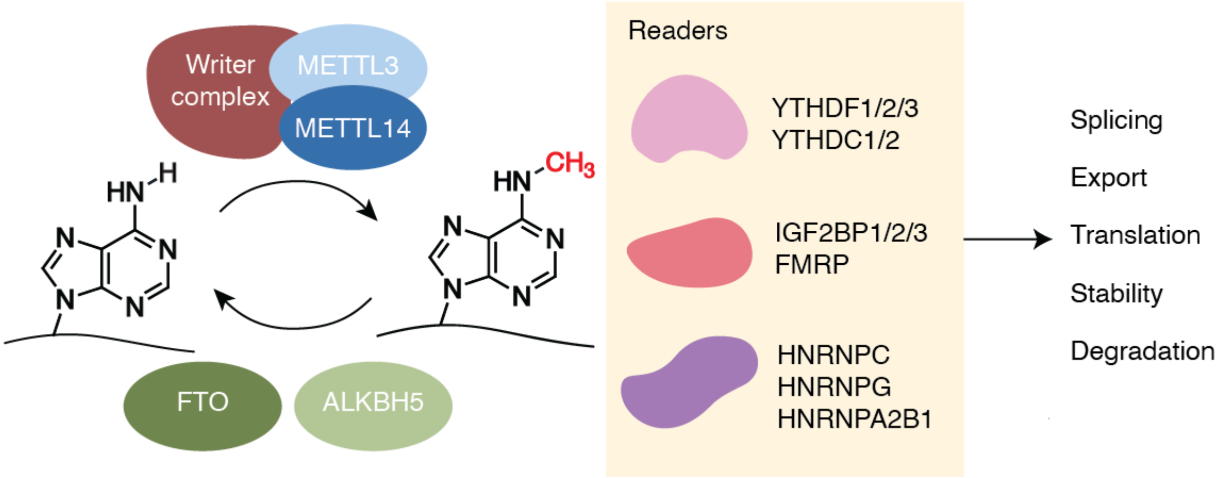

Figure 1.1 Key regulator proteins of m^{6}A modification

m^{6}A methylation of RNA is catalyzed by the m^{6}A writer complex, including METTL3 and METTL14, and reversibly removed by eraser proteins FTO and ALKBH5. m^{6}A reader proteins that preferentially bind m^{6}A modifications in the nucleus and cytoplasm regulate many aspects of RNA metabolism.

1.2 m^{6}A regulation of immune response

The immune system defends against infections. The mechanism to recognize self-and non-self and the defensive mechanisms used to eliminate infections are highly regulated. Both hyper and hypoactivation of the immune response can result in diseases[42,43]. Increasing evidence showed that m^6A modifications provide an additional layer of regulation in immune cell functions and response (Figure 1.2).

Firstly, m^6A is crucial for immune cell fate. Immune cells are differentiated from hematopoietic stem cells (HSCs), and HSC differentiation is regulated by m^6A modifications installed by METTL3[36]. In T cells, m^6A modifications on SOCS mRNA facilitate the degradation of SOCS mRNA, which allows for the successful IL-7/STAT5 signaling to promote T cell proliferation and differentiation[38]. Treg differentiation from naïve T cells is also dependent on m^6A[44]. METTL3 expression level changes during macrophage polarization to methylate *STAT1* transcripts, which increases transcript stability and protein expression[45]. A separate study showed that FTO also regulated the polarization of macrophages. FTO demethylates the m^6A modifications on *STAT1* and *PPAR-γ* transcripts to prevent the decay mediated by YTHDF2. FTO knockdown in macrophages also inhibits NF-kB signaling[46].

Secondly, m^6A regulates immune cell function and activation. In regulatory T (Treg) cells, SOCS family genes are methylated to regulate IL-2/STAT5 signaling, which affects Treg suppressive function[47]. A recent report showed that ALKBH5 is upregulated upon T cell activation and can modulate the pathogenicity of $CD4^+$ T cells during autoimmunity[48]. Dendritic cell maturation and activation are also supported by METTL3 methylation. The transcripts encoding CD40, CD80, and TIRAP are methylated and have enhanced translation efficiency facilitated by YTHDF1 binding. As a result, METTL3 regulates innate immune response and NF-kB signaling[49].

Thirdly, m^6A regulates the immune response to viral infections. In macrophages, DEAD-box (DDX) helicases can recruit ALKBH5 to demethylate m^6A-marked antiviral transcripts to inhibit the production of type I interferons after viral infection[50]. In response to virus infection, *Ythdf2*-deficient natural killer (NK) cells have decreased perforin expression and reduced proliferation[51]. By promoting the translation of transcription corepressor forkhead box protein O3 (FOXO3), YTHDF3 acts as a negative regulator of immune response and promotes viral replication in infected cells. The YTHDF3-mediated expression of FOXO3 suppresses IFN-stimulated genes essential for activating immune responses against viral infections[52].

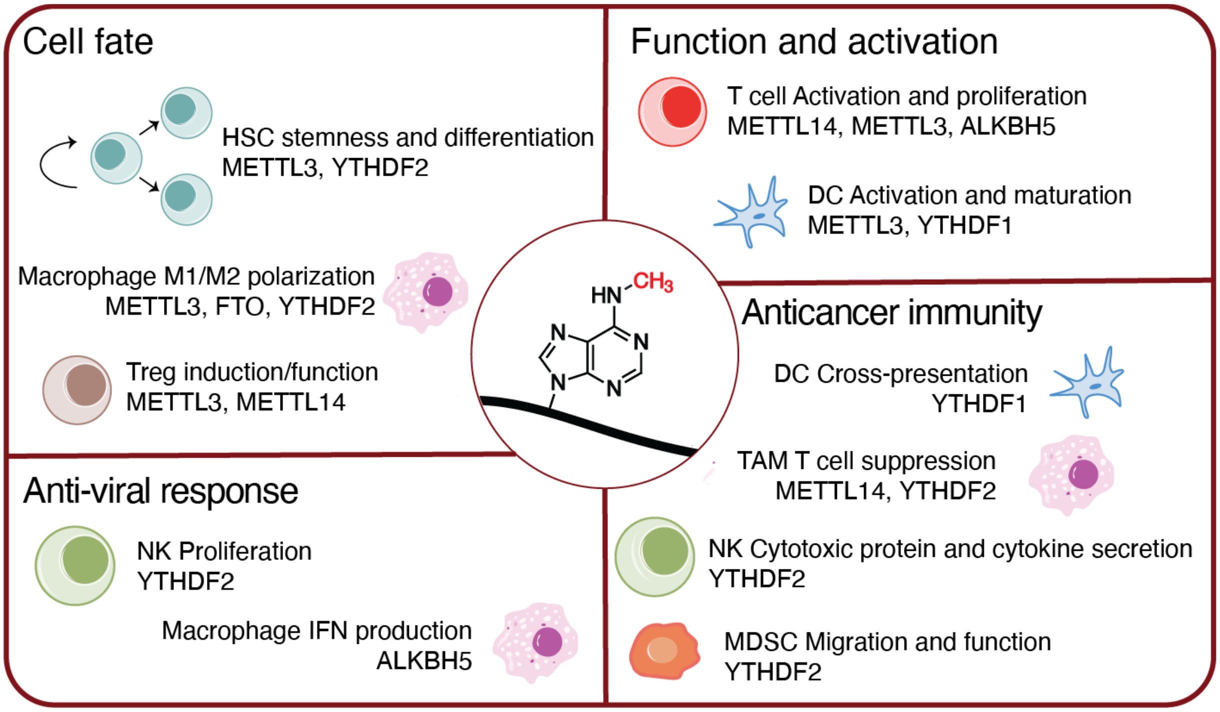

Figure 1.2 m^{6}A regulation of the immune cells

m^{6}A modifications have been studied in various immune cells, including T cells, regulatory T (Treg) cells, macrophages, dendritic cells (DC), natural killer (NK) cells, and myeloid-derived suppressor cells (MDSCs) to regulate their differentiation and functions in different contexts.

1.3 Emerging role of m^{6}A in anti-tumor immune response

Despite the highly regulated immune system, tumor cells can escape immune surveillance. While tumor cells derived from healthy cells have a unique expression of antigens, the antigen expression level and immunogenicity are often insufficient to initiate an immune response[53]. Further, cancer cells can express inhibitory proteins and secret immunosuppressive cytokines, generating an immunosuppressive microenvironment[54]. Studies showed that m^{6}A modifications regulate immune escape. For example, FTO can be utilized by tumors for immune escape through m^{6}A demethylation of transcripts encoding the transcription factors c-*Jun*, *JunB*, and *CEBPA* associated with glycolytic metabolism[55]. In intrahepatic cholangiocarcinoma (ICC), tumor-intrinsic ALKBH5 inhibited the expansion and cytotoxicity of T cells by sustaining tumor cell PD-L1 expression through 3'UTR m^{6}A demethylation of PD-L1 mRNA[56]. Moreover, in anti-PD-1 therapy, ALKBH5 could control lactate accumulation through target gene m^{6}A demethylation and therefore modulate suppressive immune cell accumulation in the tumor microenvironment (TME)[57]. Hypoxia-induced ALKBH5 also stabilizes lncRNA *NEAT1* through m^{6}A demethylation and facilitates the paraspeckle assembly, thereby causing the upregulation of *CXCL8/IL8* by relocating the transcriptional repressor SFPQ from their promoters. The indirect regulation of CXCL8/IL8 expression in tumor cells regulates the recruitment of tumor-associated macrophages[58]. There is a correlation between YTHDF1 and immune cell infiltration and immune checkpoint gene expression, and the direction of correlation depends on the cancer type[59].

Our understanding of m^{6}A modifications in the anti-tumor immune response is still limited (Figure 1.2). In mice, deletion of *Ythdf1* can hinder tumor development through increased dendritic cell neoantigen presentation to T cells leading to more antigen-specific T cell response[37]. YTHDF1 regulates the translation of lysosomal cathepsin proteases, which are known to degrade antigens. YTHDF1 KO mice showed slower tumor growth and a better response to anti-PD-L1 treatment. Deletion of *Ythdf2* in NK cells resulted in diminished anti-tumor immunity due to lower expression of IFN-g, granzyme B, and perforin in NK cells. However, Wang et al. showed that irradiation promotes the expression of YTHDF2 in myeloid-derived suppressor cells (MDSCs) through the activation of NF-κB signaling. NF-κB regulates the transcription activation of YTHDF2. YTHDF2 then further enhances NF-κB signaling to support MDSC function and migration. Conditional knockout of *Ythdf2* in MDSCs enhances anti-tumor immunity by reducing MDSC infiltration and function[60]. These results collectively depict YTHDF2 as a key factor in modulating immune cell function and activation in the tumor microenvironment, with NF-κB as a main pathway involved in the regulation. A subset of tumor-associated macrophages has elevated m^6A abundance and expression of METTL3, METTL14, FTO, and YTHDF2. Collectively, transcripts encoding immunoregulatory ligands, specifically EBI3, are methylated by METTL14 and decayed by YTHDF2. Overexpression of EBI3 due to deletion of *Mettl14* or *Ythdf2* results in exhausted CD8 T cells and decreased CD8 T cell infiltration[61].

Tumor drug resistance is also regulated by m^6A. Deletion of *Mettl3* or *Mettl14* sensitizes tumors to anti-PD-1 immunotherapy in mice[62]. In colorectal cancer, YTHDF1 expression level is positively associated with cisplatin resistance[63]. YTHDF1 upregulation in cisplatin resistance cells promotes the translation of *GLS1*, which metabolizes glutamine for cancer cell proliferation. Inhibition or GLS1 or YTHDF1 re-sensitizes cells to cisplatin treatment, providing targets to overcome drug resistance. Knockdown of YTHDF1 also sensitizes CRC to anti-cancer drugs fluorouracil and oxaliplatin[64]. FTO overexpression in leukemia cells also drives tyrosine kinase inhibitor (TKI) resistance by stabilizing transcripts coding for proliferation and survival[65]. Inhibition of ALKBH5 also sensitized cancer immunotherapy in mouse model[57].

1.4 Modulating m^6A modification and function by small molecule inhibitors

Several inhibitors targeting m^6A effector proteins have been discovered (Figure 1.3). The Caflisch lab screened an adenine-based library and reported two potent METTL3 inhibitors: UZH1a[66] and UZH2[67]. UZH1a can inhibit 50% of METTL3 activity at 280 nM[66]. Treatment with UZH2 was able to reduce cellular mRNA m^6A modifications by ~80% with EC_{50} 0.7 μM for AML cell lines[67]. Yanagi et al. discovered that methylation by METTL3 during the lytic cycle of tumor virus Epstein-Barr virus enhances the generation of progeny virions. Application of UZH1a following lytic induction decreased viral replication and inhibited the growth of EBV-positive cells[68]. Yankova et al. reported a new class of compound that is not structurally related to adenosine[69]. Compound STM2457 has a K_d of 1.4 nM with the METTL3/14 complex. In cells, this inhibitor can decrease the amount of m^6A on mRNAs with an IC_{50} of 2.2 μM. Applying STM2457 to AML cell lines led to reduced methylation level and diminished translation efficiency of *SP1*, *MYC*, and *HOXA10*, resulting in reduced proliferation with IC_{50} values ~1-10 μM. In AML patient-derived xenografts (PDX) model, 12-14 treatments with STM2457 at 50 mg/kg could effectively prevent AML and prolong survival when compared to the control vehicle. Recently, STORM Therapeutics reported STC-15, an optimization of STM2457, could inhibit tumor cell growth while activating anti-tumor immune response[70]. STC-15 has entered the clinical study for patients with solid tumors (NCT05584111). This marks the first success of targeting RNA modifications for clinical trials.

Multiple small-molecule inhibitors of FTO have been developed for potential therapeutic implications. In 2012, a natural product, rhein, was identified as the first FTO inhibitor through a structure-based *in silico* high-throughput screening, which can competitively bind to the FTO active site *in vitro* with a Kd of 2.4 μM[71]. Rhein showed moderate inhibitory activity on m^6A demethylation inside cells, with a relatively high IC50 of 21 μM in leukemia cells. Application of rhein to TKI-resistant cells resensitized them to TKI treatment[65]. Mimicking the structure of ascorbic acid, a cofactor that induces the reactivity of a large family of Fe(II)- and 2OG-dependent dioxygenases, MO-I-500 was identified as an inhibitor with an IC50 of 8.7 μM for purified FTO *in vitro* and applied in triple-negative breast cancer cells to arrest proliferation[72,73]. Note that both

Rhein and MO-I-500 lack selectivity towards FTO as they broadly target other 2-OG oxygenases. However, a 2OG analog, compound 12, exhibits unexpected ~30-fold selectivity with IC_{50} around 1 μM against FTO over other AlkB subfamilies and 2OG oxygenases, which could lead to a dose-dependent increase of mRNA m^6A after applying to HeLa cells[74]. A natural oncometabolite, R-2HG, with a similar structural skeleton to 2OG, was also reported to show a broad anti-tumor effect by competitively inhibiting the enzymatic activity of FTO[75].

In 2015, an FDA-approved, non-steroidal, anti-inflammatory drug, meclofenamic acid (MA), was reported to selectively compete with FTO binding over the other demethylase, ALKBH5, to the m^6A-bearing nucleic acid, with an IC_{50} of 7 μM[76]. Its ethyl ester derivative effectively inhibits glioblastoma stem cell (GSC) growth *in vitro* as well as *in vivo* xenograft model, and also synergistically enhances the temozolomide treatment in glioma. In 2019, the FDA-approved drug entacapone, a known catechol-*O*-methyltransferase inhibitor used to treat Parkinson’s disease, was screened and biochemically validated as a highly selective FTO inhibitor with an IC50 of 3.5 μM[77]. Entacapone administration reduced body weight and lowered fasting blood glucose concentrations in diet-induced obese mice by regulating gluconeogenesis in the liver and thermogenesis in adipose tissues through FTO inhibition.

Later, MA-derived inhibitors with much higher potency, FB23 and FB23-2, were developed through structure-guided design and optimization, which directly and selectively bind to FTO, inhibiting its demethylase activity[78]. FB23-2 showed moderate cell permeability with an IC_{50} of 2.6 μM and high efficiency in suppressing the proliferation of multiple AML cell lines as well as the primary cells in xeno-transplanted mice. FB23-2 treatment in mESCs could reduce ESC self-renewal while promoting EB differentiation, recapitulating the effect of *Fto* deletion[79]. A further optimized FB23 analog, Dac51, was applied to promote T cell anti-tumor response and synergizes with anti-PD-L1 blockade by attenuating glycolysis through FTO inhibition[55]. Through a structure-based virtual screening, two highly potent FTO inhibitors, CS1 and CS2, with IC_{50} of ~100 nM in several cell lines tested[80]. Both inhibitors appear to suppress immune checkpoint gene expression and immune evasion. More recently, two novel FTO inhibitors, FTO-02 (IC_{50} = 2.2 µM) and FTO-04 (IC_{50} = 3.4 µM), were developed through a similar approach, which could prevent neurosphere formation in patient-derived GSCs without inhibiting the growth of healthy control[81].

Efforts have also been devoted to the development of small molecules selectively against ALKBH5. A 3D proteome-wide *in silico* screening identified ALKBH5 as one of the top off-targets of MV1035, a known sodium channel blocker, by competing with the 2OG binding to ALKBH5[82]. MV1035 inhibits glioma cell migration and invasion dependent on the ALKBH5-mediated m^6A demethylation rather than sodium channel blockade. Through structure-activity relationship-based *in silico* screening focusing on the X-ray crystal structure of ALKBH5, ALK-04 was identified as the first ALKBH5-specific inhibitor, which sensitized cancer immunotherapy in mouse models, indicating a potential combination treatment to overcome resistance to immune checkpoint blockade[57]. Another high-throughput virtual screening of 144,000 compounds combined with enzyme and cancer cell proliferation inhibition assays identified two potent ALKBH5 inhibitors, 2-[(1-hydroxy-2-oxo-2-phenylethyl)sulfanyl]acetic acid (Compound 3, IC_{50} = 0.84 µM) and 4-{[(furan-2-yl)methyl]amino}-1,2-diazinane-3,6-dione (Compound 6, IC_{50} = 1.79 µM)[83]. Note that the IC_{50} of the ALKBH5 inhibitor on cancer cell proliferation varies from a low micromolar range to negligible, likely due to the context-dependent function of m^6A in different types of cancer cells. Recently, a new class of ALKBH5 inhibitors with the 1-aryl-1*H*-pyrazole scaffold was reported through a high-throughput fluorescence polarization assay.

Thereinto, compound 20m showed an IC50 of 0.021 μM and high selectivity (> 1000 folds) towards ALKBH5 over FTO[84].

Fluorescence polarization-based screening assays with the YTHDF proteins and m^6A-containing probes were used to screen for potential inhibitors. Salvianolic acid C (SAC) is the first YTHDF1 targeting inhibitor[85]. SAC binds YTHDF1 with a K_D of 5-6 μM. In the AlphaScreen assay, SAC could inhibit YTHDF1 and m^6A binding with an IC_{50} value of 1.4 μM. Treatment of FXS organoid with SAC inhibited YTHDF1 mediated hyper-translation, which rescued neural progenitor cell proliferation and differentiation[85]. Another screen revealed compound DC-Y13-27 as an inhibitor of YTHDF2. It competes for the m^6A binding pocket with an IC_{50} of 21 μM. Similar to *Ythdf2* deletion in MDSCs, inhibition by DC-Y13-27 also inhibited NF-kB signaling in MDSCs. In mice models, combining DC-Y13-27 with IR or anti-PD-L1 treatments significantly improved the anti-tumor effects by reducing MDSC infiltration[60].

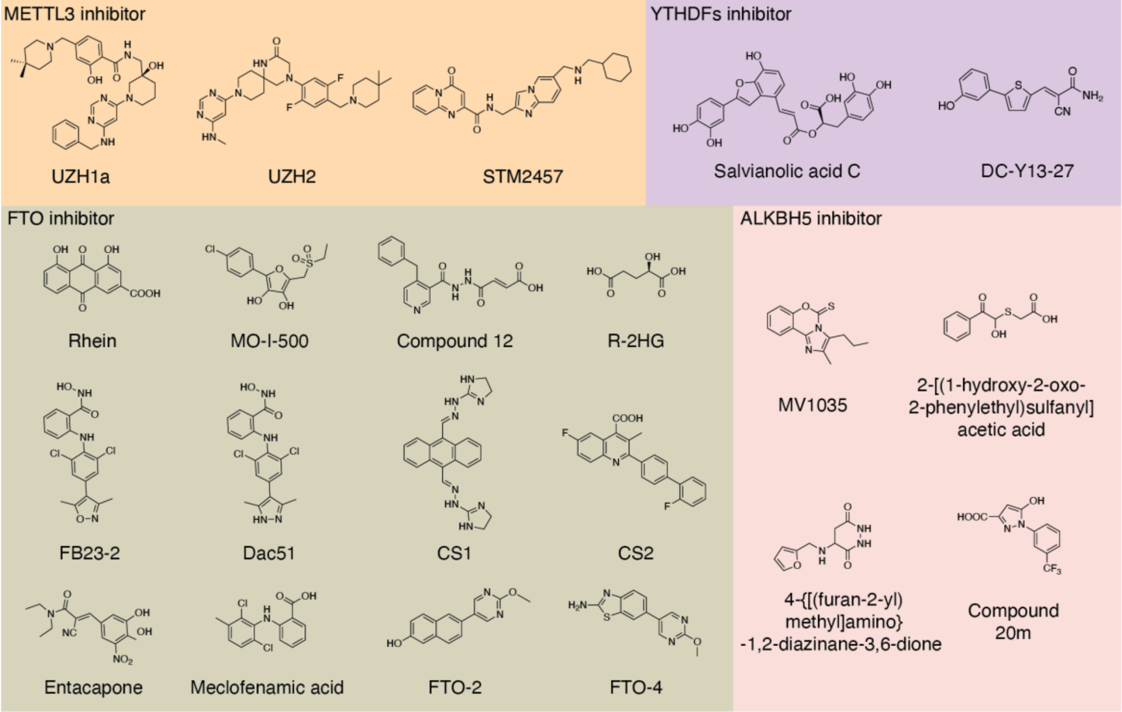

Figure 1.3 Small molecule inhibitors of m^6A effector proteins

(**Figure 1.3, continued**) Inhibitors targeting RNA modification writer, eraser, and reader proteins have been developed.

1.5 Scope of this thesis

My thesis will focus on revealing the role of m^6A in facilitating immune cell state transition and context-dependent functions, especially in the tumor microenvironment, and targeting the effector protein YTHDF2 with small molecule inhibitors for translational potentials.

Chapter 2 shows YTHDF2 as a transcriptome switch by mediating the decay of m^6A-modified transcripts to assist B cell development and proliferation.

Chapter 3 presents the role of YTHDF2 in regulating transcription activities of NF-κB signaling in intratumoral Treg cells through m^6A modifications.

Chapter 4 describes the efforts in developing small molecule inhibitors targeting YTHDF2.

Chapter 5 summarizes the recent findings in anti-tumor immune response regulated by m^6A modifications, discusses the potential of targeting the m^6A pathways for overcoming challenges in cancer immunotherapy, and specifies essential considerations in developing inhibitors.

Chapter 2

Control of Early B Cell Development by the RNA N^6-Methyladenosine Methylation

2.1 Introduction: Transcriptome regulations of B cell development

B cell development represents a cellular model system that incorporates a series of cell fate determination and cell differentiation processes. It is hallmarked by sequential DNA rearrangements of the immunoglobulin heavy (IgH) and light (IgL) chain loci as well as rapid transitions between proliferation and recombination, resulting in a diverse repertoire of peripheral B cells that recognize foreign antigens but are tolerant of self[86,87]. The accurate control of cell state transitions in B lymphopoiesis highly depends on the precise regulation of gene expression in multiple layers. At the gene transcription level, a series of transcription factors (TFs) that directly bind to specific DNA sequences have been well known to sequentially control gene expression, providing the first layer of regulation for cell fate determination and transitions[88,89]. Epigenetic regulatory pathways involving DNA or histone modifications regulate chromatin accessibility, offering an additional layer of regulation at the transcription level[90–92]. Accumulating evidence indicates that post-transcriptional regulation of RNA represents another vital regulatory layer of gene expression, as RNA binding proteins (RBPs)[93–95] and microRNAs[96–98] have been shown to fine-tune gene expression by modulating mRNA degradation, splicing, or translation during B lymphopoiesis. Recently, modifications of RNA have emerged as an additional regulation layer of gene expression, but their roles in B cell development remained unexplored.

2.2 Results

2.2.1 *Mettl14* deficiency severely blocks early B cell development in mice

To investigate the potential role of RNA m^6A in B cells, we generated *Mb1*$^{cre/+}$*Mettl14*$^{fl/fl}$ (*Mettl14* knockout, KO) mice. Compared with the *Mb1*$^{+/+}$*Mettl14*$^{fl/fl}$ or *Mb1*$^{cre/+}$*Mettl14*$^{fl/+}$ (wild-type, WT) littermates, *Mettl14* KO mice had an over 120-fold reduction in the splenic B cell numbers (Figure 2.1A) and undetectable B cells in the peritoneal cavity (Figure 2.1B). Analysis of B cell progenitors in the bone marrow showed that *Mettl14* KO mice had a nearly 75% reduction in the percentage of B lineage (CD19$^+$) cells (Figure 2.1C). Within the CD19$^+$ population, the percentages (Figure 2.1C) and numbers (Figure 2.1D) of the immature B cells and the mature B cells were both severely decreased. These data indicate that loss of METTL14 dramatically impairs B cell development.

We further divided the CD19$^+$B220^{mid}Igκ/λ^- population into pro-B cells, early large pre-B cells, late large pre-B cells, and small pre-B cells (Figure 2.1C). *Mettl14* KO mice displayed higher portions of CD43^{hi} pro-B cells and large pre-B cells but a much lower portion of CD43^{lo} cells. Whereas WT large pre-B cells contain both early and late populations, *Mettl14* KO large pre-B cells lack the late population (Figure 2.1C). Quantification of all the subpopulations showed that *Mettl14* KO mice had normal numbers of the pro-B cells and the early (CD2$^-$) large pre-B cells, significantly reduced numbers of the late (CD2$^+$) large pre-B cells and the small pre-B cells (CD2$^+$; Figure 2.1D), and an accumulation of an abnormal CD2$^-$small pre-B population (Figure 2.1E).

Despite the normal cell numbers, the pro-B cells and the early large pre-B cells from the *Mettl14* KO mice displayed significantly lower proliferation rates than the respective counterparts from the WT mice (Figure 2.1F). In contrast, although WT small pre-B cells already exited cell cycle, *Mettl14* KO CD43^{lo} small cells remained more proliferative (Figure 2.1F), further supporting that these cells did not reach the small pre-B stage. Quantitative PCR showed

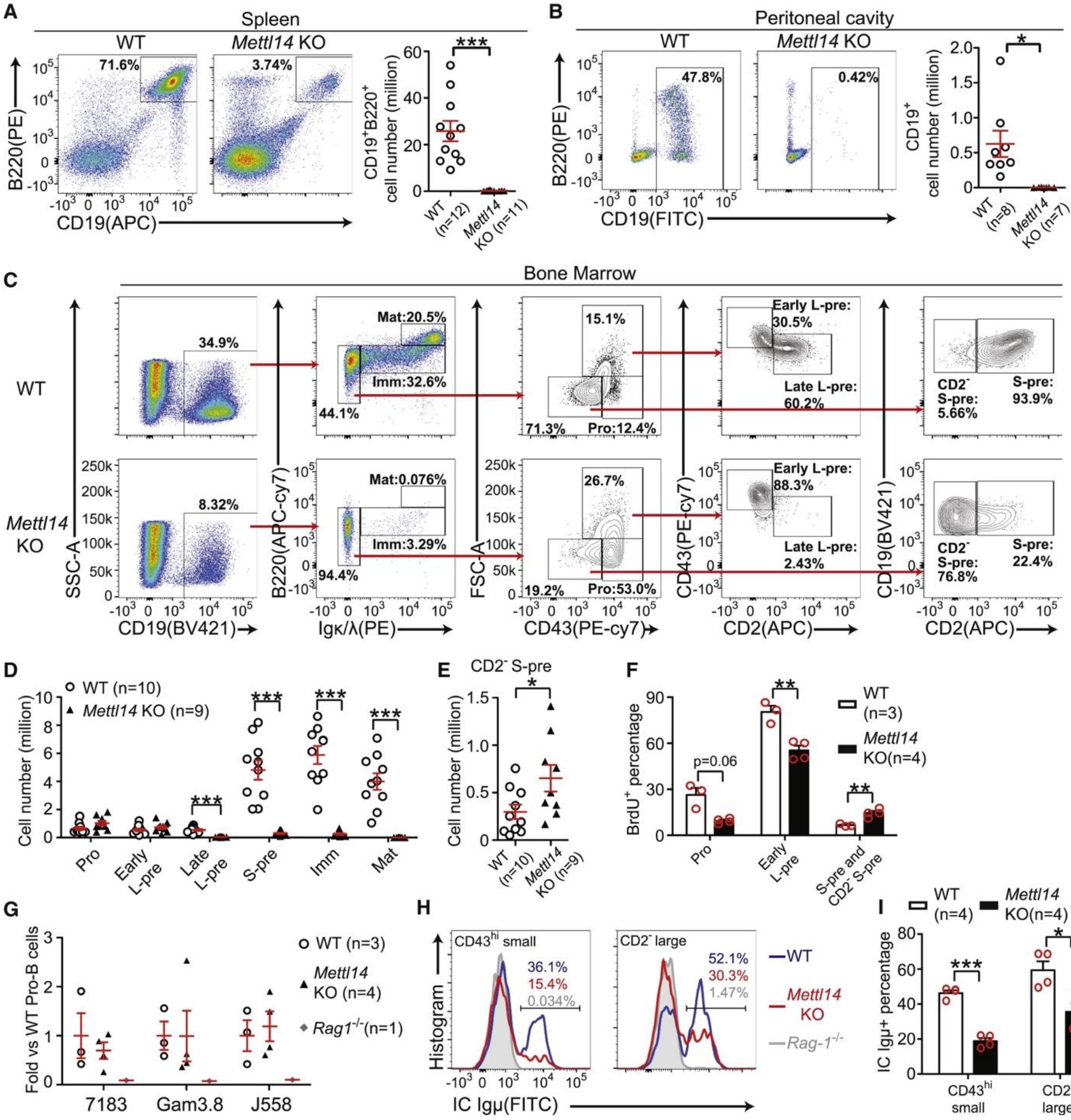

Figure 2.1 Loss of METTL14 blocks early B cell development *in vivo*.

(**A**) and (**B**), Flow cytometry plots and quantifications of B cells in the spleens (**A**) and the peritoneal cavity (**B**) of indicated mice. (**C**) and (**D**), Flow cytometry plots (**C**) and quantifications (**D**) of indicated populations in the bone marrow of indicated mice. (**E**) Quantification of the abnormal CD2^{-}small pre-B population of indicated mice. (**F**) BrdU (1 mg/mouse) was intraperitoneally injected into mice, and BrdU incorporation in indicated B-lineage cells from indicated mice was analyzed 1 h later. (**G**) Quantitative PCR of indicated recombined IgH families in the pro-B cells sorted from indicated mice. (**H**) and (**I**), Flow cytometry plots (**H**) and percentages (**I**) of intracellular Igμ^{+} cells in indicated CD19^{+}B220^{mid}Igκ/λ^{-} bone marrow subpopulations from indicated mice.

that *Mettl14* KO pro-B cells did not have any significant defect in IgH recombination at the DNA level (Figure 2.1G); however, intracellular staining of Igμ showed that developing B cells from the *Mettl14* KO mice had significantly less Igμ$^+$ populations than those from WT mice (Figure 2.1H-I) suggesting that *Mettl14* deficiency might impair expression of recombined IgH. Altogether, these *in vivo* data demonstrated that loss of METTL14 caused severe defects during early B cell development.

2.2.2 *Mettl14* deficiency impairs IL-7-induced pro-B cell proliferation and blocks two transitions in B cell development

Next, we investigated how METTL14 modulates the major stages of B cell differentiation. WT CD19$^+$Igκ/λ$^-$CD2$^-$ cells (representing both pro-B and early large pre-B stages) started to proliferate at day 2 in the presence of interleukin-7 (IL-7), leading to an increase of cell number together with an enlargement of cell size. In contrast, *Mettl14* KO group showed a 5- to 10-fold less cell number than WT controls during the expansion, delayed initiation of proliferation, and delayed cell size enlargement (Figure 2.2A-C).

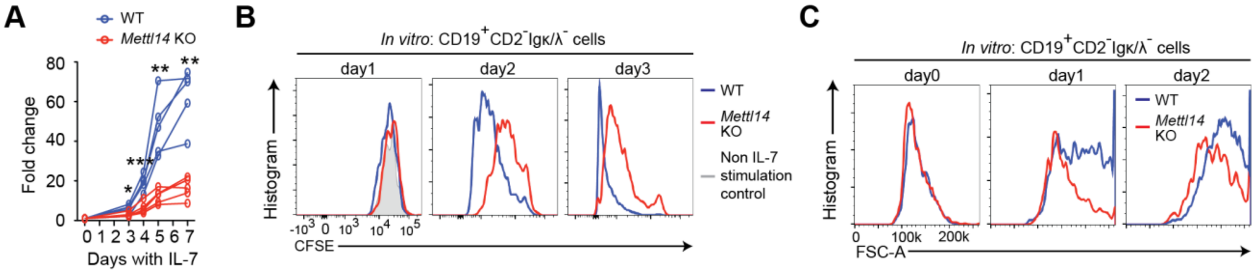

Figure 2.2 Loss of METTL14 impairs IL-7-induced pro-B cell proliferation

(**A**) Fold changes of the CD19$^+$CD2$^-$Igκ/λ$^-$ cells versus day 0 at indicated times during IL-7-induced expansion are shown. (**B**) CFSE intensity of the CD19$^+$CD2$^-$Igκ/λ$^-$ cells of indicated group at indicated times during IL-7-induced expansion are shown. The same WT cells cultured without IL-7 at day 1 were used as baseline control (**C**) Forward scatterplots of indicated CD19$^+$CD2$^-$Igκ/λ$^-$ cells at indicated times during IL-7-induced expansion.

High-throughput RNA sequencing (RNA-seq) showed that, before IL-7 stimulation, *ex vivo* sorted pro-B cells from *Mettl14* KO mice displayed relatively small differences in the transcriptome compared with the WT controls (Figure 2.3A). 6-h post-IL-7 stimulation, more difference in gene expression was detected between the WT and *Mettl14* KO pro-B cells (Figure 2.3B). Differential expressed genes (DEGs) with lower expression in the *Mettl14* KO cells after IL-7 stimulation strongly enrich cell-cycle-related genes (Figure 2.3C), which is consistent with decreased proliferation observed in these cells.

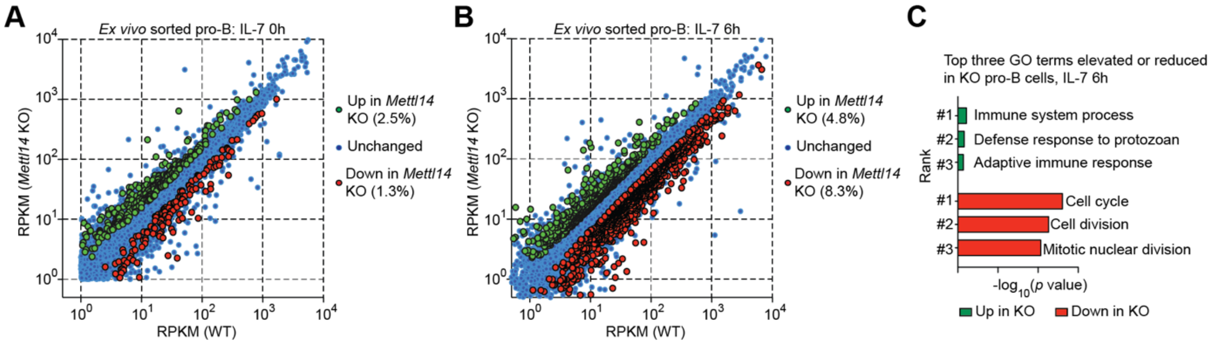

Figure 2.3 Loss of METTL14 causes changes in gene expression in IL-7-stimulated B cells

(**A**) and (**B**), Scatter plot of gene expression differences between *Mettl14* KO and WT pro-B ($CD19^{+}B220^{mid}Ig\kappa/\lambda^{-}CD43^{hi}CD2^{-}$small) cells upon 0 hours (**A**) or 6 hours (**B**) IL-7 stimulation. Each dot represents one gene. The percentage of genes in each group is shown in the parentheses after the group names. (**C**) DEGs between WT and *Mettl14* pro-B cells upon 6 hours IL-7 stimulation were subject to GO term enrichment analysis. The top 3 terms that are elevated (green) or reduced (red) in the *Mettl14* KO group are shown.

As revealed by RNA-seq, *Mettl14* KO large B cells that were expanded in the presence of IL-7 for 5 days displayed dramatic alterations in gene expression (Figure 2.4A). Down regulated genes in the *Mettl14* KO cells were also strongly enriched with cell-cycle-related genes (Figure 2.4B). Transcriptome analysis confirmed that the IL-7/STAT5 signaling cascade was intact in the *Mettl14* KO large pre-B cells, as the expression induction of the key STAT5-regulated genes *Mcl1*, *Bcl2*[99], and *Ebf1*[100] were normal, but the key STAT5-stimulated cyclin essential for the initiation of proliferation in pro-B cells, cyclin D3[101,102], was significantly lower in the *Mettl14* KO cells in mRNA expression (Figure 2.4C). Notably, *Foxo1* and BCR recombination effectors *Rag1*, *Rag2*, and *Dntt* were higher in the KO group (Figure 2.4D). These data suggest that loss of METTL14 results in abnormal regulation of genes involved in both cell cycle and BCR recombination machinery in the large pre-B cells.

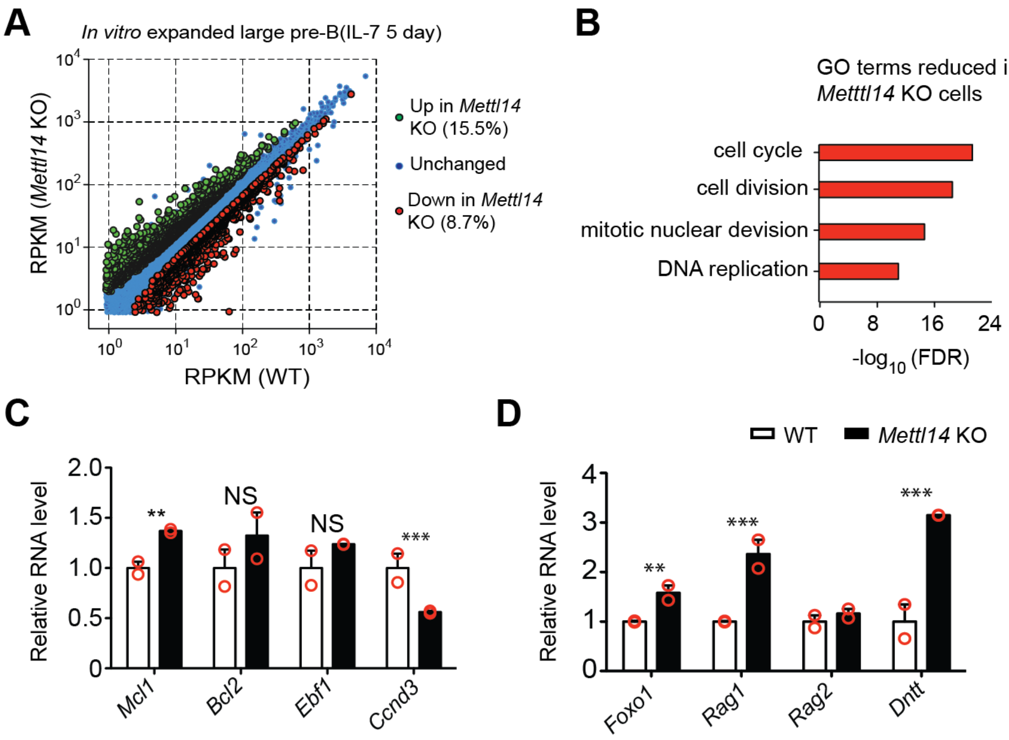

Figure 2.4 METTL14 regulates genes involved in cell cycle

(**A**) Scatter plot of gene expression differences between *Mettl14* KO and WT large pre-B cells identified by RNA-seq. (**B**) Reduced DEGs in the *Mettl14* KO large pre-B cells were subject to GO term enrichment analysis. Top terms related "cell cycle" are shown. (**C**) Relative RNA levels of indicated genes in *Mettl14* KO large pre-B cells versus WT controls. (**D**) Comparison of the expression of indicated genes between WT and *Mettl14* KO large pre-B cells.

To further understand how *Mettl14* deficiency blocks the transition from the CD2$^-$ stage to the CD2$^+$ stage, we withdrew IL-7 from the *in vitro* expanded large pre-B cells. After IL-7 removal, a large portion of the WT large pre-B cells differentiated to CD2$^+$ small pre-B cells and Igκ/λ$^+$ immature B cells, but *Mettl14* KO large pre-B cells were unable to do so (Figure 2.5A), which is consistent with the major block observed *in vivo* (Figure 2.1C-D). *Mettl14* KO pre-B cells also remained more proliferative than WT controls after IL-7 removal (Figure 2.5B), indicating that *Mettl14* deficiency impairs the exit from cell cycle in large pre-B cells. Furthermore, *Mettl14* KO cells were unable to rearrange Igκ (Figure 2.5C) or downregulate the pre-BCR component VPREB (Figure 2.5D), as WT cells do during this transition. These data indicated that *Mettl14* deficiency blocks the differentiation to the small pre-B stage.

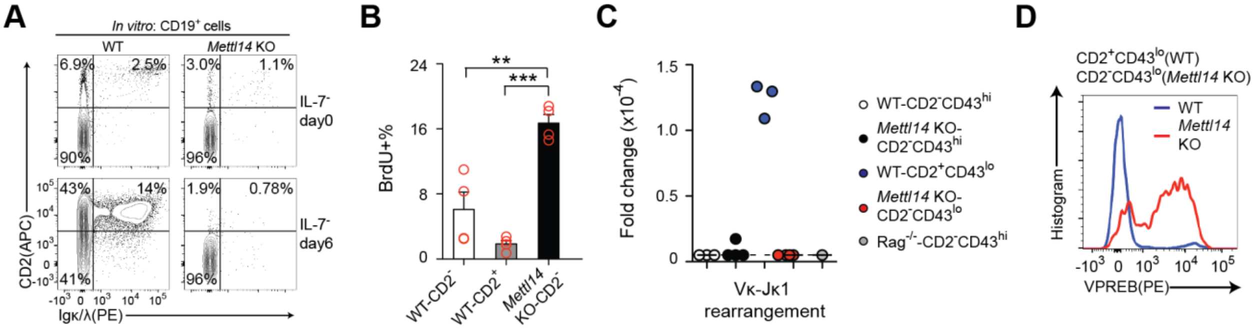

Figure 2.5 Loss of METTL14 blocks the large-pre-B to small-pre-B transition

(**A**) Flow cytometry plots of indicated markers in CD19$^+$ cells of indicated groups before or 6 days after IL-7 removal. (**B**) BrdU was added to the cell culture for 45 min on day 4 after IL-7 removal. BrdU$^+$ percentages in indicated CD19$^+$Igκ/λ$^-$ cells are shown. (**C**) Quantitative PCR of Vκ1-Jκ1 recombination with the genomic DNAs from indicated CD19$^+$B220^{mid}Igκ/λ$^-$ subpopulations sorted from indicated mice. (**D**) Intracellular staining of VPREB in indicated CD19$^+$B220^{mid}Igκ/λ$^-$ subpopulations from indicated mice.

RNA-seq analysis showed that, upon IL-7 removal, although the majority of both upregulated and downregulated genes in the WT cells also followed the same trend in *Mettl14* KO cells (Figure 2.6A), the fold changes in *Mettl14* KO group were significantly smaller (Figure 2.6B). Gene ontology analysis identified a large group of genes related to cell cycle as well as the pre-BCR components (*Vpreb* and *Igll1*) in the inadequately downregulated genes due to *Mettl14* deficiency (Figure 2.6C), consistent with that these cells failed to cease proliferation (Figure 2.5B) and downregulate pre-BCR components (Figure 2.5D). The inadequately upregulated genes include key TFs mediating the large-pre-B-to-small-pre-B transition (*Ikzf3*, *Irf4*, *Spib*, and *Bcl6*), B cell markers (*Ptprc*, *Il2ra*, and *Cd93*), BCR signaling components (*Syk*, *Lyn*, and *Cd79b*), BCR recombination components (*Rag1* and *Rag2*), and proliferation inhibitors (*Cdkn1b*; Figure 2.6D). These data demonstrated that *Mettl14* KO large pre-B cells are unable to completely switch the gene expression program during the transition from the large pre-B stage to the small pre-B stage.

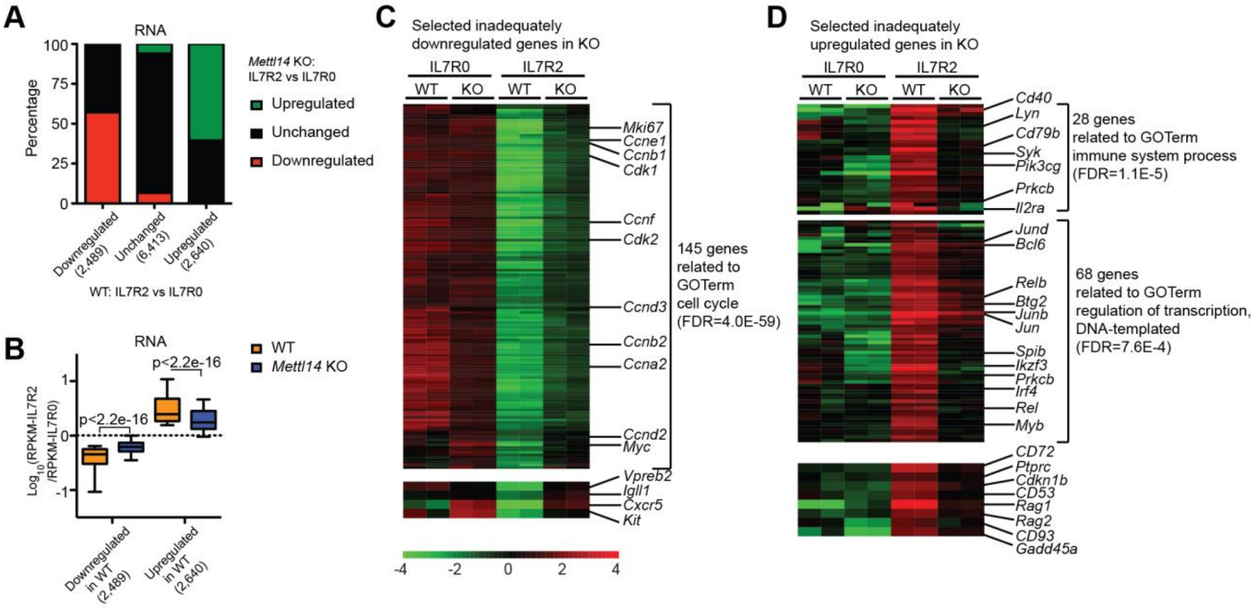

Figure 2.6 Transcriptome analysis of large pre-B cells upon IL-7 removal

WT and KO CD19$^+$CD2$^-$Igκ/λ$^-$ cells before (IL7R0) or 2 days after IL-7 removal (IL7R2) were sorted and subject to RNA-seq analysis. Expressed genes were first grouped by comparing WT-IL7R2 and WT-IL7R0 samples. (**A**) The distribution of DEGs between KO-IL7R2 and KO-IL7R0 samples in each group. (**B**) The IL-7 removal-induced fold changes of genes from indicated groups are compared between WT and KO samples. (**C**) and (**D**) Heatmaps of selected inadequately downregulated (**C**) and inadequately upregulated (**D**) genes in the KO large pre-B cells upon IL-7 removal.

2.2.3 METTL14 installs m^{6}A onto a wide range of transcripts in developing B cells

To link mRNA m^{6}A to B cell development, we mapped the whole transcriptome m^{6}A of developing B cells by m^{6}A-seq. Over 7,000 highly confident m^{6}A sites were identified in WT *ex vivo* sorted pro-B cells and *in vitro* expanded large pre-B cells, enriched with the m^{6}A consensus motif GGACU(G) identified before[103] (Figure 2.7A). m^{6}A is primarily enriched in the CDS (coding sequence) and 3′ UTR surrounding the stop codons in developing B cells (Figure 2.7B), as the case in cell lines and other tissues[4,103]. m^{6}A-labeled genes identified in two stages showed large overlap (Figure 2.7C). These data indicated that the m^{6}A methylation is widely distributed in the transcriptome of developing B cells.

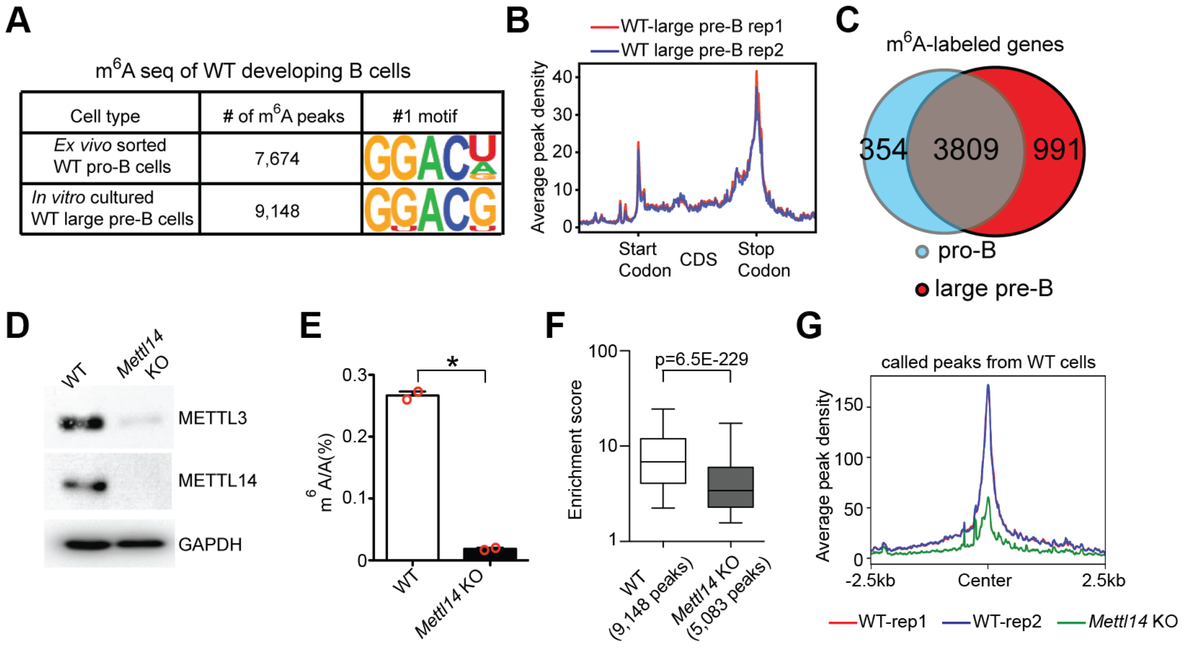

Figure 2.7 METTL14 installs m^{6}A onto transcripts in developing B cells

(**A**) Numbers of m^{6}A peaks identified in indicated cells and their top consensus sequences. (**B**) Metagene profiles of enrichment of m^{6}A modifications across the whole transcriptome in the two WT large pre-B cell biological replicates. (**C**) Overlapping of m^{6}A-labeled genes identified in WT pro-B cells and in WT large pre-B cells. (**D**) Western blot against indicated proteins in *in vitro* expanded large pre-B cells. (**E**) Quantification of m^{6}A methylation by LC-MS/MS in the poly-A enriched mRNAs from indicated *in vitro* expanded large pre-B cells. (**F**) Fold enrichment scores of called peaks from indicated groups were compared. Box and whisker (5–95 percentile) plots were shown. p value was calculated by Mann-Whitney-Wilcoxon test. (**G**) Global comparison of the peaks identified in indicated groups between all samples.

Loss of METTL14 caused disappearance of the whole METTL3/METTL14 core in the large pre-B cells (Figure 2.7D), which is consistent with observations in T cells[38]. Quantification of m^{6}A in poly-A-enriched mRNAs by mass spectrometry showed that the *Mettl14* KO large pre-B cells had a 93% reduction in the mRNA m^{6}A level compared to the WT controls (Figure 2.7E). Similarly, by m^{6}A-seq, significantly lower enrichment scores (Figure 2.7F) and peak density

(Figure 2.7G), were identified in *Mettl14* KO large pre-B cells (5,083 peaks) than in WT counterparts (9,148 peaks)

2.2.4 m^{6}A modulates IL-7-induced pro-B cell proliferation by suppressing a group of YTHDF2-bound transcripts

Consistent with the well-established notion that m^{6}A inversely correlates with mRNA stability, in large pre-B cells, m^{6}A-labeled genes are more likely to have increased mRNA levels in the absence of METTL14 (Figure 2.8A-B). A strong correlation between higher m^{6}A labeling in transcripts and higher gene expression levels in *Mettl14* KO cells was also detected (Figure 2.8C-D), suggesting that m^{6}A directly decreases the mRNA levels of a group of genes.

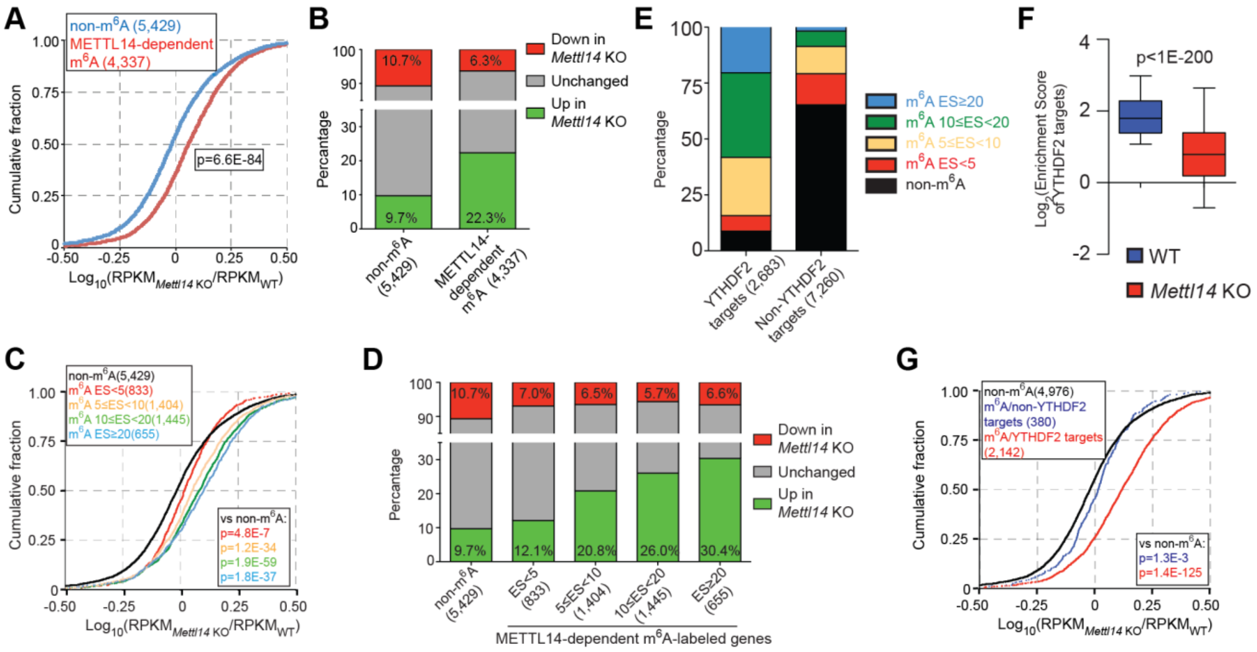

Figure 2.8 Methylation by METTL14 destabilizes mRNA bound by YTHDF2

(**A**) Cumulated distribution of *log$_{10}$* fold changes between *Metl14* KO cells and WT cells for non-m^{6}A-labeled genes (blue) and METTL14-dependent m^{6}A-labeled genes (red). (**B**) Distribution of DEGs identified by RNA-seq from the *Mettl14* KO large pre-B cells in non-m^{6}A-labeled genes and METTL14-dependent m^{6}A-labeled genes. (**C**) Cumulated distribution of RPKM *log10* fold changes between *Metl14* KO cells and WT cells for non- m6A-labeled genes (black) and METTL14-dependent m6A-labeled genes with different m6A levels. (**D**) Distribution of DEGs identified by RNA-seq from *Mettl14* KO large pre-B cells in non-m6A-labeled genes and METTL14-dependent m6A-labeled genes with different m6A levels. (**E**) WT and *Mettl14* KO

(**Figure 2.8, continued**) large pre-B (CD19$^+$CD2$^-$Igκ/λ$^-$) cells were sorted after 5-day expansion with IL-7 *in vitro* and subject to YTHDF2 RIP-seq. Distribution of genes with different mRNA m6A levels in YTHDF2 targets and non-YTHDF2 targets is shown. (**F**) *Log2* YTHDF2 RIP enrichment scores of YTHDF2 targets identified in the WT cells were compared between WT and *Mettl14* KO group. (**G**) Cumulated distribution of log_{10} fold changes between *Mettl14* KO cells and WT cells for non-m^{6}A-labeled genes, non-YTHDF2-bound, METTL14-dependent, m^{6}A-labeled genes, and YTHDF2-bound, METTL14-dependent, m^{6}A-labeled genes

YTHDF2-mediated decay is a well-known mechanism by which m^{6}A decreases mRNA levels[27]. To investigate whether the elevated expression of m^{6}A-labeled genes in the KO cells was linked to YTHDF2, we identified transcripts bound by YTHDF2 in developing B cells by RNA immunoprecipitation and sequencing (RIP-seq). YTHDF2 clearly showed a preference to recognize m^{6}A-containing transcripts (Figure 2.8E), and loss of METTL14 significantly reduced the binding of YTHDF2 to the majority of its targets (Figure 2.8F). Importantly, among the heavily m^{6}A-labeled transcripts, only YTHDF2-bound transcripts were more likely to be elevated in the *Mettl14* KO cells (Figure 2.8G). These data strongly suggested that m^{6}A directly decreases a group of transcripts via YTHDF2 in developing B cells.

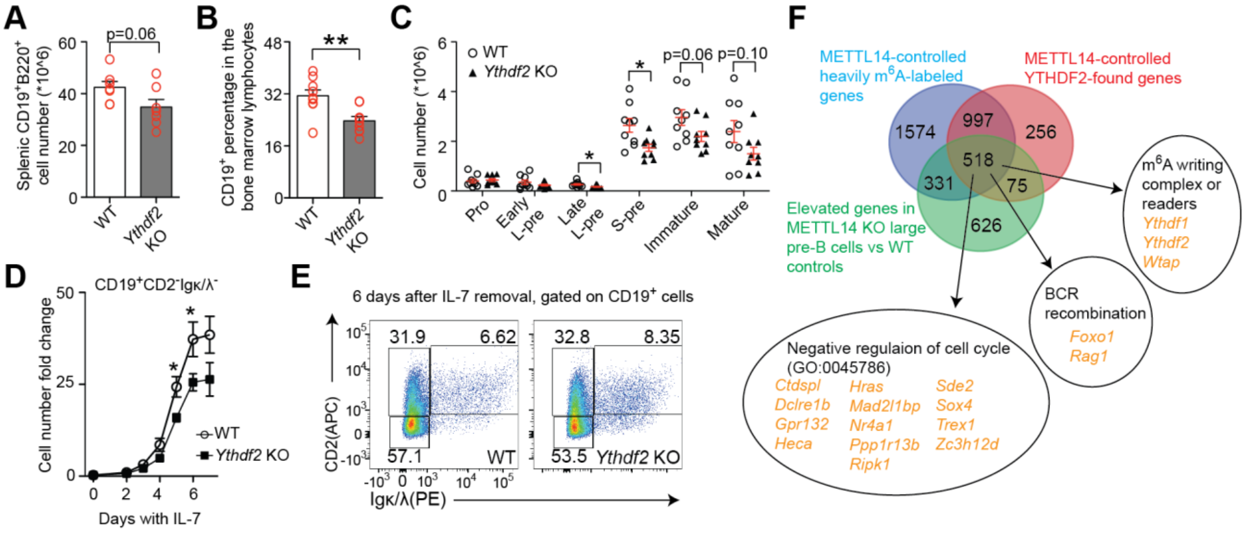

Figure 2.9 m^{6}A regulates IL-7 induced pro-B cell proliferation through YTHDF2

(**A**) Quantification of splenic B cells in indicated mice. (**B**) The percentages of CD19$^+$ cells in the bone marrow cells in indicated mice. (**C**) The numbers of indicated populations in indicated mice. (**D**) Fold changes of the CD19$^+$CD2$^-$Igκ/λ$^-$ cells at indicated times during IL-7-induced expansion.

(**Figure 2.9, continued**) (**E**) Flow cytometry plots of indicated markers in CD19$^+$ cells of indicated groups 6 days after IL-7 removal. (**F**) Identification of the 518 YTHDF2-suppressed m^{6}A-labeled genes in large pre-B cells.

Next, we generated *Mb1*$^{cre/+}$*Ythdf2*$^{fl/fl}$ (*Ythdf2* KO) mice to evaluate the role of YTHDF2 in B cell development. We found that loss of YTHDF2 caused a 20% reduction of B cells in the spleen (Figure 2.9A). A significant block between the pro-B stage and the late large pre-B stage was detected in the bone marrow of the *Ythdf2* KO mice (Figure 2.9B-C), but this block was milder than the one observed in the *Mettl14*KO mice (Figure 2.1C-D). *In vitro*, *Ythdf2* KO B-lineage cells exhibited a significant defect in the IL-7-induced expansion compared to WT controls (Figure 2.9D). However, loss of YTHDF2 did not cause any detectable block during the large-pre-B-to-small-pre-B transition *in vitro* (Figure 2.9E). These data indicated that the mRNA m^{6}A mediates the IL-7-induced pro-B cell proliferation via YTHDF2 but modulates the large-pre-B-to-small-pre-B transition in an YTHDF2-independent way.

By integrative analysis of three sequencing datasets, we identified 518 genes as m^{6}A-labeled, YTHDF2-recognized genes whose expressions were suppressed by m^{6}A in the large pre-B cells (Figure 2.9F). These genes contained a group of genes known to negatively regulate cell cycle, which is consistent with the decreased proliferation observed in *Mettl14* KO large pre-B cells. Both *Foxo1* and *Rag1* are among the list, suggesting that the YTHDF2-mediated RNA decay might also be critical to tuning down BCR recombination machinery[104]. Interestingly, *Ythdf1* and *Ythdf2*, together with *Wtap*, an important component of the m^{6}A writing complex[23,105], are also present in the list, suggesting that the gene-suppression effect of m^{6}A could also impact its readers and writers.

2.3 Discussion and conclusion

Two separate blocks in B cell development due to *Mettl14* deficiency were clearly identified. They coincide with transitions of proliferation and recombination, strongly supporting the proposed role of m^6A in coordinating gene expression switch during cell state transitions[8,40,106]. The latter block during the large-pre-B-to-small-pre-B transition is the major defect in B cell development in *Mettl14* KO mice. In contrast, the contribution of the defective IL-7-induced pro-B cell proliferation is relatively minor, as it only leads to reduced pro-B/early large pre-B cell proliferation in the *Mettl14* KO mice. The significant defect in the IL-7-induced pro-B cell proliferation but very mild reduction in peripheral B cell numbers in the *Ythdf2* KO mice also supports this conclusion. In two recent studies[33,34], Mx1-Cre inducible *Mettl3* conditional KO mice were generated to study the roles of m^6A in hematopoietic stem cell identity and symmetric commitment. Both studies showed that there were no major defects in the bone marrow B cells after poly I:C treatment-induced *Mettl3* deletion. Given the fast turnover of immature B cells and our data on early B cell developmental blocks, the unaffected immature B cell number in these mice might result from incomplete deletion of *Mettl3* in the B lineage cells. However, it is also possible that RNA m^6A methylation is not essential for the maintenance and survival of mature B cells once they have reached this stage.

mRNA m^6A has been shown to inversely correlate with mRNA stability[27,103]. Loss of METTL3 or METTL14 causes elevations of m^6A-containing transcripts in various cell types, and the subsequent increased expression of key m^6A-labeled genes has been linked to abnormalities in these cells[8,35,36,38]. Our previous study identified the YTHDF2-mediated mRNA decay as a main regulatory pathway to post-transcriptionally reduce mRNA levels, which had been shown critical in processes such as embryo development[41] and hematopoietic stem cell expansion[107]. Here, we found that, in developing B cells, loss of METTL14 also reduced the binding of YTHDF2 to its targets and specifically caused the elevations of a group of YTHDF2-bound transcripts. Both loss of METTL14 and loss of YTHDF2 caused significant block during the IL-7-induced pro-B cell proliferation, indicating that the YTHDF2-mediated mRNA decay is critical to the transition from the pro-B stage to the large pre-B stage. Interestingly, loss of METTL14 causes block between the large pre-B stage and the small pre-B stage via a different mechanism. Loss of YTHDF2 alone does not affect this transition. METTL14 depletion also dramatically decays METTL3. These two proteins may play additional roles in the nucleus or affect stability of certain regulatory non-coding RNAs[28]. We suspect it could be a combination of some of these potential pathways that warrants future investigations.

In summary, our data demonstrate important regulatory roles of the mRNA m^6A methylation in early B cell development. The RNA m^6A methylation modulates two cellular transitions by different mechanisms. The installation of m^6A onto mRNA by the METTL3-METTL14 complex is important for the IL-7-induced pro-B cell proliferation through post-transcriptional reduction of a group of transcripts by YTHDF2. In contrast, the large-pre-B-to-small-pre-B transition is controlled by regulating gene expression at the transcriptional level.

2.4 Methods

2.4.1 Materials

Antibodies for flow cytometry and western blotting used in this study are listed below.

Table 1: Antibodies for flow cytometry and western blotting

Antibodies	SOURCE	IDENTIFIER
APC-cy7 anti-mouse B220 antibody	Biolegend	RRID: AB_313007
PE anti-mouse B220 antibody	Biolegend	RRID: AB_312993
Brilliant Violet 421 anti-mouse CD19 antibody	Biolegend	RRID: AB_10895761
FITC anti-mouse CD19 antibody	Biolegend	RRID: AB_313641
APC anti-mouse CD19 antibody	Biolegend	RRID: AB_313647

(**Table 1, continued**)

PE Anti-mouse Igκ antibody	Biolegend	RRID: AB_2563581
FITC Anti-mouse Igκ antibody	Biolegend	RRID: AB_2563585
Biotin anti-mouse Igλ antibody	Biolegend	RRID: AB_345332
PE anti-mouse Igλ antibody	Biolegend	RRID: AB_1027659
PE-cy7 anti-mouse CD43 antibody	Biolegend	RRID: AB_2564349
FITC anti-mouse CD2 antibody	Biolegend	RRID: AB_312652
APC anti-mouse CD2 antibody	Biolegend	RRID: AB_2563090
Brilliant Violet 711 anti-mouse c-Kit antibody	Biolegend	RRID: AB_2565956
APC anti-mouse CD25 antibody	Biolegend	RRID: AB_312861
FITC anti-mouse Ly-51(BP-1) antibody	Biolegend	RRID: AB_313362
FITC anti-mouse CD4 antibody	Biolegend	RRID: AB_312691
APC anti-mouse CD24 antibody	Biolegend	RRID: AB_2565651
APC anti-mouse IL-7Rα antibody	Biolegend	RRID: AB_1937216
PE anti-mouse VpreB antibody	Biolegend	RRID: AB_11150774
FITC anti-mouse IgM antibody	BD Biosciences	RRID: AB_394857
FITC anti-BrdU antibody	BD Biosciences	RRID: AB_396304
Rabbit anti-METTL3 antibody	Cell Signaling Technology	RRID: AB_2800072
Rabbit anti-METTL14 antibody	Cell Signaling Technology	RRID: AB_2799383
HRP-conjugated Rabbit anti-GAPDH (D16H11)	Cell Signaling Technology	RRID: AB_11129865
HRP-conjugated anti-rabbit IgG	Cell Signaling Technology	RRID: AB_2099233
anti-m^{6}A antibody	New England Biolabs	Catalog#:E1610s
anti-YTHDF2 antibody	Aviva Systems Biology	Catalog#:ARP67917_P050

2.4.2 Mice

Mb1-cre[108], *Mettl14*-floxed[109], *Ythdf2*-floxed[10], and SW$_{\text{HEL}}$[110] mice have been described previously. *Rag1*$^{-/-}$[111] mice were purchased from the Jackson Laboratory. All mice were housed in a specific pathogen-free facility. Both males and females were used. Mice were used 6 to 24 weeks of age and all the experiments were approved by the University of Chicago Institutional Animal Care and Use Committee.

2.4.3 *In vitro* culture of B cell progenitors

B220$^+$ cells were enriched from the bone marrow of mice by positively selecting B220$^+$ cells with biotin-conjugated anti-mouse B220 antibody (Biolegend), the anti-Biotin MicroBeads (Miltenyi Biotec) and the LS column (Miltenyi Biotec). Enriched B220$^+$ cells were co-cultured with OP9 cells in the culture medium (OPTI-MEM media supplemented with 10% FBS, 0.05 mM 2-mercaptoethanol, 100 units/ml penicillin, 100 μg/mL streptomycin, and 2 mM glutamine) with 15 ng/mL IL-7 (Biolegend) for indicated times. For IL-7 removal, co-cultured B cell progenitors and OP9 cells were washed twice with pre-warmed medium without IL-7 and continued to be cultured in the same medium without IL-7 for indicated times.

2.4.4 Flow cytometry

Cells were stained with fluorochrome-conjugated antibodies against surface antigens in DPBS (Thermo Fisher Scientific) containing 2% FBS (Thermo Fisher Scientific) prior to analysis, cell sorting or intracellular staining. To stain intracellular Igμ, Igκ or VPREB, cells were fixed and permeabilized with a fixation/permeabilization solution (BD Biosciences) before being stained for intracellular proteins. Labeled cells were analyzed on a BD LSR II or a BD LSRFortessa, or sorted on a BD FACSAria, using Diva software (BD Biosciences). Flow cytometric data were analyzed using FlowJo software (BD Biosciences). Antibodies used are listed under materials.

2.4.5 *In vivo* and *in vitro* proliferation assays

For *in vivo* BrdU labeling, one milligram of BrdU (Sigma) in 100 μL DPBS per mouse was injected intraperitoneally, before mice were sacrificed one hour later and BrdU cooperation in various B cell subpopulations was analyzed. For *in vitro* labeling, BrdU was added to the cell culture at a concentration of 10 μM for 45 minutes at indicated time points. BrdU staining was performed with the BrdU flow cytometry kit following manufacturer instructions (BD

Biosciences). For CFSE dilution assay, the CellTrace CFSE kit (Invitrogen) was used to label cells with CFSE.

2.4.6 Quantification of cells

Spleens were mashed between 2 frosted microscope slides. Peritoneal cells were collected by injecting 5 mL PBS to the peritoneal cavity of mouse to wash out cells. Bone marrow cells were collected by mashing bones with mortar and pestle. Splenocytes, peritoneal cavity cells, and bone marrow cells were counted using hemocytometer after red blood cells were lysed with ACK RBC lysis buffer, and the cells were filtered. For bone marrow cells, the cell numbers represent either 2 (femur + humerus + tibia) per mouse or 2 femurs per mouse. For *in vitro* cultured cells, floating and attached cells were combined for counting. Attached cells were collected by incubating cells with 0.05% Trypsin/EDTA (Thermo Fisher Scientific) for 5 minutes. The cultured cells were counted by flow cytometry with counting beads (Thermo Fisher Scientific).

2.4.7 PCR and quantitative PCR

The primers used for amplifying the *Mettl14* flox and deleted alleles were: Forward common: CTGCCAAGAAAATGGAAAA; Flox reverse: TGCAGCCCCACAATTATAGC; Deleted reverse: GGGACTGGGAACACTTGAAA. Primers for quantitative PCR of Vκ1-Jκ1 rearrangement with genomic DNA were as previously reported[112]. Primers “a” and “b” from the referenced paper were used for the qPCR of the recombined Vκ1-Jκ1, while primers “b” and “c” were used for internal control reaction. Primers for quantitative PCR of recombination of various IgH families with genomic DNA were as previously reported[113] and *Hprt* was used as internal control.

2.4.8 RNA sequencing and data analysis

Total RNA from sorted cells was extracted with TRIzol (Thermo Fisher Scientific). Polyadenylated RNA was enriched with Dynabeads mRNA DIRECT Purification Kit (Invitrogen). The sequencing library was generated with SMARTer Stranded Total RNA-Seq Kit (Takara). All sequencing was performed by the Genomics Facility at the University of Chicago. Raw sequencing reads were trimmed by Trim_Galore software (https://www.bioinformatics.babraham.ac.uk/projects/trim_galore/) to remove adaptor sequences and low-quality nucleotides. Clean reads were then mapped to the mm9 or mm10 reference genome using Hisat[114], and only uniquely mapped reads were kept for the following analyses. Cuffnorm[115] were used to calculate RPKM for all samples. Fold changes and FDRs were determined by Cuffdiff[115] with default parameters. Deferentially expressed genes between different groups were defined as genes with fold change > 1.5 and FDR < 0.05. GO term analysis was conducted with the Database for Annotation, Visualization and Integrated Discovery (DAVID)[116]. Heatmaps were made with Cluster 3.0 (http://bonsai.hgc.jp/~mdehoon/software/cluster/) and Java Treeview[117] (http://jtreeview.sourceforge.net/).

2.4.9 mRNA m^{6}A quantification by LC-MS/MS

Polyadenylated RNA from sorted cells was enriched with Dynabeads mRNA DIRECT Purification Kit (Invitrogen), digested with nuclease P1 (Wako) and dephosphorylated with FastAP Thermosensitive Alkaline Phosphatase (Thermo Fisher Scientifics). Then the samples were filtered and quantified by Agilent 6410 QQQ triple-quadrupole LC mass spectrometer.

2.4.10 m^{6}A seq and data analysis

Briefly, polyadenylated RNA isolated from indicated cells was fragmented to ~100 nt with sonication. Four percent of the fragmented RNA was preserved as input. The rest was subject to m^{6}A immunoprecipitation using the EpiMark *N*^{6}-Methyladenosine Enrichment Kit (NEB). RNA was concentrated with RNA Clean & Concentractor-5 (Zymo Research) and the library was constructed with the SMARTer Stranded Total RNA-Seq Kit (Takara). IP and Input sequencing data were sent to Trim-Galore to remove low quality reads and adaptor sequence contaminants under default parameters except for "–length 50." Remaining reads were then aligned to the mouse transcriptome annotation based on mm9 assembly using hisat2[114] aligner (v2.1.0), with default parameters being used. Peaks enriched in the IP samples versus input or enriched in WT versus *Mettl14* KO samples were identified using exomePeak[118] with default parameters. Profiles of m^{6}A tag density were generated by plotProfile tool in deeptools 2.0 tool suite[119]. For motif search, identified peaks were sorted according to the *p* values from lowest to highest, then the top 1000 peaks were chosen for the *de novo* motif analysis using HOMER Motif discovery tools. Expressed genes (defined by RNA-seq) with at least one peak called with enrichment score > 2 (IP versus Input) in the WT group was defined as m^{6}A-labeled genes. m^{6}A-labeled genes with at least one peak significantly reduced by over two-fold in the *Mettl14* KO group versus WT group were defined as METTL14-dependent m^{6}A-labeled genes.

2.4.11 YTHDF2 RIP-seq and data analysis

Sorted cells were lysed with lysis buffer (50 mM HEPES, pH 7.4, 150 mM KCl, 2 mM EDTA, 0.5% NP40, 0.5 mM DTT, protease inhibitor, RNase Inhibitor) on ice for 30 minutes. The lysate was spin at 21,000 × g for 15 minutes. To pre-clear, the supernatant was incubated with Protein G beads (Invitrogen) at 4 °C for 1 hr. 5% of the lysate was kept as input. Antibody against YTHDF2 (Aviva Systems biology) was conjugated to Protein G beads. The protein-bead conjugate was added to the lysate and incubated for 4 hours. Beads were washed 6 times with NT2 buffer (50 mM HEPES, pH 7.4, 200 mM NaCl, 2 mM EDTA, 0.05% NP40, 0.5 mM DTT, protease inhibitor, RNase inhibitor). RNA was eluted with TRIzol and library was constructed as described above. Reads from RIP-seq experiments were mapped to mm9 mouse genome sequence by hisat2[114], with the parameters setting as –rna-strandness R –mp 6,2 -k 5 –score-min L,0,-0.2. The FPKM value for each gene was calculated with Cufflinks[115]. The number of the reads assigned to each gene was counted by the function of featureCounts from R package Rsubread [120]. The target genes of YTHDF2 in WT and METTL14 KO samples were identified by the R package DESeq2[121]. The genes with p value less than 0.05 and log2 fold change bigger than 2 in RIP data contrast to input were defined as YTHDF2 target genes.

2.4.12 Statistical analysis

Differences between different comparisons were tested using two-tailed Student's t test for data analysis. NS, not significant; *, $p < 0.05$; **, $p < 0.01$; and ***, $p < 0.001$. RNA-seq analysis, the FDR of individual genes between samples were calculated by Cuffdiff. In m^6A-seq and YTHDF2 RIP-seq analysis, the p values of individual gens between samples were calculated by exomePeak R/Bioconductor package or R package DESeq2, respectively.

2.4.13 Data availability

The accession numbers for the RNA-seq, m^6A-seq, and YTHDF2 RIP-seq data reported in this paper are Gene Expression Omnibus (GEO): GSE 112022, GSE 136419, and GSE 151071.

Chapter 3

YTHDF2-m^{6}A-NF-κB axis controls anti-tumor immunity by regulating intratumoral Tregs

3.1 Introduction: The role of m^{6}A in anti-tumor immunity

The checkpoint blockade anti-cancer immunotherapy has had increasing clinical successes[122]. One major effort in cancer immunotherapy is to overcome the suppressive tumor microenvironment (TME) generated by suppressor cells such as regulatory T (Treg) cells. Treg cells are suppressive T cells expressing transcription factor forkhead box protein P3 (FOXP3)[123]. These cells balance immune response, maintain peripheral homeostasis, and prevent inflammation[124,125]. The infiltration of Treg cells in tumors is often associated with tumor progression and poor prognosis[126]. Various antibodies showed anti-tumor activity through Treg cell depletion, leading to tumor regression and prolonged survival[127–130]. However, growing clinical studies of antibody-based drugs and cellular treatments targeting Treg cells have revealed inflammations and other complications in patients[131]. Effective targets that can precisely regulate intratumoral Treg cells are needed to improve immunotherapy efficacy while avoiding peripheral side effects.

N^6-methyladenosine (m^{6}A) modification regulates many aspects of mRNA metabolism, including transcription, splicing, translation, and decay[20,132]. m^{6}A-related pathways are emerging targets for cancer treatments due to their functions in regulating tumor cell survival and propagation[133,134]. Beyond tumor cells, m^{6}A has also been revealed to regulate tumor-infiltrating immune cells. For example, YTHDF1, an m^{6}A reader protein that promotes the translation of m^{6}A-modified transcripts, regulates the antigen presentation function of dendritic cells by promoting the translation of m^{6}A-modified proteases transcripts. Depletion of YTHDF1 can notably enhance anti-tumor immunity[37]. Additionally, YTHDF2, another m^{6}A reader protein that facilitates m^{6}A-modified mRNA degradation, has been shown to sustain natural killer cell survival and function in the tumor[51].

In T cells, m^{6}A-related pathways play a role in regulating homeostasis. Specifically, the m^{6}A methylase METTL3 regulates the IL7-STAT5 signaling pathway to maintain naïve T cell survival[38]. Deletion of either one of the methyltransferase components METTL3 or METTL14 leads to dysfunctional Treg cells and autoimmunity[44,47]. However, the mechanism by which reader proteins orchestrate m^{6}A regulation in Treg cells remains unknown. Furthermore, transcriptome profiles of Treg cells in the tumors *versus* healthy tissues are largely different[135,136]. Numerous examples have demonstrated that the m^{6}A pathway can respond to environmental stimuli[137–139], and whether this nature facilitates the location-specific features of Treg cells has not been explored.

3.2 Results

3.2.1 *Ythdf2*-depleted Treg cells inhibit tumor growth

Alteration of the m^{6}A profile by *Mettl3*/*Mettl14* deletion in Treg cells can lead to fatal autoimmunity [44,47]. However, dysfunctional Treg cells can be beneficial for immune activation to eradicate tumor cells. METLL3 and METTL14 deposit m^{6}A to both mRNA and chromosome-associated RNA to broadly affect cell differentiation and survival[140]. We reasoned that distinct m^{6}A reader proteins control subsets of m^{6}A-modified transcripts, the depletion of which in Treg may affect TME-specific response without affecting peripheral functions of Treg cells. We focused on YTHDF2 as this m^{6}A reader is essential for the turnover of methylated transcriptomes in mammalian cells upon cell differentiation or signaling[41,141,142].

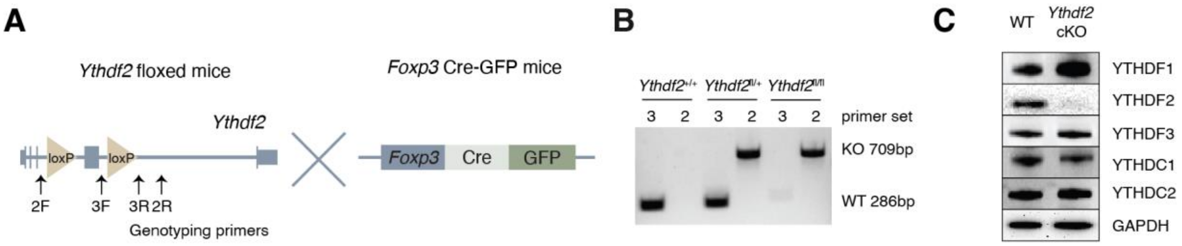

Figure 3.1 Validation of *Foxp*3$^{\text{Cre}}$*Ythdf2*$^{\text{fl/fl}}$ mice

(**A**) Breeding scheme to generate *Foxp*3$^{\text{Cre}}$*Ythdf2*$^{\text{fl/fl}}$ mice. Primer pairs 2 and 3 at the indicated locations were used for genotyping by PCR. (**B**) Representative PCR products of FOXP3 Treg cells from indicated mice using genotyping primers. (**C**) Western blot analysis of YTH proteins expression in FOXP3 Treg cells from WT and *Ythdf2* cKO mice.

To evaluate the role of YTHDF2 in regulating tumor-infiltrating Treg cells, we generated Treg-specific *Ythdf2* deletion by crossing *Ythdf2*-floxed mice with *Foxp3*-CreGFP mice (*Foxp*3$^{\text{Cre}}$*Ythdf2*$^{\text{fl/fl}}$, *Ythdf2* cKO) (Figure 3.1A). Treg cells from *Ythdf2* cKO mice had an efficient deletion of *Ythdf2*. (Figure 3.1B) n increase of YTHDF1 expression was observed, but other YTH reader proteins displayed similar expression levels when compared with the WT Treg cells (Figure 3.1C). We inoculated mouse melanoma tumor cells B16F10 into these mice to follow tumor development. Compared to tumors developed in control (*Foxp*3$^{\text{Cre}}$*Ythdf2*$^{\text{fl/+}}$, WT) mice, B16F10 tumors developed in *Ythdf2* cKO mice showed a slower growth rate and smaller tumor weight (Figure 3.2A). Similar results were observed with colon carcinoma cells MC38 (Figure 3.2B). These data suggested that YTHDF2 depletion in Treg cells has anti-tumor effect.

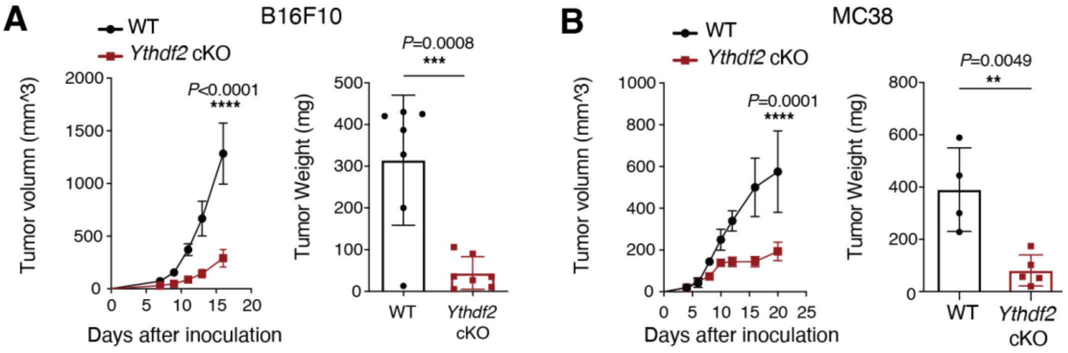

Figure 3.2 *Ythdf2*-deficient Treg cells inhibit tumor growth rate

(**Figure 3.2, continued**) (**A**) B16F10 melanoma tumor growth (left) in WT (*Foxp*3$^{\text{Cre}}$*Ythdf2*$^{\text{fl/+}}$) or *Ythdf2* cKO (*Foxp*3$^{\text{Cre}}$*Ythdf2*$^{\text{fl/fl}}$) mice. Data are presented as means ± s.e.m. and analyzed by two-way ANOVA. Tumors were harvested 16 days post-tumor inoculation for weight measurements (right). Data are presented as means ± s.d. and analyzed by two-tailed unpaired Student's *t*-test. (**B**) MC38 colon carcinoma tumor growth (left) in WT or *Ythdf2* cKO mice. Data are presented as means ± s.e.m. and analyzed by two-way ANOVA. Tumors were harvested 21 days post-tumor inoculation for weight measurements (right). Data are presented as means ± s.d. and analyzed by two-tailed unpaired Student's *t*-test.

Treg cells are known to create an immunosuppressive TME and suppress effector T cell response and proliferation[143,144]. To examine the effect of *Ythdf2* cKO Treg cells in the TME, we profiled B16F10 tumor-infiltrating immune cells from both WT and *Ythdf2* cKO mice by flow cytometry. *Ythdf2* cKO mice showed differences in Treg and CD8$^+$ T cell infiltration, where the infiltration of other immune cells remained comparable (Figure 3.3A). Tumors developed in *Ythdf2* cKO mice had an increased ratio and cell count of tumor-infiltrating CD8$^+$ T cells (Fig Figure 3.3B). Furthermore, tumor-infiltrating CD8$^+$ T cells in *Ythdf2* cKO mice showed an increased percentage of INFγ-producing population (Figure 3.3C), suggesting a less immunosuppressive TME with *Ythdf2* cKO Treg cells than with WT Treg cells. While the ratio of CD4$^+$ T cells was unchanged (Figure 3.3A), the T$_{\text{H}}$1 subset, which promotes anti-tumor immunity[145], was increased (Figure 3.3D).

The ratio and absolute cell count of Treg cell infiltration were decreased in *Ythdf2* cKO mice (Figure 3.4A), but Treg signature marker FOXP3 expression level was unchanged (Figure 3.4B). Meanwhile, markers that characterize intratumoral Treg cells, including OX40, TIGIT, and NRP1, were not affected by *Ythdf2* deletion (Figure 3.4C). Therefore, YTHDF2 depletion does not appear to notably alter Treg cell identity. Only a marginally significant reduction in PD-1 high population was observed in intratumoral Treg cells from *Ythdf2* cKO mice compared with the WT Treg cells (Figure 3.4C). How PD-1 regulates Treg cells is still unclear, but infiltration of PD-1 expressing Treg cells has been associated with tumor progression[146]. Taken together, loss of *Ythdf2* in Treg cells elevated immune response at the tumor site through reducing Treg cell infiltration, rather than altering Treg identity.

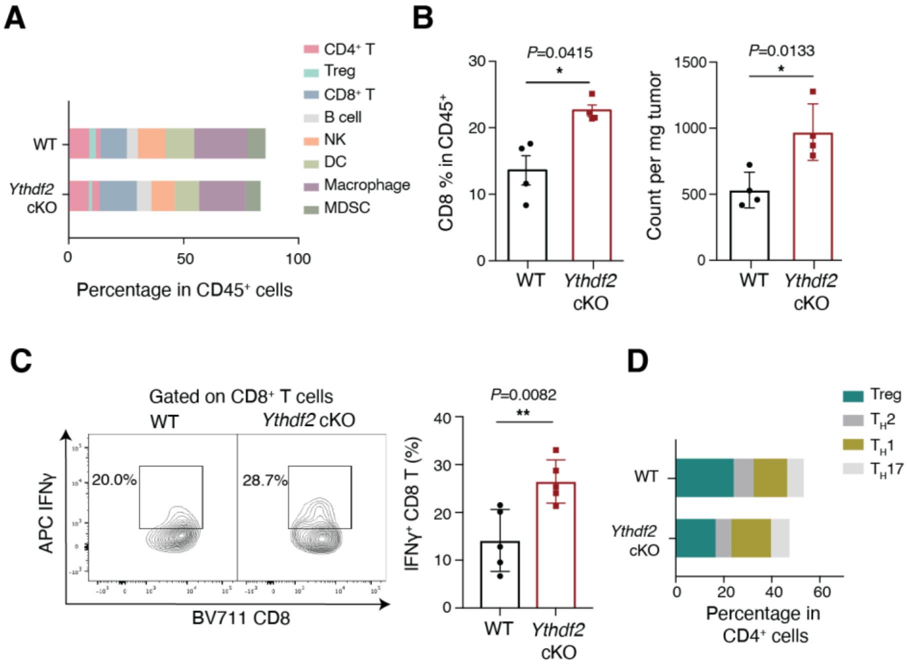

Figure 3.3 ***Ythdf2*****-deficient Treg cells lead to increased infiltration of cytotoxic T cells**

16 days after tumor inoculation, B16F10 tumors from WT and *Ythdf2* cKO mice were digested for flow cytometry analysis. (**A**) Percentage of tumor-infiltrating immune cells in tumors from WT and *Ythdf2* cKO mice. (**B**) Percentage (left) and absolute numbers (right) of CD8$^+$ T cells in tumors. (**C**) Representative plots (left) and the percentage (right) of IFNγ producing CD8$^+$ T cells. (**D**) Percentage of CD4$^+$ subsets.

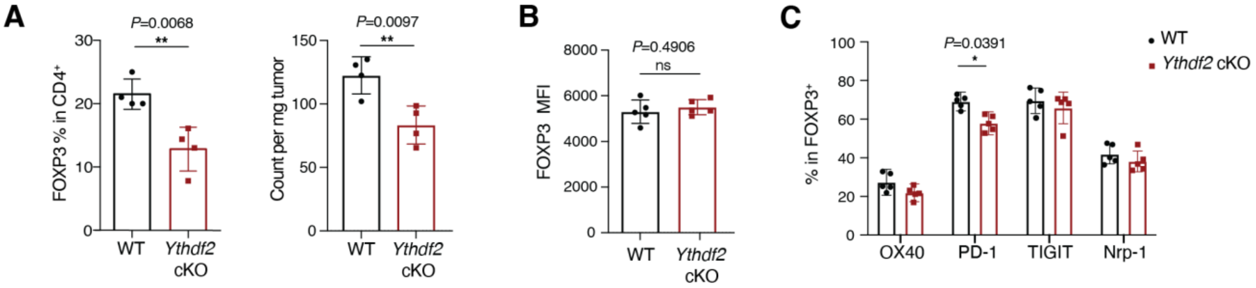

Figure 3.4 ***Ythdf2*****-deficient Treg cells have reduced tumor infiltration**

16 days after tumor inoculation, B16F10 tumors from WT and *Ythdf2* cKO mice were digested for flow cytometry analysis. (**A**) Percentage (left) and absolute numbers (right) of Treg cells. (**B**) FOXP3 expression MFI in tumor-infiltrating Treg cells. (**C**) The proportion of Treg cells expressing the indicated surface marker.

3.2.2 YTHDF2 is dispensible for maintaining peripheral T cell homeostasis

Unlike *Mettl3* or *Mettl14* deficiency in Treg cells that lead to severe autoimmune diseases through modulating m^{6}A modifications[44,47], the lack of m^{6}A reader YTHDF2 in Treg cells did not induce observable skin inflammation. In attempts to capture the chronic effects of *Ythdf2* deletion, we aged WT and *Ythdf2* cKO mice and found that *Ythdf2* cKO mice were able to survive for one year without observable inflammation phenotypes. Specifically, hematoxylin and eosin staining of the tissues collected from adult mice showed no sign of inflammation in the kidney, skin, intestine, liver, and pancreas (Figure 3.5A). Additionally, *Ythdf2* cKO and WT adult mice have comparable body weights (Figure 3.5B).

To examine whether *Ythdf2* KO Treg cells disturb T cell homeostasis, we profiled splenic T cell populations in WT and *Ythdf2* cKO mice. The immune cell profiles remained the same between the two groups of mice, with no hyper-activation of T cells observed in *Ythdf2* cKO mice (Figure 3.5C), suggesting that the peripheral Treg cells are functional even without YTHDF2. WT and *Ythdf2* cKO mice have comparable ratios of Treg cells (Figure 3.5D), and the two Treg populations expressed FOXP3 at a similar level (Figure 3.5E). Key Treg surface markers, including NRP1, CD103, ICOS, CD25, and CD62L, were unaffected by the loss of YTHDF2 (Figure 3.5F-G). Meanwhile, consistent with that on intratumoral Treg cells, PD-1 expression on Treg cells from *Ythdf2* cKO mice was decreased compared to WT mice (Figure 3.5H).

We further examined the suppressive function of *Ythdf2* cKO Treg cells in the periphery. First, we cocultured WT or *Ythdf2* cKO Treg cells with responder T cells *in vitro*. We found that WT and *Ythdf2* cKO Treg cells isolated from the spleen showed no significant difference in their

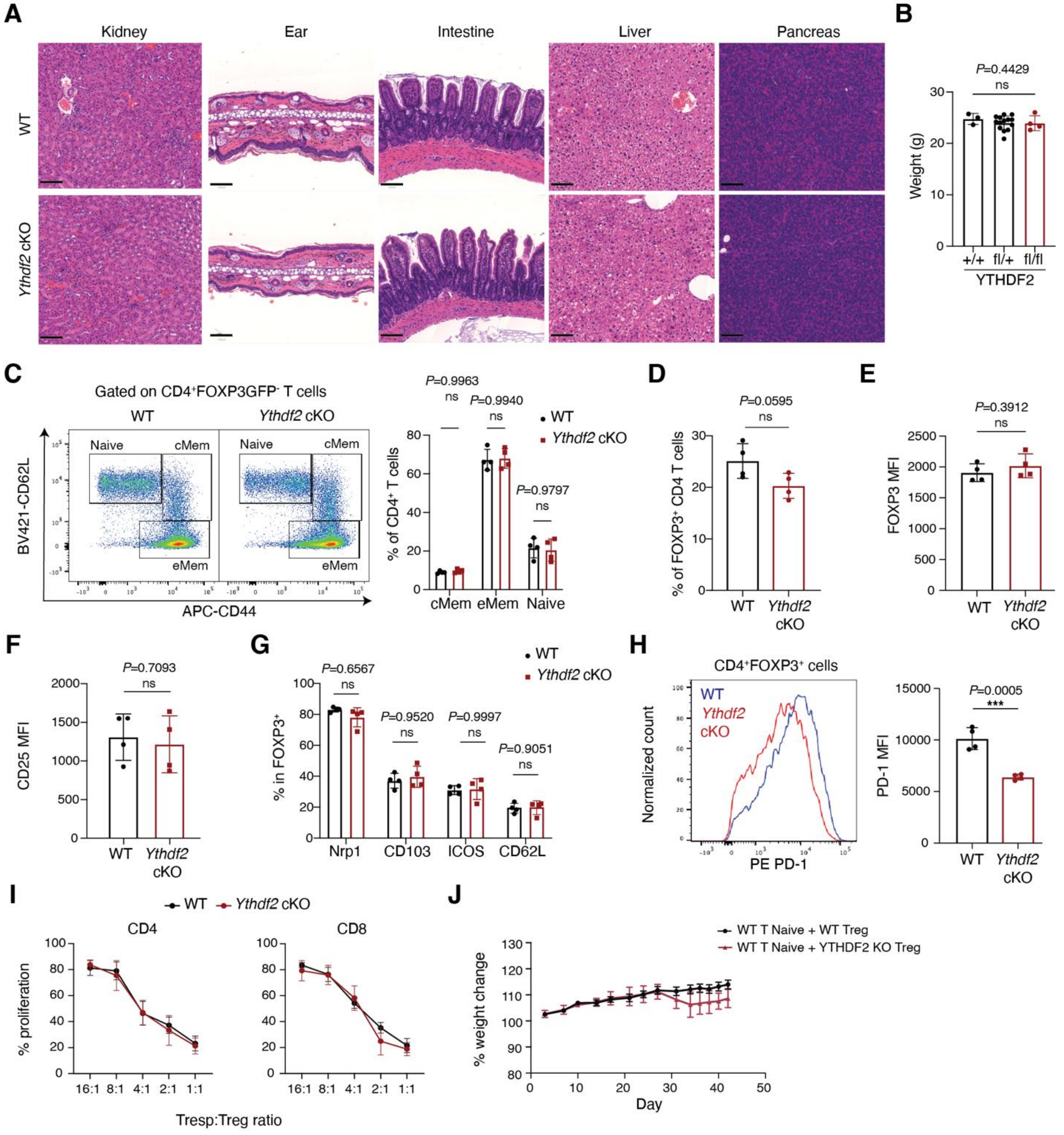

Figure 3.5 YTHDF2 is dispensable for maintaining peripheral T cell homeostasis

(**A**) Representative images of hematoxylin and eosin staining of the indicated tissues from 1-year-old WT and *Ythdf2* cKO mice. Scale bar: 100 µm. (**B**) Body weight of mice at 12 weeks old. Each data point represents one mouse. splenocytes from 1-year-old WT and *Ythdf2* cKO mice were analyzed by flow cytometry. (**C**) Representative plots (left) and the percentage (right) of naïve ($CD62L^{hi}CD44^{lo}$), central memory (cMem, $CD62L^{hi}CD44^{hi}$), and effector memory (eMem, $CD62L^{lo}CD44^{hi}$) T cells. (**D**) percentage (right) of FOXP3 expressing Treg cells in CD4 T cells. (**E**) FOXP3 expression MFI. (**F**) Splenic Treg CD25 MFI values. (**G**) Percentage of FOXP3 Treg

(**Figure 3.5, continued**) cells expressing the indicated surface marker. (**H**) Representative plot (left) of FOXP3 Treg cells PD-1 expression and the MFI value (right) in WT and *Ythdf2* cKO Treg cells. (**I**) Suppression of CellTrace Violet labeled CD4 (left) or CD8 T (right) cells by WT or *Ythdf2* cKO Treg cells at various cell ratios. (**J**) Body weight of Rag$^{-/-}$ mice receiving naïve CD4^{+} T cells with WT or *Ythdf2* cKO Treg cells.

ability to suppress the proliferation of CD4^{+} and CD8^{+} T cells (Figure 3.5I). To further evaluate the peripheral suppressive function *in vivo*, WT or *Ythdf2* cKO Treg cells were co-transferred with naïve T cells into *Rag*$^{-/-}$ mice to induce colitis. Disease onset was monitored by weight change. WT Treg cells could effectively protect recipients from developing colitis, whereas *Ythdf2* cKO Treg cells led to a slight but insignificant weight loss after 40 days (Figure 3.5J). Therefore, while the transplant experiment suggested that *Ythdf2* cKO Treg cells have a mild functional defect, the defect was insufficient to interrupt T cell homeostasis in the host. Our data suggested that loss of YTHDF2 in Treg cells does not abolish T cell homeostasis in the periphery.

3.2.3 YTHDF2 maintains the function and survival of tumor-infiltrating Treg cells

The anti-tumor response in *Ythdf2* cKO mice indicated impaired suppression of Treg cells without sacrificing Treg identity. To evaluate the function of Treg cells, we isolated intratumoral Treg cells from WT and *Ythdf2* cKO mice for *in vitro* coculture with fluorescently labeled CD8^{+} T cells. Compared with those from WT mice, Treg cells isolated from *Ythdf2* cKO mice have compromised suppressive functions, leading to more proliferative responder CD8^{+}T cells (Figure 3.6A) and increased IFNγ production (Figure 3.6B).

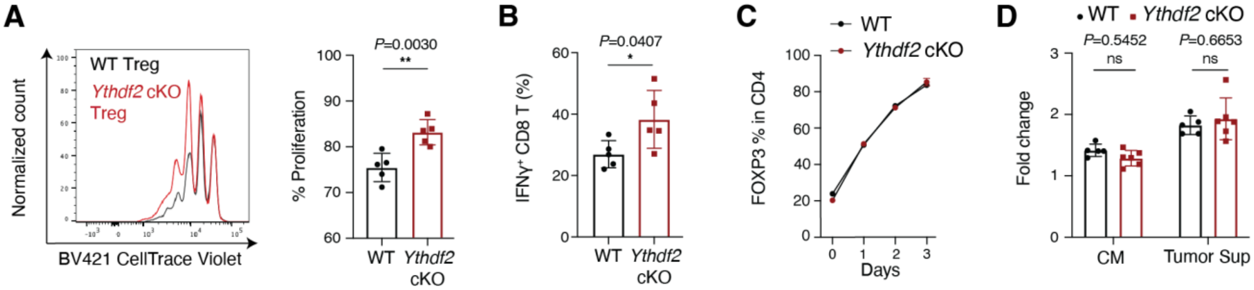

Figure 3.6 *Ythdf2* cKO Treg cells have impaired function in the TME

(**Figure 3.6, continued**) In (**A**) and (**B**), Functional assay with WT or *Ythdf2* cKO Treg cells isolated from B16F10 tumors on day 16. (**A**) Representative proliferation plot (left) of CellTrace Violet labeled $CD8^+$ T cells and the corresponding proliferation percentage normalized to $CD8^+$ T cells cultured without Treg cells (right). (**B**) Percentage of IFNγ producing CD8 T cells after coculture. (**C**) Percentage of FOXP3 expressing Treg cells in $CD4^+$ T cells after induction with retinol acid and TGFβ. (**D**) A transwell assay with splenic isolated Treg cells. Cells were migrated towards control media, B16F10 conditioned culture media (CM), or B16F10 solid tumor supernatant (Tumor Sup). The number of Treg cells migrated to the lower chamber was normalized to that with control media conditions.

Besides the impaired suppression function, reducing intratumoral Treg cell number could also increase the INFγ expressing $CD8^+$ T cells infiltration and anti-tumor immunity[147]. Therefore, we further investigated how *Ythdf2* deletion reduced the tumor infiltration of Treg cells. Treg cells can be recruited to the tumor site or induced and expanded *in situ*. In the TME, Treg cells can be induced from $CD4^+$ T cells with TGFβ[148]. To examine whether YTHDF2 interferes with Treg induction, splenic $CD4^+$ T cells were isolated from both WT and *Ythdf2* cKO mice and cultured with retinol acid and TGFβ. Monitoring the ratio of FOXP3 expressing Treg cells, we found that cells from WT and *Ythdf2* cKO mice were able to generate induced Treg cells at the same rate (Figure 3.6C). Next, the migratory ability of Treg cells was studied in a transwell migration assay. The cultured media collected from B16F10 cell culture (CM) or B16F10 solid tumor supernatant (Tumor Sup) were used to induce Treg migration. Both the CM and solid tumor supernatant were able to enhance Treg migration when compared to control media that was not conditioned with tumor cells. Under these conditions, *Ythdf2* cKO Treg cells were able to migrate to the same extent as WT Treg cells, suggesting that YTHDF2 did not regulate the migratory ability of Treg cells toward tumor sites (Figure 3.6D). Finally, staining with apoptotic marker Annexin V revealed a higher frequency of apoptotic Treg cells in tumors from *Ythdf2* cKO mice than that from WT mice (Figure 3.7A), indicating the reduction of Treg cells in *Ythdf2* cKO mouse tumors was in part due to increased apoptosis. Thus, the lack of YTHDF2 may hinder Treg cell survival and suppressive function in the TME to enhance anti-tumor immunity. Note that, unlike tumor-infiltrating Treg cells, splenic Treg cells did not have increased apoptosis with *Ythdf2* deletion (Figure 3.7B). This result suggested that YTHDF2 regulates Treg cells in the tumor but not in the spleen.

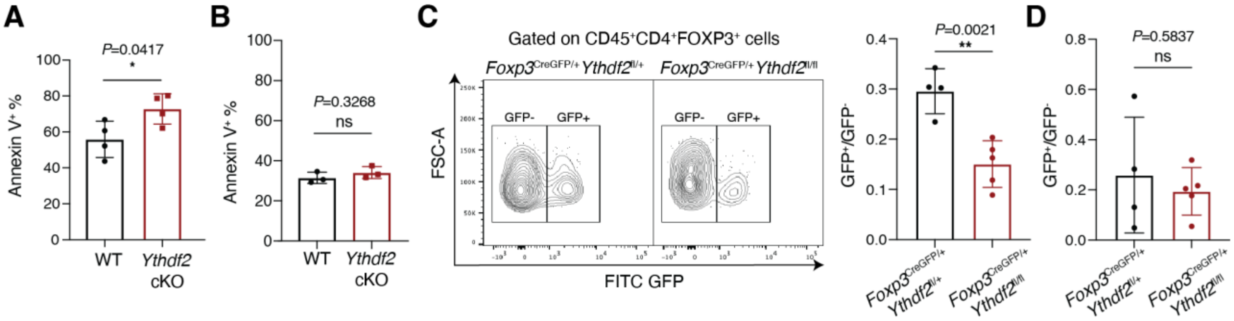

Figure 3.7 *Ythdf2*-deficient Treg cells are more apoptotic in the TME

Ratio of Annexin V$^+$ Treg cells in the B16F10 tumor (**A**) or spleen (**B**). (**C**) Representative plots (left) and ratio (right) of GFP$^+$/GFP$^-$ Treg cells in B16F10 tumors from *Foxp*3$^{\text{CreGFP/+}}$*Ythdf2*$^{\text{fl/+}}$ or *Foxp*3$^{\text{CreGFP/+}}$*Ythdf2*$^{\text{fl/fl}}$ mice. (**D**) GFP$^+$/GFP$^-$ ratio of FoxP3 expressing Treg cells in the spleen from *Foxp*3$^{\text{CreGFP/+}}$*Ythdf2*$^{\text{fl/+}}$ or *Foxp*3$^{\text{CreGFP/+}}$*Ythdf2*$^{\text{fl/fl}}$ mice.

To compare the behavior of WT and *Ythdf2* KO Treg cells in the same context, we generated chimeric (*Foxp*3$^{\text{CreGFP/+}}$) mice, where the *Foxp*3$^{\text{CreGFP/+}}$*Ythdf2*$^{\text{fl/fl}}$ mice would have WT and *Ythdf2* KO Treg cells. When the chimeric mice developed tumors, the GFP$^+$/GFP$^-$ FOXP3 cell ratio was much lower in tumors from *Ythdf2*$^{\text{fl/fl}}$ chimeric mice compared with the control mice, indicating a significant loss of *Ythdf2* KO Treg in the tumor (Figure 3.7C). This comparison supported our finding that YTHDF2 sustains tumor Treg cell infiltration. However, *Ythdf2*$^{\text{fl/+}}$ and *Ythdf2*$^{\text{fl/fl}}$ chimeras showed a similar ratio of GFP$^+$/GFP$^-$ FOXP3 cells in the spleen, indicating that *Ythdf2* deletion does not affect WT and YTHDF2 KO Treg ratio in the spleen (Figure 3.7D). This discrepancy observed in the periphery and tumors suggested that the regulatory mechanism of YTHDF2 in Treg cells is tumor-specific, making YTHDF2 a unique target to achieve tumor-specific Treg regulation with minimized peripheral side effects.

3.2.4 YTHDF2 regulates the NF-κB signaling pathway by destabilizing m^{6}A-modified negative regulator transcripts

To reveal the mechanism of YTHDF2 in regulating Treg cell survival and function in TME, we isolated tumor-infiltrating Treg cells from WT and *Ythdf2* cKO mice bearing B16F10 tumors and performed RNA sequencing, YTHDF2 RNA immunoprecipitation sequencing (RIP-seq), and MeRIP seq. Tumor-infiltrating Treg cells from WT and *Ythdf2* cKO mice were well separated based on gene clustering results (Figure 3.8A). YTHDF2 targets tended to be upregulated in *Ythdf2* cKO Treg cells (Figure 3.8B), which is consistent with the function of YTHDF2 in promoting mRNA decay. Consistent with our findings of the increased apoptotic population in *Ythdf2* cKO Treg cells (Figure 3.7A), KEGG pathway enrichment analysis revealed that the upregulated genes in *Ythdf2* cKO Treg cells were enriched for apoptosis-related genes (Figure 3.8C). Besides, negative regulators of NF-κB were also upregulated in *Ythdf2* cKO Treg cells (Figure 3.8D). The downregulated genes in *Ythdf2* cKO Treg cells were enriched for metabolic pathways and cell cycle (Figure 3.8E). We found transcripts encoding NF-κB pathway negative regulators, including *Nlrc3*, *Nlrc5*, *Nfkbie*, *Traf3*, and *Tnfaip3*[149–153], are targets of YTHDF2 and are m^{6}A methylated in WT Treg cells (Figure 3.8F). Further, previous m^{6}A-CLIP and YTHDF2 CLIP-seq performed in CD4$^+$ T cells revealed these NF-κB negative regulators contained m^{6}A modifications at YTHDF2 binding sites, suggesting binding through direct recognition of m^{6}A modifications (Fig 3.8G)[154]. The NF-κB signaling pathway is known to be important for Treg identity, survival, and function[155,156]. For example, NF-κB subunit c-Rel activates the function of Treg cells in the tumor. Deletion or inhibition of c-Rel leads to tumor inhibition[157]. Activation of NF-κB can protect Treg cells from apoptosis[155,158]. Therefore, we propose that YTHDF2 regulates the NF-κB pathway in Treg cells to maintain the suppressive TME.

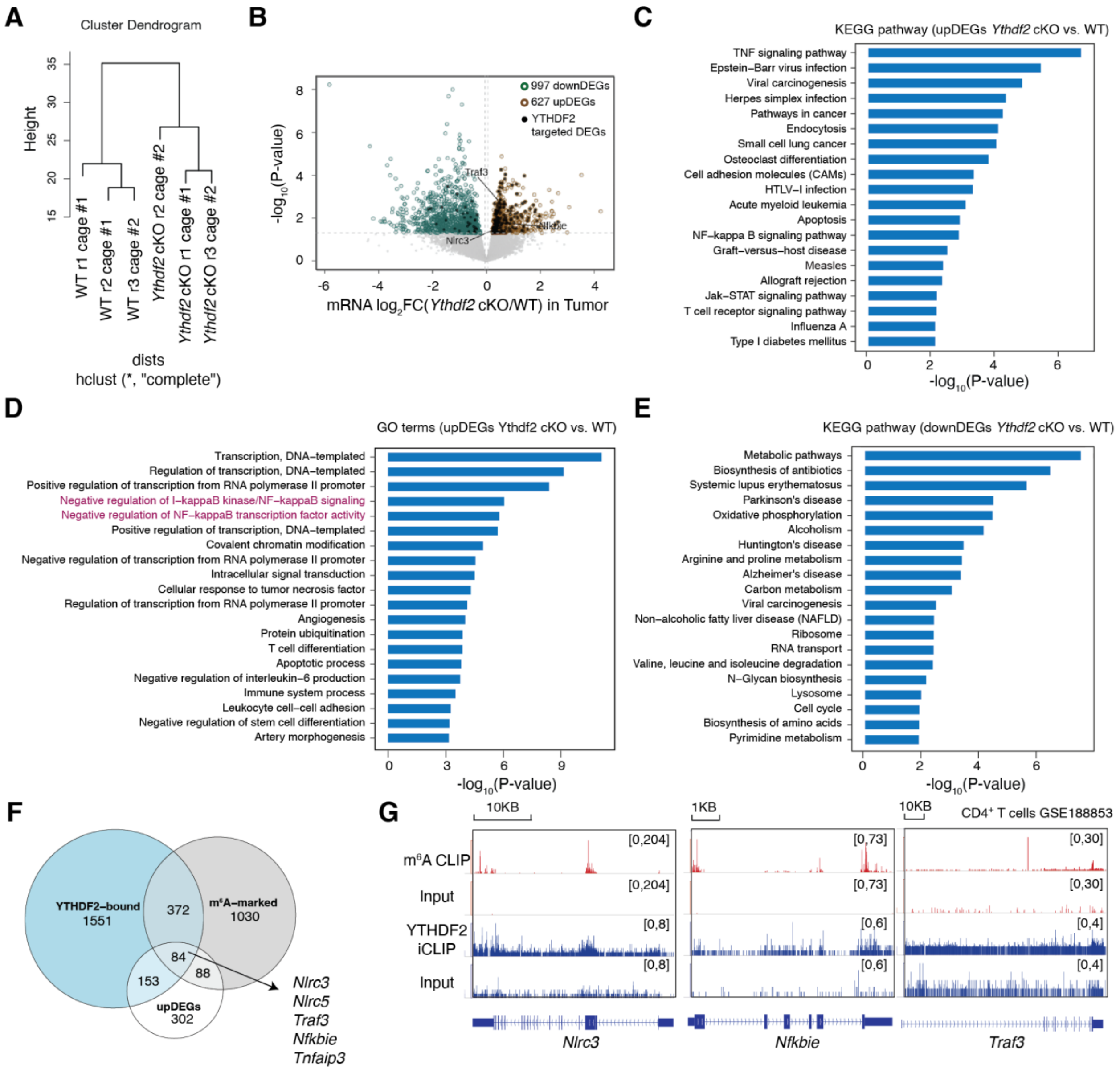

Figure 3.8 YTHDF2 regulates transcripts of NF-κB negative regulators through m^{6}A modifications

(**A**) A dendrogram showing the relationship of gene expression level in WT and *Ythdf2* KO Treg cells in tumor. (**B**) Volcano plot of the differentially expressed genes (DEGs, p-value < 0.05) of *Ythdf2* cKO *vs.* WT Treg cells in tumor comparing *Ythdf2* cKO *vs.* WT Treg cells. The upregulated DEGs were highlighted in yellow and the downregulated DEGs were highlighted in green. YTHDF2 binding targets were denoted by black dots. (**C**) KEGG pathway enrichment analysis of the upregulated genes upon *Ythdf2* KO in Treg cells from tumor site. (**D**) GO enrichment analysis of upregulated genes upon *Ythdf2* cKO in Treg cells from tumor site. (**E**) KEGG pathway enrichment analysis of the downregulated genes in intratumoral Treg cells from *Ythdf2* cKO mice. (**F**) Venn diagram showing the overlap between upregulated genes upon *Ythdf2* cKO in Treg cells with transcripts that are m^{6}A modified and bound by YTHDF2 in WT Treg cells. (**G**) IGV

(**Figure 3.8, continued**) showing m^{6}A and YTHDF2 binding at *Nlrc3*, *Nfkbie*, and *Traf3* loci in CD4$^+$ T cells (GSE188853).

NF-κB signaling is activated via T cell receptor (TCR) signaling or tumor necrosis factor receptor superfamily (TNFR) signaling[159]. We analyzed the publicly available RNA sequencing data of TCR and TNFR2 antagonist-stimulated Treg cells[160]. A comparison of gene expression profile in WT and *Ythdf2* KO Treg cells *versus* that in TCR- and TNFR2-stimulated Treg cells showed *Ythdf2* deletion functions oppositely to TCR/TNFR2 signaling (Figure 3.9A), suggesting *Ythdf2* cKO Treg cells failed to activate the downstream NF-κB signaling pathway. Further, depletion of TNFα, which activates NF-κB through TNFR signaling, eliminated the difference in tumor growth in WT and *Ythdf2* cKO mice (Figure 3.9B). Anti-TNFα treatment partially rescued the Treg cell infiltration (Figure 3.9C) and apoptosis (Figure 3.9D) in *Ythdf2* cKO mice. This indicates that the tumor suppressive effect of *Ythdf2* cKO mice was partly driven by TNFα in the TME.

To understand how YTHDF2 regulated NF-κB signaling, we treated WT and *Ythdf2* KO Treg cells with TNFα. The levels of *Nlrc3*, *Nfkbie*, and *Traf3* were upregulated 24 hours post TNFα stimulation in *Ythdf2* KO Treg cells, while *Nlrc5* and *Tnfaip3* levels remained unchanged (Figure 3.10A). Notably, the difference was not observed without TNFα stimulations (Figure 3.10A). We then followed the dynamics of *Nlrc3*, *Nfkbie*, and *Traf3* at different time points upon TNFα stimulation and observed an oscillation of these genes in WT Treg cells (Figure 3.10B). However, the loss of YTHDF2 in Treg cells led to weakened oscillation, resulting in significantly higher expression levels of these transcripts at 24 hours post TNFα stimulation (Figure 3.10B). Therefore, YTHDF2 exhibits a notable regulatory function when NF-κB signaling is activated by TNFα in Treg cells.

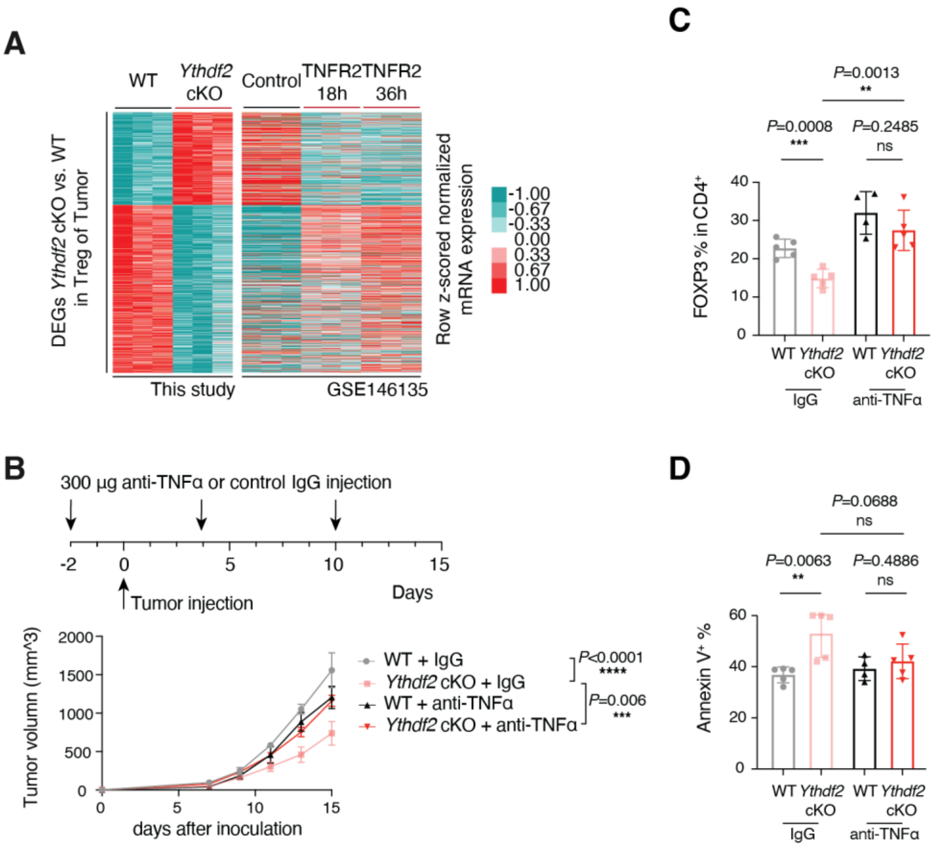

Figure 3.9 Elevated TNFα signaling in the TME induces *Ythdf2* cKO Treg apoptosis

(**A**) Heatmap showing gene expression in WT and *Ythdf2* cKO Treg cells (left panel), and in Treg cells that were activated with anti-CD3/CD28 mAbs with TNFR2 agonists for 18 or 36 hours (right panels, GSE146135). Rows are the differentially expressed genes (DEGs, p-value < 0.05) of *Ythdf2* cKO *vs.* WT Treg cells in the tumor. In (**B**), (**C**), and (**D**), B16F10 tumors were developed in mice receiving anti-TNFα or control IgG treatments and harvested on day 15 after tumor injection (**B**) Schematic representation of the anti-TNFα treatments (top). Tumor growth of B16F10 in WT and *Ythdf2* cKO mice receiving anti-TNFα treatments (bottom). (**C**) Ratio of tumor-infiltrating Treg cells in $CD4^+$ T cells. (**D**) Percentage of apoptotic Treg cells in the tumor.

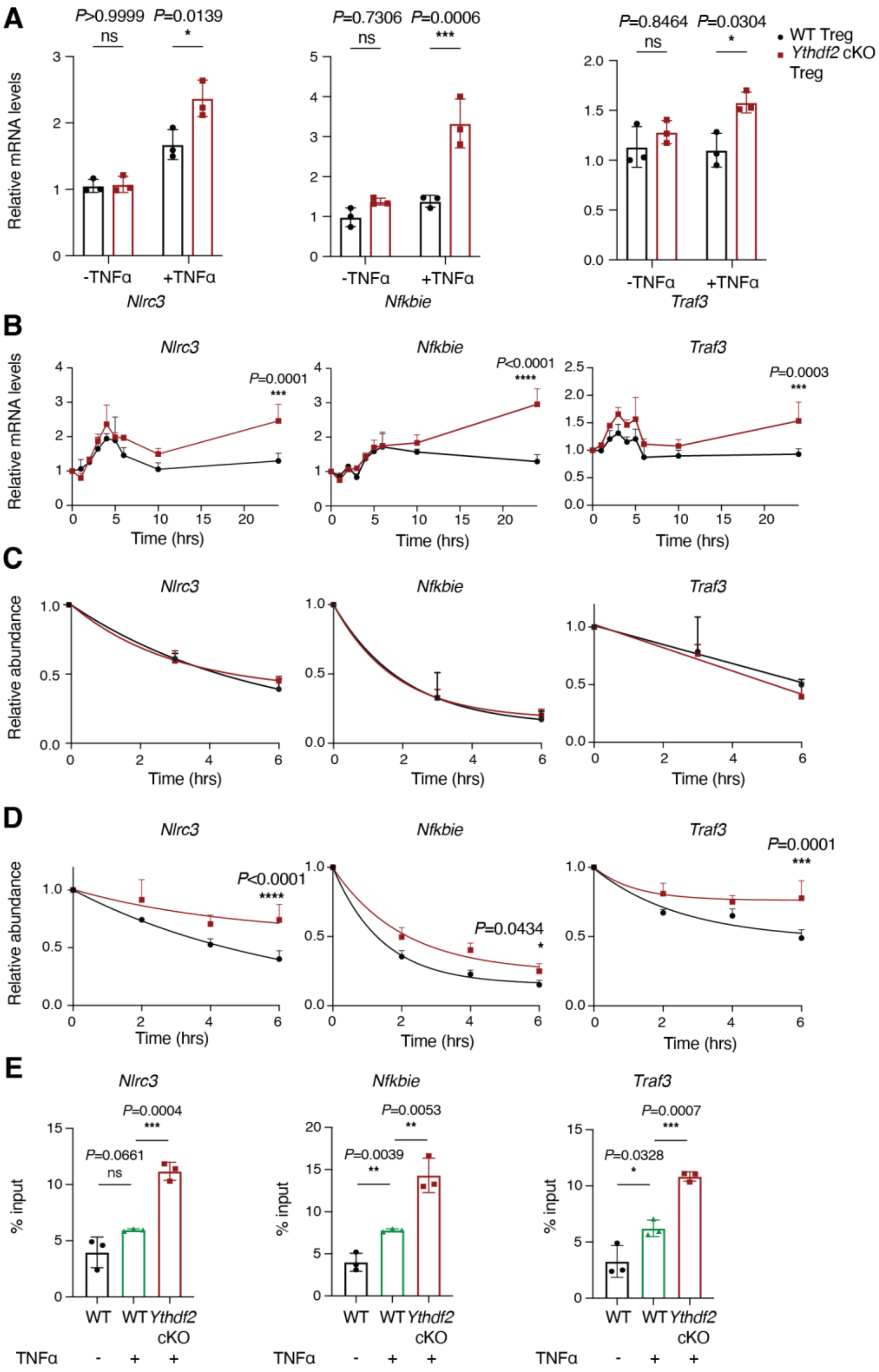

Figure 3.10 YTHDF2 regulates the decay of *Nlrc3, Nfkbie*, and *Traf3* after TNFα stimulation

WT or *Ythdf2* cKO Treg cells were isolated from the corresponding mice for in vitro treatments with 10 ng/mL TNFα for 24 hours. (**A**) Relative mRNA levels of indicated genes in WT or *Ythdf2*

(**Figure 3.10, continued**) cKO Treg cells before or after 24 hours TNFα stimulation. (**B**) Changes in *Nlrc3*, *Nfkbie*, and *Traf3* over time after TNFα stimulation. (**C**) and (**D**) WT or *Ythdf2* cKO Treg cells were treated with Actinomycin D with (**D**) or without (**C**) TNFα stimulation. Decay of *Nlrc3*, *Nfkbie*, and *Traf3* was monitored by. (**E**) Total RNA from stimulated or unstimulated cells were subjected to m^6A-IP and quantified by RT-qPCR.

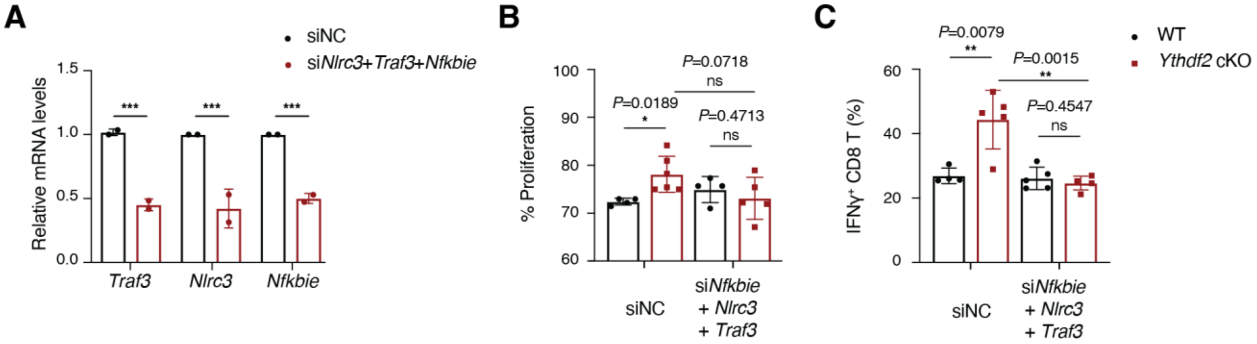

Figure 3.11 Knockdown of NF-κB negative regulators in *Ythdf2* cKO Treg cells rescues their suppressive function

(**A**) Knockdown efficiency of indicated genes in Treg cells. In (**B**) and (**C**), tumor-infiltrating Treg cells were sorted from B16F10 tumors on day 16. After knockdown, responder cells were cocultured for 3 days. (**B**) Proliferation of $CD8^+$ T cells. (**C**) Percentage of IFNγ producing $CD8^+$ T cells after coculture.

We next investigated whether the regulatory role of YTHDF2 in Treg cells derives from its known function in promoting mRNA decay. WT and *Ythdf2* cKO Treg cells were cultured *in vitro* and treated with Actinomycin D (ActD) to inhibit transcription. Cells were collected at various time points to follow the decay of YTHDF2 target transcripts, *Nlrc3*, *Nfkbie*, and *Traf3*. Without TNFα stimulation, the stability of these transcripts was not affected by YTHDF2 knockout (Figure 3.10C). However, 24 hours post TNFα stimulation, all three transcripts showed increased stability in *Ythdf2* cKO Treg cells (Figure 3.10D). Therefore, YTHDF2 is activated to decay transcripts that encode NF-κB negative regulators *Nlrc3*, *Nfkbie*, and *Traf3* in a manner specific to TNFα stimulation. TNFα stimulation also led to an increase in the ratio of the m^6A modification on *Nlrc3*, *Nfkbie*, and *Traf3* transcripts, and the portion of m^6A-modified transcripts was further accumulated in *Ythdf2* cKO Treg cells (Figure 3.10E). Furthermore, we performed *in* *vitro* knockdown of YTHDF2 targets in intratumoral Treg cells sorted from WT and *Ythdf2* cKO mice (Figure 3.11A). Knockdown of *Nlrc3*, *Nfkbie*, and *Traf3* could rescue the suppression function of *Ythdf2* cKO Treg cells, indicated by the reduced proliferation of CD8$^+$ T cells (Figure 3.11B) and IFNγ secretion (Figure 3.11C).

3.2.5 The regulation by YTHDF2 in Treg cells is induced via elevated TNFα-NF-κB signaling pathway in TME

YTHDF2 has been demonstrated to exert context-dependent functions in various systems by regulating the stability of m^{6}A-modified transcripts[161–163]. To investigate how TNFα signaling activates the function of YTHDF2 in NF-κB regulation, we followed *Ythdf2* expression after TNFα stimulation. TCR and TNFR2 signaling heavily induced *Ythdf2* mRNA expression while suppressing *Ythdf3* and *Ythdc1* expression. (Figure 3.12A)[160]. Consistently, Treg cells with TCR stimulation showed an increased binding at the *Ythdf2* promotor region by NF-κB subunit p65 (Figure 3.12B)[156], revealing that NF-kB is activated and translocated to the nucleus to promote transcription of *Ythdf2*. Next, we stimulated Treg cells with TNFα and found that, in agreement with published RNA-seq data (Figure 3.12A), long-term TNFα stimulation could elevate the protein level of YTHDF2 (Figure 3.12C). Monitoring *Ythdf2* mRNA level revealed that the expression level quickly oscillated after stimulation (Figure 3.12D). Simultaneously, the mRNA level of *Tnfaip3* also oscillated as previously reported following NF-κB signaling (Figure 3.12E)[164]. The NF-κB signaling pathway is known to have negative feedback regulation and the expression level of genes in the signaling pathway oscillates after stimulation to tune NF-κB activity[153,165]. The changes in the *Ythdf2* expression level indicate that YTHDF2 is activated by NF-κB signaling and becomes a part of the feedback signaling loop.

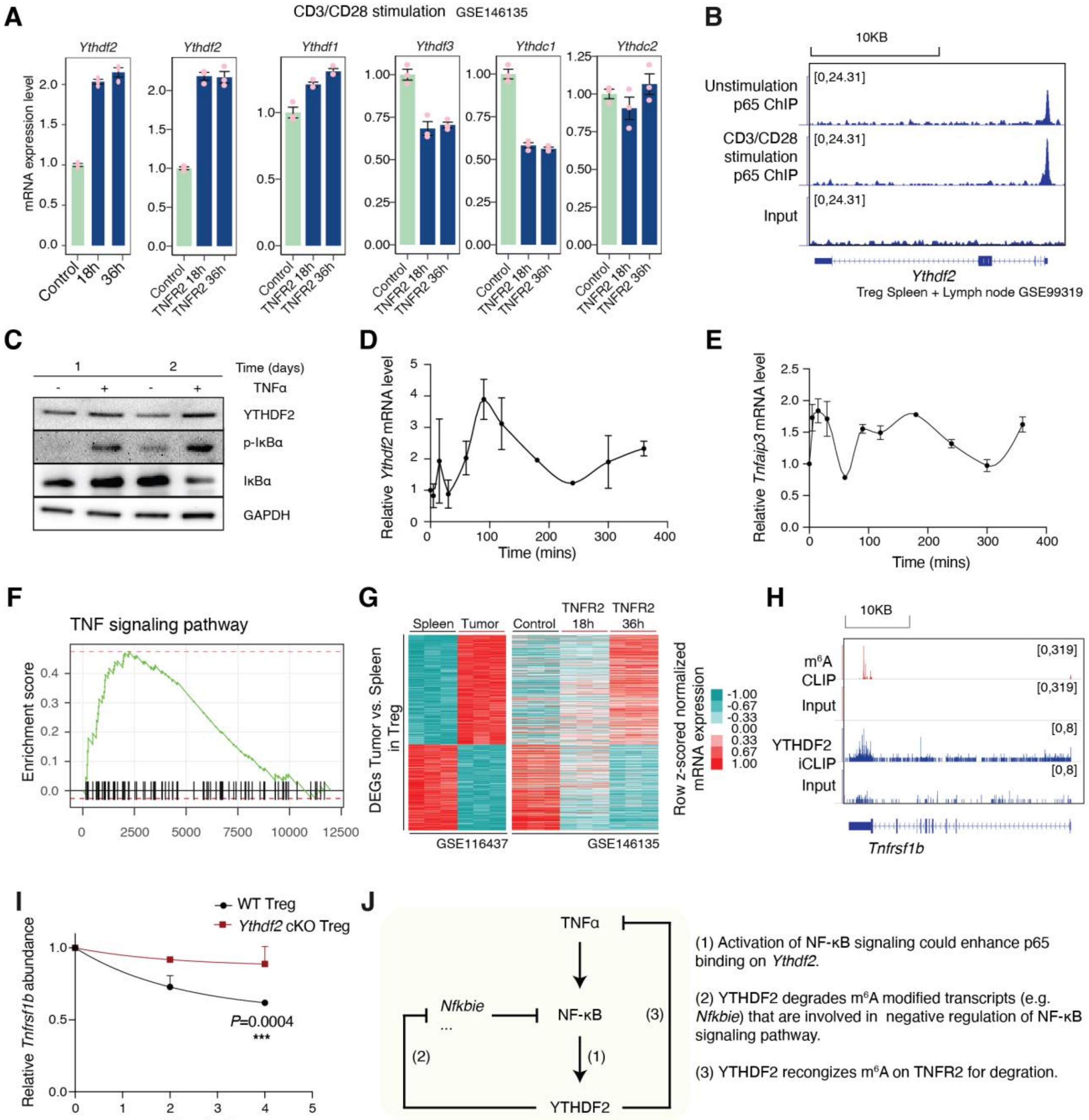

(1) Activation of NF-κB signaling could enhance p65 binding on *Ythdf2*.

(2) YTHDF2 degrades m⁶A modified transcripts (e.g. *Nfkbie*) that are involved in negative regulation of NF-κB signaling pathway.

(3) YTHDF2 recongizes m⁶A on TNFR2 for degration.

Figure 3.12 Activation of NF-κB signaling induces *Ythdf2* expression

(**A**) Bar plot showing *Ythdf2*, *Ythdf1*, *Ythdf3*, *Ythdc1*, and *Ythdc2* expression levels in WT Treg cells that were activated with anti-CD3/CD28 mAbs and agonists of TNFR2 for 18 or 36 hours (GSE146135). (**B**) IGV visualization showing p65 binding at *Ythdf2* genomic loci in CD3/CD28 stimulated and unstimulated Treg cells (GSE99319). In (**C**)-(**E**), WT Treg cells from the spleen were stimulated with 10 ng/mL TNFα *in vitro*. (**C**) YTHDF2, IκBα, and p-IκBα expression level with or without TNFα stimulation for the indicated duration. Changes in *Ythdf2* (**D**) or *Tnfaip3* (**E**) mRNA expression level over time after TNFα stimulation. (**F**) GSEA enrichment analysis was performed with genes in TNF signaling pathway as gene list and expression $\log_2$FC comparing

(**Figure 3.12, continued**) Treg cells from tumor *versus* that from spleen as rank list. (**G**) Heatmap showing gene expression profile in Treg cells from Spleen and Tumor (left panel, GSE116437), and in Treg cells that were activated with anti-CD3/CD28 mAbs and TNFR2 agonists for 18 or 36 hours (right panels, GSE146135). Rows are the differentially expressed genes (DEGs, p-value $<$ 0.05) comparing Treg cells from tumor with that from spleen. (**H**) IGV visualization showing m^6A modification and YTHDF2 binding at *Tnfrs1b* loci in CD3/CD28 stimulated and unstimulated Treg cells (GSE99319). (**I**) WT or *Ythdf2* cKO Treg cells were treated with Actinomycin D after TNFα stimulation, and the decay of *Tnfrsf1b* was followed. (**J**) A schematic model showing the feedback regulation of YTHDF2 and TNFα-NF-κB signaling pathway.

Treg cells are known to have elevated TNF signaling after entering the tumor site (Figure 2.12F)[136]. Meanwhile, the DEGs profile revealed from RNA-seq in tumor-infiltrating Treg cells correlates with TCR and TNFR2 antagonist-stimulated Treg cells, strongly suggesting Treg cells have activated TNF signaling in the tumor (Figure 2.12G)[136,160]. In the TME, elevated TNF-NF-κB signaling in Treg cells activates and amplifies the regulatory functions of YTHDF2. In contrast, Treg cells in healthy tissues have a basal level of TNF-NF-κB signaling, negating the need for YTHDF2 in maintaining peripheral homeostasis. This difference in TNF signaling could explain the TME-specific function of YTHDF2 in regulating Treg survival and functions.

These results led us to propose that NF-κB signaling in intratumoral Treg cells is regulated by YTHDF2 (Figure 3.13). In WT Treg cells, TNF signaling releases NF-κB to the nucleus and activates *Ythdf2* expression along with other negative regulators to initiate the feedback signaling. Cytoplasmic YTHDF2 accelerates the degradation of transcripts encoding NF-κB negative regulators to sustain prolonged NF-κB signaling. *Ythdf2* deficient Treg cells accumulate NF-κB negative regulators over time and interrupt NF-κB signaling. Blockage of NF-κB signaling leads to impaired Treg function, increased apoptosis, and enhanced anti-tumor immune response in the tumor.

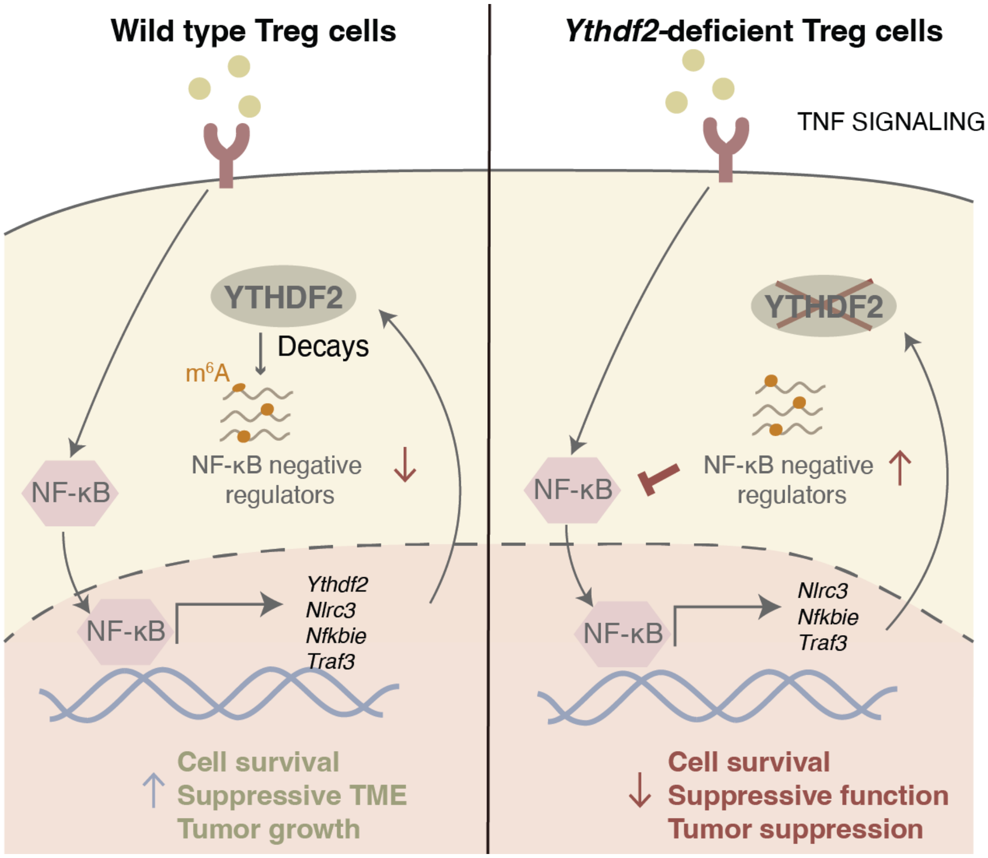

Figure 3.13 Proposed model of YTHDF2 regulation of TNFα-NF-κB signaling in intratumoral Treg cells

We propose that in the TME, elevated TNF signaling activates the downstream NF-κB signaling, which promotes the transcription of its negative regulators and YTHDF2. The transcripts for NF-kB negative regulators are methylated and regulated by YTHDF2 to sustain NF-κB signaling.

3.3 Discussion and conclusion

The immune system is highly regulated to maintain a balance between cytotoxicity and self-tolerance. While activation of the immune system can benefit cancer cytotoxicity, over-activation of the immune system could also result in autoimmune reactions such as inflammation and colitis. A target that could specifically activate the immune system at the tumor site can alleviate the risks of immunotherapy.

The reversible m^6A modification provides dynamic regulation of the transcriptome in different cellular environments. Previous studies revealed the role of m^6A writers in maintaining

Treg function[44,47]. However, the severe autoimmunity caused by deleting *Mettl3*/*Mettl14* renders them suboptimal targets; *Mettl3*/*Mettl14* depletion also blocks naïve T cell maturation and survival[38]. We report that the deletion of *Ythdf2* in Treg cells hinders tumor growth in mice by reducing Treg cell infiltration and altering the suppressive environment. Yet, deletion of *Ythdf2* in Treg cells only leads to mild and insignificant defects in the periphery. *Ythdf2* deletion in Treg cells leads to an increased expression level of YTHDF1 (Figure 3.1C). It is possible that YTHDF1 and other proteins in the m^6A pathway played a role in maintaining peripheral Treg cell functions. Further studies using mice models that deplete multiple YTH proteins simultaneously might reveal the competitive or compensatory effects between YTH proteins. In the TME, Treg cells have elevated signaling through TNF receptors, which activates the downstream NF-κB signaling pathway and the transcription of *Ythdf2*. In human Treg cells, activation of NF-κB signaling can protect cells from apoptosis[155,158]. YTHDF2 becomes a regulator of the NF-κB signaling pathway to sustain Treg cell survival and function in the tumor. Dysregulation of NF-κB signaling in *Ythdf2*-deficient Treg leads to increased cell death and decreased infiltration, thus lessening the suppressive TME. The ability of *Ythdf2*-deficient Treg cells to maintain peripheral homeostasis demonstrates that targeting YTHDF2 could benefit tumor immune response while minimizing the effects of disturbing peripheral homeostasis. Further, comparing WT and $CD4^{Cre}$*Ythdf2*$^{fl/fl}$ mice, we found that deletion of *Ythdf2* in T cells does not affect $CD4^+$ and $CD8^+$ T cell maturation in the thymus (Figure 3.14A). Homeostasis, activation, and apoptosis of $CD4^+$ T cells were also unaffected by *Ythdf2* deletion. (Figure 3.14B-E). Therefore, targeting YTHDF2 does not seem to affect the generation of T cells. Whether YTHDF2 affects the function of $CD4^+$ and $CD8^+$ T cells needs to be investigated. *Ythdf2*-deficient Treg cells showed lower PD-1 expression levels in the periphery and TME (Figure 3.4C and 3.5H). The relevance of PD-1 expression on Treg cells has not been fully elucidated, and further investigations may reveal the combinatory effects of inhibiting YTHDF2 with anti-PD-1/PD-L1 treatments.

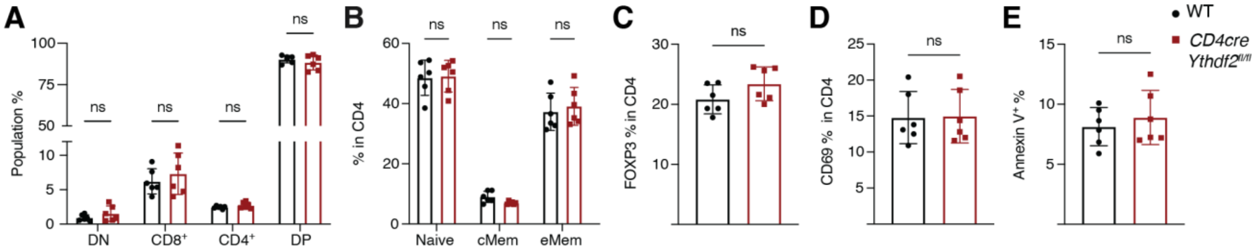

Figure 3.14 YTHDF2 is dispensable for CD4$^+$ T cell development and homeostasis

CD4$^{\text{Cre}}$*Ythdf2*$^{\text{fl/fl}}$ mice and littermate controls (WT) were analyzed by flow cytometry. (**A**) Frequency of the double negative (DN), double positive (DP), and CD4 and CD8 single positive populations in the thymus. In (**B**)-(**E**), Splenocytes from WT or CD4$^{\text{Cre}}$*Ythdf2*$^{\text{fl/fl}}$ mice were analyzed by flow cytometry. (**B**) Frequency of naïve and memory CD4$^+$ T cells. (**C**) Percentage of FOXP3$^+$ Treg in CD4$^+$ T cells. (**D**) Percentage of CD69 expressing CD4$^+$ T cells. (**E**) Ratio of Annexin V$^+$ CD4$^+$ T cells.

The m^{6}A pathway is highly dynamic and can change due to environmental stimulations. NF-κB signaling changed the mRNA expression level of other YTH reader proteins and m^{6}A abundance (Figure 3.10E and 3.12A). Here, we revealed the regulation of the TNF-NF-κB signaling pathway by YTHDF2. While NF-κB negative regulators were upregulated in intratumoral *Ythdf2* cKO Treg cells, we also observed upregulation of TNF signaling (Figure 3.8C). We discovered that YTHDF2 also binds the TNF receptor encoding transcript *Tnfrsf1b* through m^{6}A in T cells (Figure 3.12H)[154]. With TNFα stimulation, deletion of *Ythdf2* stabilized *Tnfrsf1b* in Treg cells (Figure 3.12I). In addition to regulating the inhibitors of NF-κB signaling, YTHDF2 might also regulate the expression level of TNF receptor to fine-tune the downstream NF-κB signaling. Taken together, The YTHDF2-NF-κB axis has a three-fold regulation: i) TNF-NF-κB signaling activates *Ythdf2*; ii) YTHDF2 tunes NF-κB signaling by destabilizing transcripts encoding NF-κB negative regulators; and iii) YTHDF2 tunes TNF signaling by modulating *Tnfrsf1b* expression level (Figure 3.12J).

In conclusion, we presented that YTHDF2 is crucial for Treg cells in the TME through regulating m^{6}A-modified NF-κB negative regulator transcripts (Figure 3.13). Our study suggests YTHDF2 can be a potential drug target for cancer immunotherapy with limited inflammation. YTHDF2 has also been shown to regulate the NF-κB signaling pathway in macrophages[142]. A similar mechanism may regulate other tumor-infiltrating immune cells' function and survival, thus affecting tumor immune surveillance and immune response. Further studies of the m^{6}A methylation patterns in the TME could reveal how tumors stimulate methylation changes to manipulate immune cells. Further, in many tumor cells such as glioma and AML, YTHDF2 has been shown to act as an oncogene[163,166–172]. Therefore, targeting YTHDF2 could have synergistic effects by directly inhibiting tumor cell growth and promoting anti-tumor immunity.

3.4 Methods

3.4.1 Mice

Ythdf2$^{fl/fl}$ mice were generated as previously reported(Li *et al*, 2018). Genotyping PCR primers in EV1A are listed below. C57BL/6/J, CD45.1, Foxp3-CreGFP, and *Rag1*$^{-/-}$ mice were purchased from the Jackson Laboratory. Animals were housed in specific pathogen-free facilities at the University of Chicago with controlled air humidity, temperature, and light cycle. Mice were used at 8-16 weeks unless otherwise stated. All experiments were approved by the University of Chicago Institutional Animal Care and Use Committee. Experiments were performed following the guidelines.

Table 2: *Ythdf2*$^{fl/fl}$ mice genotyping PCR primers

mYthdf2_2F	AGACATCATCTCCACTAGACCTG
mYthdf2_2R	CACACCACCACTTCAATTATCCT
mYthdf2_3F	GAACGGTATTGTCGGTATTGTCA
mYthdf2_3R	AGACCACTCCAACACAGAACTT

3.4.2 Cell culture

The B16F10 (ATCC, CRL-6475, RRID:CVCL_0159) and MC38 (RRID: CVCL_B288) cell lines were cultured in Dulbecco's modified Eagle's medium supplemented with 10% FBS and 1% penicillin-streptomycin. Cells were tested for pathogen contamination. T cells were cultured in RPMI 1640 medium supplemented with 10% heat-inactivated FBS, 2 mM L-glutamine, 50 μM β-mercaptoethanol, and 1% penicillin-streptomycin.

3.4.3 Tumor engraftment

B16F10 or MC38 tumor cells were collected at 50-80% confluency. Cells were washed with DPBS. 2-3×10^5 tumor cells in 100 μL DPBS were injected subcutaneously into the flank. Tumors were measured every 2-3 days by a caliper. Tumor volumes were calculated by Volume = (length×width^2)/2. For anti-TNFα treatments, mice were randomized. Mice received 3 doses of 300 μg anti-TNFα treatments through IP injections. No blinding was done for treatments.

3.4.4 Tissue digestion and cell isolation

Tumors were harvested and minced into small pieces. Tumor tissue was submerged in RPMI with 10 U/mL DNase I (Thermo Fisher Scientific, EN0521) and 1 mg/ml collagenase IV (Gibco, 17104019) and digested at 37 °C for 1 hour. The suspension was filtered through a 70-μm cell strainer. Red blood cells were lysed with ACK Lysing Buffer (Gibco, A1049201) and resuspended in FACS buffer (DPBS with 2% FBS). To obtain splenocytes, the spleen was harvested and mashed using frosted microscope slides. Red blood cells were lysed with ACK Lysing Buffer. Splenocytes were resuspended in FACS buffer and filtered through a 70-μm cell strainer.

3.4.5 Flow cytometry and cell sorting

Cells were stained with antibodies for surface antigens in FACS buffer. To measure cytokine production, cells were resuspended in T cell culture media with 10 ng/mL PMA (Sigma-Aldrich, P8139), 1 μg/mL ionomycin (Sigma-Aldrich, I9657), and 1 μM Monensin (BioLegend, 420701) and incubated at 37 °C for 5 hours. Intracellular cytokines were stained with BD Cytofix/Cytoperm Fixation and permeabilization kit (BD Biosciences, 554714). For FoxP3 staining, Foxp3/Transcription Factor Fixation/Permeabilization Concentrate and Diluent (Thermo Fisher Scientific, 00-5521-00) was used according to the manufacturer's protocol. To retain GFP signal while staining for FOXP3, cells were first pre-fixed with 1% PFA in DPBS at room temperature for 5 minutes. Before cell sorting, splenic CD4$^+$ T cells were enriched by EasySep Mouse CD4$^+$ T cell Isolation Kit (Stemcell, 19852), and tumor-infiltrating lymphocytes were enriched by CD4 (TIL) Microbeads (Miltenyi Biotec, 130-116-475). Data were collected with BD LSR II or Fortessa, and cell sorting was done by BD FACSAria sorters. Flow cytometric data were analyzed by FlowJo software (BD Biosciences). Antibodies used for staining are listed below.

Table 3: Antibodies used for flow cytometry staining

		clone	Catalog	manufacturer	application	dilution
PE	Foxp3	fjk-16s	48-5773-82	eBioscience	FC	1:200
APC	CD45	30-F11	103112	BioLegend	FC	1:200
PE	CD45	30-F11	103106	BioLegend	FC	1:200
Pacific Blue	CD45	30-F11	103216	BioLegend	FC	1:200
PE/cy7	CD8	53-6.7	100722	BioLegend	FC	1:200
APC	CD8	SK1	344721	BioLegend	FC	1:200
BV711	CD8	53-6.7	100747	BioLegend	FC	1:200
BV711	CD4	RM4-5	100557	BioLegend	FC	1:200
APC	CD4	RM4-5	100516	Biolegend	FC	1:200
PE	CD4	RM4-5	100511	BioLegend	FC	1:200
APC/Cy7	CD4	GK1.5	100414	BioLegend	FC	1:200
APC	IFNg	XMG1.2	505810	BioLegend	FC	1:200
	Zombie Red		423109	BioLegend	FC	1:1000
PE	CXCR3	CXCR3-173	126505	BioLegend	FC	1:200
PE/cy7	CCR4	2G12	131213	BioLegend	FC	1:200

(**Table 3, continued**)

APC	CCR6	29-2L17	129814	BioLegend	FC	1:200
BV421	CD19	6D5	115538	BioLegend	FC	1:200
PE/Cy7	NK1.1	S17016D	156513	BioLegend	FC	1:200
BV711	CD3	17A2	100241	BioLegend	FC	1:200
PE	Gr-1	RB6-8C5	108408	BioLegend	FC	1:200
APC/Cy7	CD11b	M1/70	101226	BioLegend	FC	1:200
PE/Cy7	F4/80	BM8	1233113	BioLegend	FC	1:200
APC	CD11c	N418	117310	BioLegend	FC	1:200
BV711	OX40	0X-86	119421	BioLegend	FC	1:200
BV421	TIGIT	1G9	142111	BioLegend	FC	1:200
PE	NRP1	3.00E+12	145203	BioLegend	FC	1:200
APC	CD44	IM7	103011	Biolegend	FC	1:200
BV421	CD62L	MEL-14	104436	Biolegend	FC	1:200
PE	CD103	2.00E+07	121405	Biolegend	FC	1:200
PE	ICOS	7E.17G9	12-9942-82	eBioscience	FC	1:200
APC	CD45.1	A20	110714	Biolegend	FC	1:200
PE	CD25	PC61	102008	BioLegend	FC	1:200
PE/cy7	CD69	H1.2F3	104511	BioLegend	FC	1:200
PE	PD1	29F.1A12	135206	BioLegend	FC	1:200
Pacific Blue	Annexin V		640918	BioLegend	FC	1:20
	7AAD		420403	BioLegend	FC	1:20
	YTHDF2		ab220163	Abcam	FC	1:1000

3.4.6 *Ex vivo* suppression assay

Responder CD4$^+$ or CD8$^+$ T cells were enriched from CD45.1 mice splenocytes by EasySep Mouse CD4$^+$ or CD8$^+$ T cell Isolation Kit (Stemcell, 19853) and stained with CellTrace Violet (Thermo Fisher Scientific, C34571). Mouse T-Activator CD3/CD28 Dynabeads (Gibco, 11452D) were added to T cells at a 1:1 ratio. GFP$^+$ Treg cells were sorted from CD4$^+$ T enriched splenocytes or tumor suspension. Responder and Treg cells were seeded at various ratios in T cell culture media for 3 days. Cultured cells were stained with CD45.1 and proliferation was tracked by the CellTrace Violet signal of the CD45.1$^+$ population. To knockdown transcripts in Treg cells, 5,000 cells were sorted into 50 μL of culture media. A final concentration of 25 nM siRNA

(Thermo Fisher Scientific, siNC: 4390843, si*Nfkbie*: s70554, si*Nlrc3*: 114125, si*Traf3*: s75427) and 0.45 µL of TransIT-TKO® Transfection Reagent (Mirus, MIR2154) were resuspended in 9 µL Opti-MEM and added to cells. 6 hours after knockdown, responder cells were added and cultured as described above.

3.4.7 *In vitro* Treg induction

Treg cells were induced from CD4$^+$ T cells following the previously reported protocol[173]. Splenocytes CD4$^+$ T cells were resuspended in T cell culture medium at 10^6 cells/mL. Cells were supplemented with 150 U/mL IL2 (PeproTech, 212-12), 20 ng/mL TGFβ (PeproTech, 100-21), and 1 nM retinol acid and seeded in anti-CD3 (BioLegend, 100340) -coated plates.

3.4.8 Transwell assay

24-well plates with 5 µm inserts were used. Treg cells were resuspended in 100 µL RPMI and added to the top insert. 650 µL of media was added to the lower chamber. Control media was RPMI with 2% FBS. B16F10 conditioned culture media was collected from B16F10 cells cultured in RPMI with 2% FBS for 2 days and filtered through a 0.45 µm filter. 16 days after B16F10 tumor cells injection into C57BL/6/J mice, tumors were harvested and homogenized in RPMI with 2% FBS. The tumor supernatant was centrifuged and filtered. 4 hours after incubation, migrated cells in the lower chamber were collected and quantified by flow cytometry with CountBright Absolute Counting Beads (Thermo Fisher Scientific, C36950).

3.4.9 T cell transfer model of colitis

Naïve CD4$^+$ T cells were isolated from CD45.1 mouse by sorting the CD4$^+$CD25$^-$CD62L$^+$CD44$^-$ population. CD4$^+$Foxp3-GFP$^+$ Treg cells were sorted from WT or *Ythdf2* cKO mice. CD4$^+$ T cells and Treg cells were prepared at a 2:1 ratio and injected into *Rag1*$^{-/-}$ mice to induce colitis. Each recipient mouse was injected with 5×10^5 naïve T cells. Mice were weighted every 2-3 days.

3.4.10 Histology analysis

Tissues were collected in cassettes and fixed in 10% neutral buffered formalin (Thermo Fisher Scientific, 22-220682) for 48 hours. Fixed tissues were embedded in paraffin wax and sectioned for hematoxylin and eosin staining. Images were taken by CRi Pannoramic SCAN 40× Whole Slide Scanner.

3.4.11 TNFα stimulation

Treg cells were resuspended in culture media with 10 ng/mL TNFα (InvivoGen, rcyc-htnfa). Cells were collected at various time points for protein or mRNA expression analysis.

3.4.12 RNA decay

Treg cells treated or untreated with TNFα were incubated with 5 μg/mL of Actinomycin D (Sigma-Aldrich, A9415). Cells were collected in Trizol (Thermo Fisher Scientific, 15596026) at indicated time points. Total RNA was isolated and quantified by RT-qPCR. The decay rate was fitted by one phase decay mode.

3.4.13 m^{6}A-IP

Total RNAs of Treg cells from the spleen or tumor were subjected to m^{6}A-IP using EpiMark *N*^{6}-Methyladenosin Enrichment Kit (NEB, E1610S) following the manual. Briefly, 30-50 ng total RNAs were spiked with 1 μL of 1:1000 diluted m^{6}A control RNA from the kit, and 10% was saved as input. The remaining 90% was enriched by m^{6}A antibody-bead conjugate and eluted by buffer RLT (Qiagen, 79216). Eluted RNAs were recovered by RNA Clean & Concentrator (Zymo, R1014) and subjected to library preparation or RT-qPCR.

3.4.14 RT-qPCR

cDNA was generated from RNA with PrimeScript RT Reagent Kit (Takara, RR037B). qPCR reactions were prepared with FastStart SYBR Green Master (Roche, 06924204001) and run by Roche LightCycler 96. Housekeeping genes *Gapdh*, *Hprt*, or *18S* were used as internal controls and the relative mRNA expression was calculated by $2^{-\Delta\Delta Ct}$. Sequences for qPCR primers are listed below.

Table 4: qPCR primers

*Nlrc3*_qPCR_F	GGAGTAACAGCATTGGACCACC
*Nlrc3*_qPCR_R	CTGTAGCATGGAGATGGTCTGG
*Traf3*_qPCR_F	GTGAACCTGCTGAAGGAGTGGA
*Traf3*_qPCR_R	TTCGGAGCATCTCCTTCTGCCT
*Nfkbie*_qPCR_F	AGCAACTCGAGGCGCTCACATA
*Nfkbie*_qPCR_R	GCCAAGCAACAGAATAGCACCG
*Nlrc5*_qPCR_F	AGTGCAGCTGGTGAAGTCTC
*Nlrc5*_qPCR_R	TCCCGGACAGCAAGAGTTTC
*Tnfaip3*_qPCR_F	CAGTGGGAAGGGACACAACT
*Tnfaip3*_qPCR_R	GCAGTGGCAGAAACTTCCTC
*Tnfrsf1b*_qPCR_F	TGACAGGAAGGCTCAGATGTGC
*Tnfrsf1b*_qPCR_R	ATGCTTGCCTCACAGTCCGCAC
*Ythdf2*_qPCR_F	ACCAACTCTAGGGACACTCA
*Ythdf2*_qPCR_R	GGATAAGGAGATGCAACCGT
*18s*_qPCR_F	GCAATTATTCCCCATGAACG
*18s*_qPCR_R	GGCCTCACTAAACCATCCAA
*Gapdh*_qPCR_F	CATCACTGCCACCCAGAAGACTG
*Gapdh*_qPCR_R	ATGCCAGTGAGCTTCCCGTTCAG
*Hprt1*_qPCR_F	CTGGTGAAAAGGACCTCTCGAAG
*Hprt1*_qPCR_R	CCAGTTTCACTAATGACACAAACG
m^{6}A+ctr_qPCR_F	CGACATTCCTGAGATTCCTGG
m^{6}A+ctr_qPCR_R	TTGAGCAGGTCAGAACACTG

3.4.15 RNA-seq library preparation

CD4-enriched TILs were stained with DAPI, CD45, and CD4. Live $CD45^+CD4^+GFP^+$ Treg cells were sorted at 4 °C into Trizol (Invitrogen) for RNA-seq. For YTHDF2 RIP-seq, intratumoral Treg cells were sorted into lysis buffer (50 mM HEPES, pH 7.4, 150 mM KCl, 2 mM EDTA, 0.5% NP40, 0.5 mM DTT, protease inhibitor (Roche), and SUPERase·In RNase Inhibitor (Thermo Fisher Scientific, AM2696)) and placed on ice for 30 minutes. 20 μL Protein A Dynabeads (Thermo Fisher Scientific, 10008D) were washed with lysis buffer and incubated with 2 μg anti-YTHDF2 (Aviva Systems Biology, ARP67917_P050) for 30 minutes at 4 °C. Beads were washed twice with lysis buffer. Cell lysis was centrifuged at 20,000 × g for 15 minutes. 10% of the lysis was stored in Trizol as the input, and the rest was added to bead-antibody conjugates to rotate at 4 °C for 4 hours. After incubation, beads were washed with NT2 buffer (50 mM HEPES, pH 7.4, 200 mM NaCl, 2 mM EDTA, 0.05% NP40, 0.5 mM DTT, protease inhibitor, and RNase inhibitor) 6 times and resuspended in Trizol. RNAs were isolated by chloroform and precipitated by isopropanol following the manufacturer's protocol. Genomic DNA was removed by DNase I and purified by RNA Clean & Concentrator. RNA libraries were constructed with the SMARTer Stranded Total RNA-Seq Kit v2 (Takara, 634412). Samples were sequenced by Illumine Hiseq 4000 with single-end 50 bp read length.

3.4.16 Sequencing data analysis

Raw reads were trimmed with Trimmomatic-0.39[174], then aligned to mouse genome and transcriptome (mm10, version M19, 2018-08-30) using HISAT (version 2.1.0)[114] with '--rna-strandness R' parameters. Annotation files (version M19, 2018-08-30, in gtf format for mouse) were downloaded from GENCODE database (https://www.gencodegenes.org/).

For RNA-seq, reads on each GENCODE annotated gene were counted using HTSeq[175] and then differentially expressed genes were called using DESeq2 package in R[121] requiring at least 20 read counts in at least three samples with adjusted p-value < 0.05, and batch effect (mice cages) removed by introducing the batch in the design of the experiment as design = ~ batch + condition.

For RIP-seq, reads on each GENCODE annotated gene were counted using HTSeq[175] and then differentially expressed genes were called using DESeq2 package in R[121] requiring at least 10 read counts in at least two samples with adjusted p-value < 0.05. YTHDF2 target genes or m^6A modified genes were identified as differentially up-regulated genes comparing YTHDF2 or m^6A IP sample with the corresponding Input samples. m^6A modified genes were identified as differentially up-regulated genes comparing m^6A IP sample with the corresponding Input samples. Functional enrichment analysis was performed with DAVID[116].

3.4.17 Data availability

Raw and analyzed data for RNA-seq, YTHDF2-RIP-seq, and MeRIP-seq have been deposited to the National Center for Biotechnology Information Gene Expression Omnibus under the accession number GSE216960.

Chapter 4

Small molecule inhibitors of m^{6}A binding protein YTHDF2

4.1 Introduction: YTHDF2 as a therapeutic target

The molecular and biological functions of YTHDF2 in regulating m^{6}A-modified transcripts pose many clinical values. YTHDF2 is purposed to act as a transcriptome-switch through mediating mRNA degradation[40,41]. While microRNA mediates the degradation of selected mRNAs, the YTHDF2-mediated process can coordinate the degradation of hundreds of thousands of mRNAs, a pathway we proposed critical to cell state transition during differentiation or other cell state transitions. Indeed, YTHDF2 regulates the decay of transcription factors involved in stem cell self-renewal. Depletion of YTHDF2 in hematopoietic stem cells (HSCs) promotes expansion[107]. HSCs expanded in the absence of YTHDF2 did not lead to lineage bias. Consistently, in porcine bone marrow stem cells (pBMSCs), methylation of *JAK1* by METTL3 and regulation by YTHDF2 can tune STAT5 signaling and adipogenic differentiation[176]. Human induced pluripotent stem cells (iPSCs) need YTHDF2 to maintain pluripotency [177]. YTHDF2 decays neural development-related genes, and it is downregulated to support neural differentiation[10]. These findings show that YTHDF2 is a promising target to tune the stemness and expansion of various stem cells, which has a high potential for stem cell therapies.

YTHDF2 also supports cancer growth. It supports the generation and propagation of LSCs. Deletion of YTHDF2 in established AML cells induces cell apoptosis[163]. In liver cancer, *SOCS2* is suppressed by METTL3-mediated methylation and subsequent destabilization by YTHDF2[178]. *SOCS2* downregulation activates the JAK/STAT pathway and sustains tumor cell growth. Along with METTL3 and mRNA m^{6}A levels, YTHDF2 is also upregulated in triple-negative breast cancer (TNBC). Silencing of *YTHDF2* can inhibit the growth of TNBC cells, providing a new therapeutic target for TNBC. Furthermore, inhibition of YTHDF2 is especially valuable because deletion of YTHDF2 in various healthy tissue did not lead to observable defects, which allows for untargeted delivery of YTHDF2 inhibitors[166].

These studies drove the discovery of the first inhibitor targeting the binding pocket of YTHDF2, DC-Y13-27[60]. However, the potency and efficacy of this inhibitor are far from clinical applications. Further, the selectivity of DC-Y13-27 against other m^{6}A binding proteins that share the conserved YTH domain is not evaluated. Additional inhibitor with increased activity is needed for clinical translation.

4.2 Results

4.2.1 Fluorescence polarization (FP)-based high-throughput screening (HTS) assay

To discover small molecules that compete for the m^{6}A binding pocket, the YTH domain of YTHDF2 (YTH-2) was expressed and purified, and 9-mer DNA probes containing the m^{6}A motif GG6mACT and a fluorophore FAM at the 3' end (6mA-FAM probe) or GGACT with FAM (A-FAM probe) were synthesized. Electrophoretic mobility shift assay showed binding of the 6mA-FAM probe by the recombinant YTH-2 domain, and the binding affinity is similar to that performed with an m^{6}A motif-containing RNA probe[179] (Figure 4.1A). A-FAM probe showed weaker binding by the YTH-2 domain (Figure 4.1A). The DNA probes and YTH-2 domain recaptured the m^{6}A binding activity of YTHDF2.

Next, we evaluated the m^{6}A binding activity of YTH-2 in fluorescence polarization (FP) assay. The 6mA-FAM probe gained polarization signal as the concentration of YTH-2 increased (Figure 4.1B). YTH-2 domain also showed a preference for 6mA-FAM probes over the A-FAM probes (Figure 4.1B). The corresponding dissociation constant (K_D) values with 6mA-FAM and A-FAM probes were also similar to that obtained with RNA probes[179]. Optimizing reaction conditions, a range of salt, detergent, and DMSO concentrations were tested (Figure 4.1C-E). The interaction between YTH-2 and 6mA-FAM probe decreased with increasing NaCl and $MgCl_2$ concentration (Figure 4.1C), while unaffected by low concentrations of Triton X-100 (Figure 4.1D) and DMSO (Figure 4.1E). Polarization signal from YTH-2 and 6mA-FAM probe binding can be competed off with non-fluorescently-labeled 6mA probe, but not with A probes (Figure 4.1F). However, A-FAM probe binding with YTH-2 could be competed off with A probe, and more easily with the 6mA probe (Figure 4.1G). The FP assay recapitulated the binding activity of YTHDF2 with m^6A.

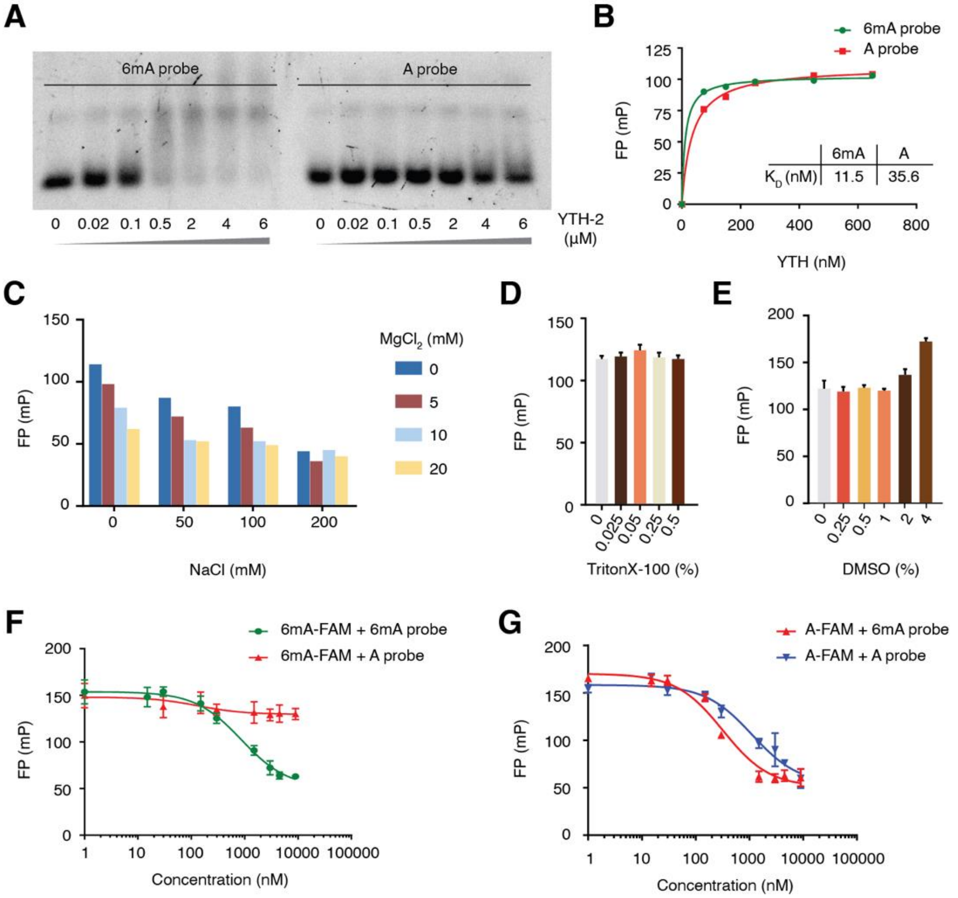

Figure 4.1 Recombinant YTH domain and synthetic probes capture the *in vivo* activities of YTHDF2

(**A**) 4 nM FITC-labeled RNA probes were incubated with YTH-2 protein concentrations ranging from 20 nM to 6 μM and the binding was visualized by gel shift assay. (**B**) Fluorescence

(**Figure 4.1, continued**) polarization of indicated FITC-labeled probes with increasing concentrations of YTH-2 protein. (**C**)-(**E**), Fluorescence polarization signal with different NaCl and $MgCl_2$ (**C**), TritonX-100 (**D**), or DMSO (**E**) concentrations were measured. In (**F**) and (**G**), the competitive displacement of YTH-2 binding to 6mA (**F**) or A (**G**) probe was evaluated with non-fluorescently labeled probes.

4.2.2 Screening of YTHDF2 inhibitors

We utilized the established FP-based HTS assay to reveal candidates that inhibit the YTHDF2 binding of m^{6}A (Figure 4.2A). By monitoring the change in FP signal from the 6mA-FAM probe, over 300,000 compounds were screened with YTH-2 and 6mA-FAM probe (Figure 4.2B). The average Z' was 0.71 with a hit rate of 0.13%. Hits were identified with inhibition greater than 2 standard deviations away from the median inhibition percentage. 432 initial hit compounds were reassessed with dose titration, and 187 of them demonstrated dose-dependent inhibition.

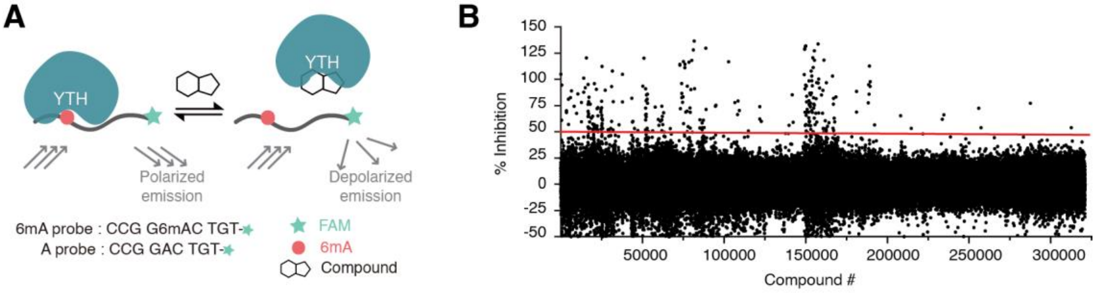

Figure 4.2 Pilot screen identifies candidate inhibitors of YTHDF2

(**A**) Scheme of FP-base screening assay with YTH-2 and DNA probes. (**B**) Compounds at 10 µM were screened with YTH-2 and DNA probe in FP assay. The solid line represents 50% inhibition.

The 187 dose-dependent hit compounds were subjected to structural analysis. The compounds were grouped by shared core structure, and 101 clusters were found, with the largest cluster containing 11 compounds. 14 compounds with different core structures were selected (Figure 4.3) based on their activities, drug-like properties, and potential for synthetic modifications. These compounds had IC_{50} values of 1-20 µM in the FP assay.

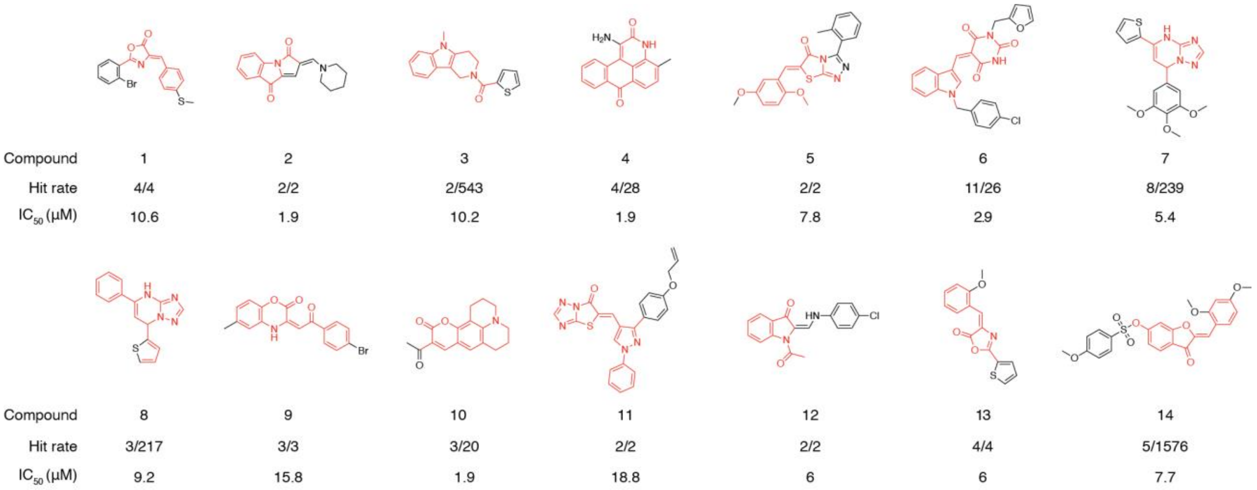

Compound	1	2	3	4	5	6	7
Hit rate	4/4	2/2	2/543	4/28	2/2	11/26	8/239
IC_{50} (μM)	10.6	1.9	10.2	1.9	7.8	2.9	5.4

Compound	8	9	10	11	12	13	14
Hit rate	3/217	3/3	3/20	2/2	2/2	4/4	5/1576
IC_{50} (μM)	9.2	15.8	1.9	18.8	6	6	7.7

Figure 4.3 Selected candidate inhibitors from structure analysis

Confirmed hits from the screen were analyzed and clustered by similar structures. The most active compound from each cluster was selected to represent the cluster. The hit rate indicates the number of hit compounds out of the number of similarly structured compounds screened. The inhibitory activity of each compound is indicated by IC_{50} values. The common core structure of each cluster is highlighted in red.

To further validate these compounds, cells were treated with these compounds to examine the effect on YTHDF2 targets. It is reported that YTHDF2 binds m^6A-methylated transcript *PRR5L* and facilitates its decay[180,181]. Knockdown of YTHDF2 also led to an accumulation of *PRR5L* in HeLa cells. Further, YTHDF2 RIP qPCR with HeLa cells enriched for *PRR5L*. The top compounds were added to HeLa cells at 10 μM to test for their activity in inhibiting YTHDF2 depend decay of *PRR5L*. Compound **7** showed the greatest accumulation of YTHDF2 target transcript *PRR5L*, suggesting the best activity in inhibiting YTHDF2 m^6A binding.

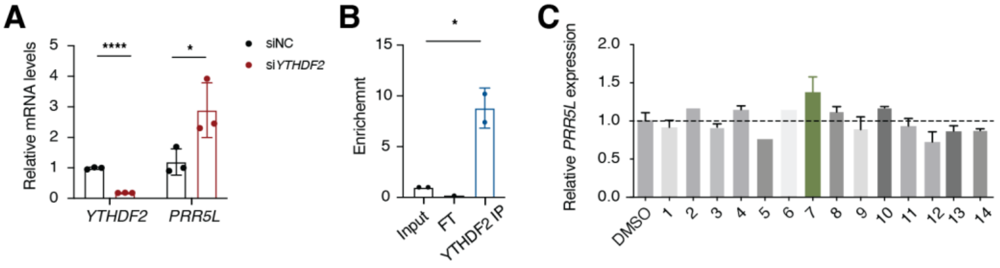

Figure 4.4 Compound 7 accumulates the abundance of YTHDF2 target transcript *PRR5L*

(**Figure 4.4, continued**) (**A**) Expression of *PRR5L* analyzed by RT-qPCR after YTHDF2 knockdown in HeLa cells. (**B**) Enrichment of *PRR5L* transcripts by YTHDF2 pull down with HeLa cells (**C**) Changes in PRR5L expression level after 12 hours incubations with 10 μM of the indicated compounds.

4.2.3 Optimization of Compound 7

While compound **7** exhibited inhibitory activities, it also showed high toxicity. Seven other compounds from the same cluster as compound **7** had similar inhibitory activities and shared the same core structure, which contains a two-membered ring (Figure 4.5A). We examined the toxicity of these compounds. We found that the removal of the methoxy groups could reduce the cytotoxicity while maintaining the activity (Figure 4.5B). To avoid toxicity, we continued our study with compound **7-3**, which contained no methoxy group but retained the inhibitory activities of compound 7 (Figure 4.5C).

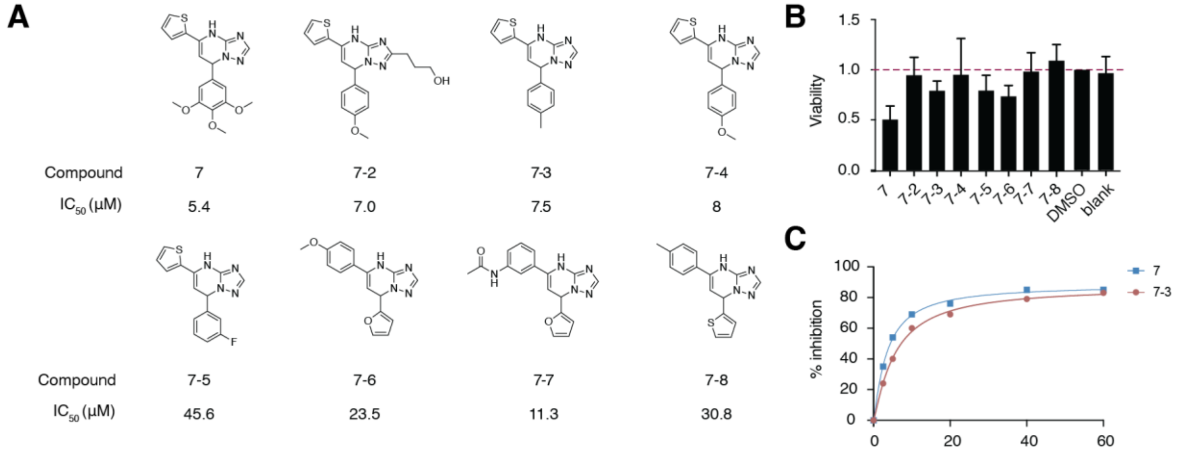

Figure 4.5 Analogs of compound 7 show similar inhibitory activity and reduced cytotoxicity

(**A**) Screening hit compounds from the same structural cluster as compound **7**. (**B**) HeLa cells were cultured with 10 μM of the indicated compounds for 2 days and cell survival was evaluated. (**C**) Inhibition of 6mA binding of YTHDF2 by compound **7** and **7-3** in FP assay.

To further optimize this cluster of compounds, we used compound **7-3** to build a binding model with the YTHDF2 protein (PDB: 4RDN) by the glide module using Schrodinger 2018. The thiophene ring of compound **7-3** was predicted to extend into the m^{6}A binding site, and establish two hydrogen bonds with Lys416 and Asn462 (Figure 4.6). We initiated a preliminary structure-activity relationship (SAR) study guided by this binding mode.

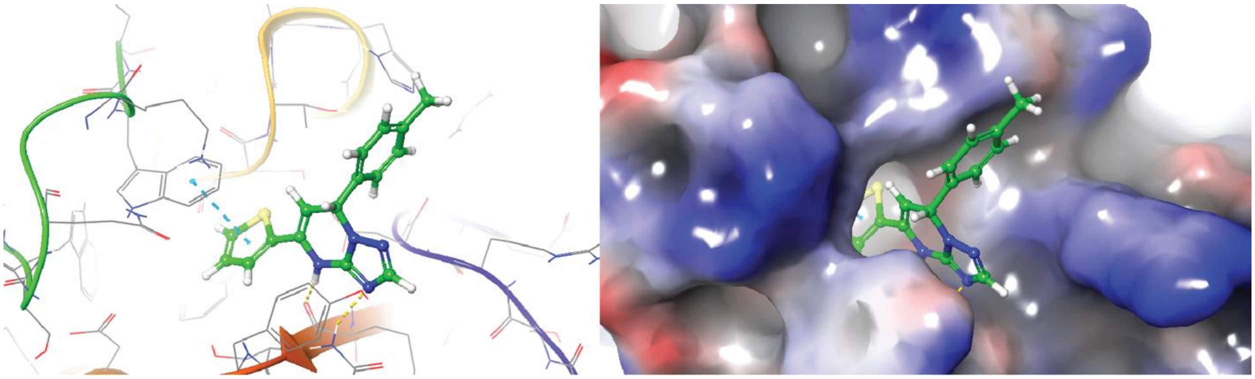

Figure 4.6 Predicted binding mode of compound 7-3

Docking mode of compound **7-3** in YTHDF2. Cartoon representation (left) of YTHDF2 showing the binding interactions with compound **7-3** and (right) the surface representation of YTHDF2.

Starting from hit **7-3** (K_D = 55 μM), we first replaced the thiophane ring with various aromatic rings, and only compound **13** showed a slight improvement of binding affinity (K_D = 39 μM) examined by the surface plasmon resonance (SPR) assay. Next, we introduced various groups to the position-2 of triazole ring, and found that the addition of a carboxyl group (**43**) could improve the binding affinity for over 10 folds (K_D = 2.5 μM) (Figure 4.7A and B). However, compound **43** also showed similar binding to the YTH domain of YTHDF1 (Figure 4.7C), indicating a lack of selectivity. The YTH domain contains tryptophan residues, and the tryptophan quenching assay showed **43** can significantly induce the quenching of tryptophan fluorescence with the calculated K_D value of 2.9 μM (Figure 4.7D), indicating the direct interaction between compound **43** and the YTH domain.

To understand how compound **43** binds to YTHDF2, we performed a docking study. The results showed that **43** adopt a binding mode similar to compound **7-3** (Figure 4.6 and 4.8). The 4-

cyanophenyl of **43** extended into the deep pocket of the m^{6}A binding pocket and the carboxyl group formed a salt bridge with the Arg527 (Figure 4.8).

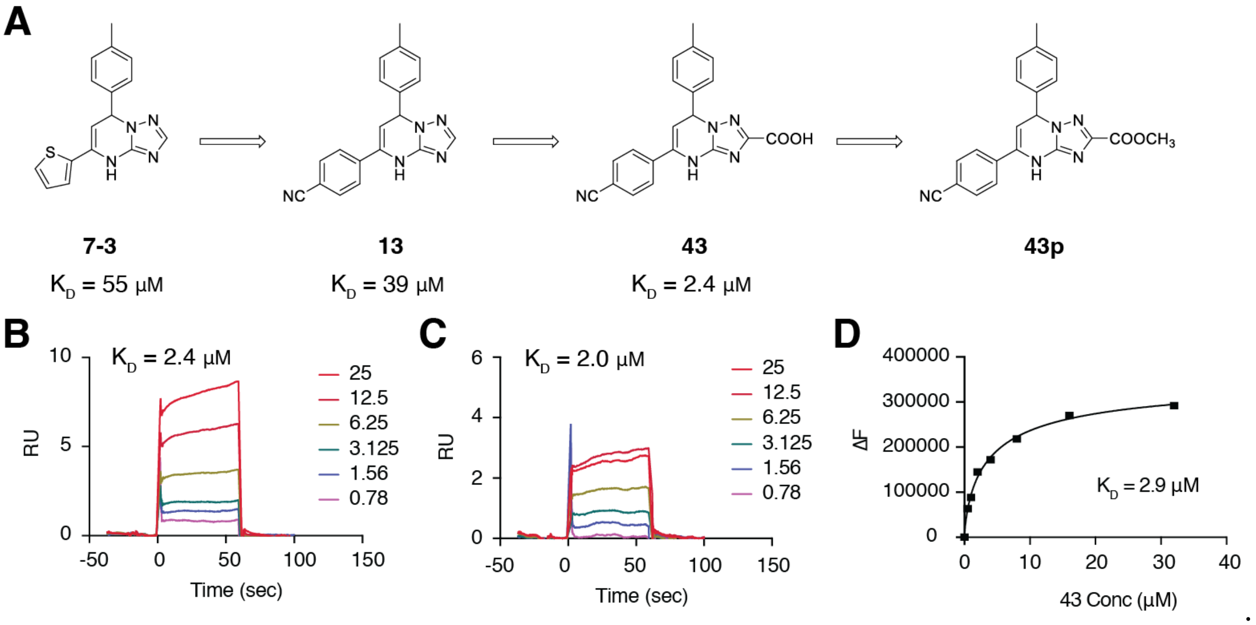

Figure 4.7 Synthetic derivatives of compound 7-3 showed improved activities

(**A**) Scheme of SAR studies leading to compound **43p**. In (**B**) and (**C**), binding affinities (K$_D$ values) between compound **43** and YTHDF2 (**B**) or YTHDF1 (**C**) were evaluated by SPR. (**C**) Tryptophan quenching of YTHDF2 by increasing concentration of compound **43**.

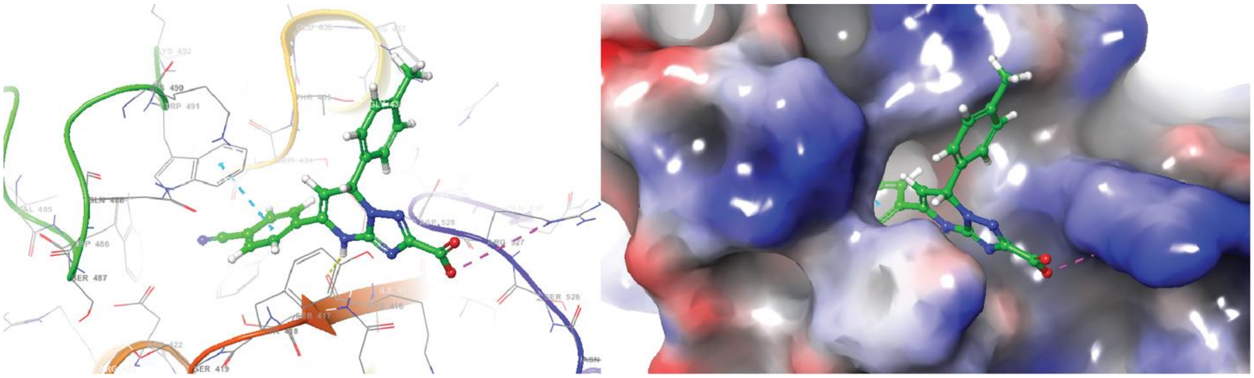

Figure 4.8 Predicted binding mode of compound 43

Docking mode of compound **43** in YTHDF2. Cartoon representation (left) of YTHDF2 showing the binding interactions with compound **43** and (right) the surface representation of YTHDF2.

4.2.4 Compound 43p could inhibit AML cell proliferation

However, when compound **43** did not lead to changes in *PRR5L* expression in HeLa cells. We reasoned that compound **43** has poor cell permeability (data not shown). To address this, the ester prodrug form of **43** (**43p**) was synthesized (Figure 4.7A). Monitoring the YTHDF2 target transcript, **43p** showed the ability to stabilize transcript *PRR5L* (Figure 4.9A). Next, we applied compound **43p** to Acute Myeloid Leukemia (AML) cell lines, since YTHDF2 is essential for AML propagation and cell proliferation through regulation of methylated *Tnfrsf2* transcripts[163]. **43p** inhibited the proliferation of AML cell lines OCI-AML3, SKM-1, and NOMO1 (Figure 4.9B). Further, cellular thermal shift assay (CETSA) revealed stabilization of YTHDF2 with **43p**, indicating direct target engagement by **43p** in AML cells (Figure 4.9C).

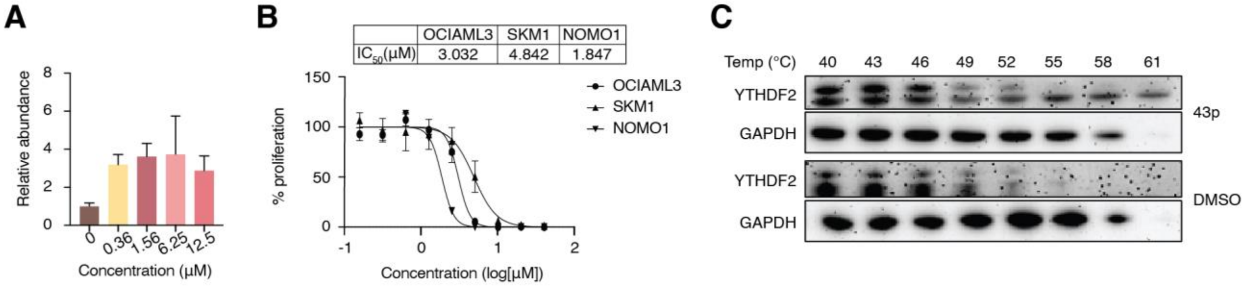

	OCIAML3	SKM1	NOMO1
IC_{50}(μM)	3.032	4.842	1.847

Figure 4.9 Cellular inhibition of YTHDF2 by compound 43p

(**A**) Relative expression level of PRR5L in HeLa cells after treatment with compound **43p** at the indicated concentrations. (**B**) Effect of **43p** treatment for 4 days on the proliferation of AML cell lines. (**C**) Representative western blot of the thermal stabilization of YTHDF2 protein by 40 μM of **43p** in AML cells.

4.3 Discussion and conclusion

A high-throughput screening assay measuring the fluorescence polarization of the 6mA-FAM probe by YTH-2 binding revealed over one hundred small molecule inhibitors that could inhibit YTH domain m^6A binding in a dose-dependent manner. We selected a cluster of hit compounds and performed further optimizations. While derivative **43p** resulted in significantly increased activity, selectivity against other YTH proteins could not be achieved. The similarity between the YTH proteins poses critical challenges in developing selective inhibitors. Although compound **43p** inhibited the proliferation of AML cells, it might be a result of pan-YTH inhibition, rather than specific inhibition of YTHDF2. This result also suggests the synergistic effect of YTH proteins in regulating AML cell survival.

4.4 Methods

4.4.1 Protein purification

His-tagged YTH domain (aa361-494) of human YTHDF2 was cloned into the pET-28a vector. The plasmid was transformed into BL21 (DE3) cells (Novagen) and expanded in LB culture at 37 °C until OD600 reached 0.6-0.8. 1 mM of Isopropyl-β-D-thiogalactopyranoside (IPTG) (Sigma-Aldrich) was added for protein expression induction at 16 °C for 20 hours. Cells were collected and resuspended with lysis buffer (20 mM Tris-HCl, pH 7.5, 400 mM NaCl, 1 mM PMSF) and lysed with Q500 Sonicator (QSonica). Cell debris was removed by centrifugation at 15,000 × g for 25 minutes. His-tagged YTH protein was purified with HisTrap HP column (Cytiva) using binding (lysis buffer + 30 mM imidazole) and elution buffer (lysis buffer + 500 mM imidazole). Proteins were stored in storage buffer (10 mM Tris-HCl, pH 7.5, 150 mM NaCl, and 1 mM DTT) at -80 °C.

4.4.2 EMSA (electrophoretic mobility shift assay/gel shift assay)

The DNA probes were synthesized with sequences of 5’-CCG G6mAC TGT-FAM and 5’-CCG GAC TGT-FAM (FAM = 6-carboxyfluorescein). YTH-2 protein and DNA probes were diluted in binding buffer (10 mM HEPES, pH 7.4, 50 mM KCl, 1 mM EDTA, 5% glycerol, 0.05% Triton X-100, 1 mM DTT, and 200 U/mL RNase inhibitor). 1 μL of DNA probe (4 nM final concentration) and 1μL of protein (20 nM, 100 nM, 500 nM, 2000 nM, 4000 nM, 6000 nM final concentration) were added to 8 μL binding buffer and incubated on ice for 30 minutes. The solution was run with a Novex 6% TBE gel (Invitrogen) at 4 °C for 90 minutes at 90V.

4.4.3 Fluorescence polarization assay

Fluorescence polarization assays were performed in 384-well plates. 220 nM YTH-2 protein and various concentrations of compounds were incubated in reaction buffer (25 mM HEPES, pH 7.4, pH 7.5, 2 mM DTT, 0.025% Triton X-100) at room temperature for 30 minutes. 7.5 nM probes were added and incubated for 40 minutes at 30 °C. The fluorescence polarization was measured by Synergy Plate Reader (BioTek) with excitation at 485 nm and emission at 525 nm. The DNA probes used are listed below.

Table 5: DNA probe sequences

6mA-FAM	5'-CCG G6mAC TGT-FAM
6mA	5'-CCG G6mAC TGT
A-FAM	5'-CCG GAC TGT-FAM
A	5'-CCG GAC TGT

4.4.4 Surface plasmon resonance (SPR) assay

SPR was performed on a Biacore 8K instrument (Cytiva) at room temperature with HBS-EP+ buffer, pH 7.6. YTH protein was loaded onto Sensor Chip CM5 (Cytiva) by amine-coupling. Compounds were serially diluted and injected for 60 s at 30 μL/minute, followed by dissociation for 120 seconds. Binding kinetics and affinity were fitted and calculated by Biacore Insight Evaluation Software using a 1:1 binding model.

4.4.5 Synthesis

4.4.5.1 Synthesis of intermediate (E)-4-(3-(p-tolyl)acryloyl)benzonitrile

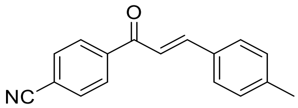

To the solution of 4-acetylbenzonitrile (6 g, 41.6 mmol) in MeOH (20 mL) was added 10% NaOH aqueous (20 mL) at 0 °C, and the mixture was stirred for 15 minutes. Then, 4-methylbenzaldehyde (5 g, 41.6 mmol) was added in portions. The resulting mixture was stirred for

30 minutes at ambient temperature. Then the mixture was filtered, and the solid was washed with cold MeOH and dried to give a white solid. (ESI): *m/z* =248.4 [M + H]$^+$.

4.4.5.2 Synthesis of 13, 43, and 43p

The mixture of (E)-4-(3-(p-tolyl)acryloyl)benzonitrile (0.2 g, 0.81 mmol) and different substituted 1H-1,2,4-triazol-5-amine (0.81 mmol) in DMF (100 uL) was stirred at 160 °C for 10 minutes, then the residues was cooled down, and acetone (5 mL) was added and stirred for 15 minutes. The mixture was then filtered, and the solid was washed with acetone and dried to give a white solid.

4-(7-(p-tolyl)-4,7-dihydro-[1,2,4]triazolo[1,5-a]pyrimidin-5-yl)benzonitrile (**13**)

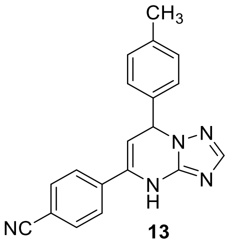

13

White solids, ^{1}H NMR (400 MHz, $CDCl_3$) δ 10.82 (s, 1H), 7.74 (q, *J* = 8.5 Hz, 4H), 7.34 (s, 1H), 7.29 – 7.24 (m, 3H), 7.20 (d, *J* = 7.9 Hz, 2H), 6.18 (d, *J* = 3.6 Hz, 1H), 5.23 (dd, *J* = 3.7, 1.6 Hz, 1H), 2.34 (s, 3H). (ESI): *m/z* =314.2 [M + H]$^+$.

5-(4-cyanophenyl)-7-(p-tolyl)-4,7-dihydro-[1,2,4]triazolo[1,5-a]pyrimidine-2-carboxylic acid (**43**)

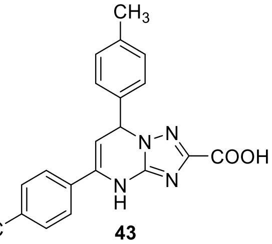

43

White solids, ^{1}H NMR (400 MHz, DMSO) δ 10.13 (s, 1H), 7.93 – 7.87 (m, 2H), 7.85 – 7.78 (m, 2H), 7.65 (s, 1H), 7.17 (s, 4H), 6.21 (d, *J* = 3.9 Hz, 1H), 5.41 (d, *J* = 3.9 Hz, 1H), 2.28 (s, 3H). (ESI): *m/z* =358.4 [M + H]$^+$.

Methyl 5-(4-cyanophenyl)-7-(p-tolyl)-4,7-dihydro-[1,2,4]triazolo[1,5-a]pyrimidine-2-carboxylate (**43P**)

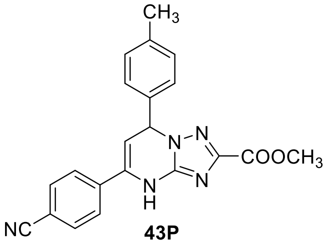

43P

White solids, ^{1}H NMR (400 MHz, DMSO) δ 10.40 (d, *J* = 1.8 Hz, 1H), 7.96 – 7.89 (m, 2H), 7.88 – 7.76 (m, 2H), 7.21 (d, *J* = 1.8 Hz, 4H), 6.30 (d, *J* = 3.8 Hz, 1H), 5.47 (dd, *J* = 3.8, 1.7 Hz, 1H), 3.78 (s, 3H), 2.29 (s, 3H). (ESI): *m/z* =372.2 $[M + H]^+$.

4.4.6 Cell culture

HeLa, NOMO1, OCI-AML3, and SKM1 cells were purchased from ATCC. HeLa cells were cultured in DMEM (Gibco 11965) supplemented with 10% (v/v) fetal bovine serum (Gibco), penicillin and streptomycin (Gibco) and grown at 37 °C with 5% CO_2. NOMO1, OCI-AML3, and SKM1 cells were cultured in RPMI 1640 (Gibco) supplemented with 10% (v/v) heat-inactivated fetal bovine serum (Gibco), penicillin and streptomycin (Gibco) and grown at 37 °C with 5% CO_2.

4.4.7 YTHDF2 RNA immunoprecipitation (RIP) RT-qPCR

HeLa cells were resuspended with lysis buffer (50 mM HEPES, pH 7.4, 150 mM KCl, 2 mM EDTA, 0.5% NP40, 0.5 mM DTT, with protease and RNase inhibitor) and rotated at 4 °C for 30 minutes. Debris was removed by centrifugation at 21,000 × g for 15 minutes. The supernatant was collected, and 10% lysate was saved as input. YTHDF2 antibody (Aviva) or rabbit IgG conjugated protein A beads (Invitrogen) were added to the lysate and rotated for 4 hours at 4 °C. Beads were washed 6 times with NT2 buffer (50 mM HEPES, pH 7.4, 200 mM NaCl, 2 mM EDTA, 0.05% NP40, 0.5 mM DTT). After washing, beads and input were resuspended in Trizol for RNA extraction. Input and IP-enriched RNAs were eluted in equal volumes of H_2O. Equal volumes of RNA were used for cDNA generation and qPCR reactions. % of input bound by YTHDF2 was calculated by % input = $2^{(Ct(RIP)-(Ct(Input)-\log_2(Input\ dilution\ factor)))}$.

4.4.8 siRNA Knockdown

HeLa cells were transfected with YTHDF2 (target sequence: AAGGCGTTCCCAATAGCCAA, Qiagen) or negative control (Qiagen) siRNA using Lipofectamine RNAiMAX reagent (Invitrogen) following the manufacturer's protocol. 48 hours post-transfection, cells were collected in Trizol for RNA extraction.

4.4.9 Cytotoxicity assay

HeLa cells were seeded in 96 well plates on day 0. Compounds were added to cells at a final concentration of 10 μM and incubated for 2 days. Cell viability was measured by MTS Assay Kit (Abcam) following the manufacturer's protocol.

4.4.10 Tryptophan quenching assay

300 μL of 5 μM YTH-2 proteins in binding buffer (20 mM HEPES, pH 7.4, 150 mM NaCl) were transferred to a micro fluorometer cell (Starna Cells). The fluorescence of tryptophan residues was measured by fluorometer Fluorolog (Horiba) with a 296 nm excitation wavelength and the emission from 310 to 650 nm was recorded. Compound **43** was spiked into the solution and stirred for one minute before taking measurements. The changes in maximum fluorescence intensity were monitored, and the K_D value was fitted using a four-parameter logistic equation in GraphPad Prism 9.0.

4.4.11 Cell proliferation assay

AML cells were seeded in 96 well plates and various concentrations of compounds were added. 4 days after culture, the cell number in each well was counted by CountBright Counting Beads (Invitrogen) using flow cytometry. Cell proliferation was normalized to controls.

4.4.12 Cellular thermal shift assay (CETSA)

OCI-AML cells were incubated with 40 μM of compound **43p** or DMSO for 24 hours. Cells were aliquoted evenly and heated at the indicated temperature for 3 minutes, followed by 25 °C for 3 minutes. Cells were lysed by 3 freeze-thaw cycles with liquid nitrogen. Cell debris was removed by centrifugation, and the soluble proteins were analyzed by western blotting.

Chapter 5

Summary and perspectives

5.1 Additional layer of regulation in immune cells

Transcription in immune cells is highly regulated to ensure proper cell differentiation, activation, and appropriate immune response[182,183]. Many transcription factors regulating immune cell development and function have been extensively studied[183]. However, the transcriptome can also be controlled by m^6A modifications in a transcription factor-independent manner. In B cell development, YTHDF2 acts as a transcriptome switch by mediating the decay of a group of m^6A-modifications transcripts. This showcased the unique ability of RNA modifications to modulate the transcriptome, which allows for the quick transition between cell states. Recently, it has been revealed that RNA modifications on chromosome-associated regulatory RNAs tune chromatin state and transcription[28,79]. m^6A can regulate the transcriptome not only through modulation of RNA metabolism, but also through regulation of chromatin states. While increasing studies revealed the role of m^6A in regulating key signaling pathways in a range of immune cell events, including T cell differentiation[38], Treg differentiation and function[44], macrophage polarization[45], and dendritic cell maturation[49], the regulatory roles of m^6A may go beyond the few transcripts and pathways reported.

The major functions of the immune system are to clear pathogens such as bacteria and viruses, neutralize harmful antigens, and eliminate tumor cells. However, in reality, the immune system can exert both tumor-suppressive and tumor-promoting roles shaped by the tumor microenvironment[184]. Cancer immunotherapy strategies that aim to promote anti-tumor immune response have gained tremendous interest but have limited success, likely owing to the complexity of immune cells and the tumor microenvironment. Further, treatments often face risks of side effects such as inflammation. Unique therapeutic targets that can overcome immunosuppression specifically in the tumor microenvironment are needed. My thesis work showed that transcriptional regulation of Treg cells by NF-kB signaling in the tumor is regulated through the m^{6}A-YTHDF2 axis. In Treg cells, m^{6}A modifications on NF-kB negative regulators allow for the indirect alteration of the transcriptome in response to tumor-specific signaling. This gain of function of YTHDF2 is particularly valuable for cancer immunotherapy, because it allows for specific inhibition of Treg cells in the tumor, avoiding undesired inflammation as seen in systematic Treg depletion[131].

Owing to its reversibility, m^{6}A modifications can quickly change to exert biological functions. One heterogeneity is attributed to the diverse range of m^{6}A effector proteins, each with different targets and functions. However, how immune cells utilize m^{6}A modifications to achieve cell-specific and context-dependent function is still unknown. My work showed that signaling in immune cells could lead to changes in m^{6}A modification abundance and activate the transcription of its regulating proteins to induce context-dependent functions. This may just be one of many mechanisms immune cells use m^{6}A, and questions about other regulations remain. What triggers the activation or deactivation of m^{6}A effector proteins? Does it affect the transcription of these proteins or post-translational modifications? What factors or RNA binding proteins assist the proper methylation at the specific target transcripts? And lastly, how do cancer cells take over these regulations in the tumor microenvironment to their own advantage? Investigating these questions will deepen our understanding of cancer immune escape mediated by RNA modifications.

5.2 New therapeutic targets for drug development

Similar to epigenetic modifications on histone and DNA, these RNA modifications can perturb gene expression without changing the DNA or RNA sequence. Studies of epigenetic marks have guided the discovery of successful anti-cancer drugs[3]. m^6A RNA modifications also show promising value as therapeutic targets in cancer and immune-related diseases. Successful inhibitors targeting m^6A modifications can benefit clinical studies beyond cancer and immunotherapy. For example, stem cell therapy is another field that would greatly benefit from drugs that inhibit m^6A effector proteins. m^6A modifications by METTL3 and METTL14 in various stem cells regulate self-renewal and differentiation[10,107,176,177]. The m^6A pathway provides opportunities to overcome the challenges in stem cell expansion for cell therapy. Neurodegenerative diseases would also benefit from inhibitors targeting the YTH family proteins. The YTHDF proteins contain low-complexity regions, which allow them to form phase-separated granules along with bound mRNAs. This protein aggregation is often associated with neurodegenerative disease[185]. In fragile X syndrome (FXS) models, low expression of YTHDF1 interacting protein FMRP allows YTHDF1 to form condensates. YTHDF1 exerts its translation-promoting function in these condensates, which also contain ribosome and YTHDF1-bound transcripts. Salvianolic acid C (SAC) is the first YTHDF1 targeting inhibitor that binds YTHDF1 with a K_D of 5-6 μM. Treatment of FXS organoid with SAC inhibited YTHDF1 mediated hyper-translation, which rescued neural progenitor cell proliferation and differentiation[85].

With the diverse proteins regulating m^6A modifications, there are many potentials for drug targets. METTL3 inhibitor, STC-15, is the first inhibitor in the clinical study intended to perturb m^6A modifications[70]. Some previously approved drugs were also later found to be potent inhibitors of RNA modification effectors. For example, entacapone, a drug for Parkinson's disease, is found to inhibit m^{6}A demethylase fat-mass and obesity-associated gene (FTO)[77].

My work showed the potential of modulating m^{6}A functions through YTHDF2 in boosting anti-tumor immune response. Limited efforts have been made to investigate inhibitors targeting the YTH reader proteins. Our work provided a robust screening method that could be adapted for other m^{6}A binding proteins, and revealed over one hundred potential candidates targeting YTHDF2. Compound **43p** is reported to inhibit the YTHDF2 binding of m6A and could inhibit AML cell proliferation with IC$_{50}$ values in the low μM range.

While we have reported a more potent inhibitor for YTHDF2, the activity is still far from clinical applications. Further optimizations or studies of other candidates are required to improve the potency. Further, this inhibitor lacks selectivity towards other YTH proteins. While **43p** could inhibit YTHDF2, the interaction with other YTH proteins must be carefully evaluated. How the co-inhibition of these proteins affects immune cells at the molecular level is also unknown.

5.3 The future of m^{6}A modifications as therapeutic targets

5.3.1 Achieving selective inhibition

Although RNA modifications hold great potential as therapeutic targets, challenges remain when transforming research-derived small molecules to the clinic. First, molecules targeting RNA-modifying proteins may need to be dosed within a control time window because functions of RNA modifications are highly context- and temporal-dependent. For example, *Mettl3* knockout in mice is embryonic lethal, while METTL3 is oncogenic in various cancers. Therefore, inhibitors targeting the writer proteins need to be dosed appropriately to balance the risk and benefits as a disease treatment. These inhibitors could also be coupled with targeted delivery and controlled release to achieve specific inhibition at the disease sites. While large-scale removal of an RNA modification by depleting the writer can be fatal, depletion of a single reader protein could be innocuous for cell survival.

Second, developing specific inhibitors for the proteins regulating RNA modifications can be challenging because RNA modifying and binding proteins often have similar catalytic domains or binding pockets. For example, ALKBH family proteins and FTO demethylate a wide range of modifications and each protein has a unique substrate preference. While they have a conserved catalytic domain, the substrate binding domain exerts selectivity[186]. Inhibitors that compete with α-KG can potentially inhibit all α-KG-dependent enzymes. However, to achieve specific inhibition, molecules should be designed to perturb the substrate binding domain. Similarly, the METTL3/14 proteins are two of the many METTL proteins that contain an S-adenosyl methionine (SAM) domain. In order to modulate a single aspect of RNA functions, selective reader inhibition is crucial. However, developing a competitive inhibitor for different YTHDF proteins is challenging owing to the highly conserved YTH domain. A better understanding of how similar proteins achieve substrate and functional selectivity would also help the development of specific inhibitors. Allosteric inhibitors are alternatives to target the unique regions of these proteins and achieve selectivity. Further, small molecules targeting the more unique regions of these proteins could guide the selective degradation of a specific protein utilizing PROTAC[187].

While there are strategies to achieve selective inhibition of the YTH family proteins, a pan-YTHDF inhibitor could also be valuable. There is evidence showing that the YTHDF proteins have overlapping functions and substrates[188]. However, methylation on chromosome-associated regulatory RNAs by METTL3 following decay by binder YTHDC1 serves as a switch to tune chromatin accessibility and downstream transcription[28]. YTHDC1 and YTHDF proteins show differences in the m^{6}A binding pocket, which may allow differential inhibition of YTHDC1 and YTHDF proteins.

However, more work is needed to establish the links between aberrant RNA modifications and human disease initiation and progression, and the corresponding inhibitor with selectivity and potency has to be carefully developed. Collectively, there is a plethora of studies suggesting RNA modifications have disease implications and the proteins regulating them could serve as therapeutic targets. Specific and potent inhibitors targeting the RNA modification pathways could have promising clinical success, as seen with DNA modification targeting drugs.

5.3.2 Site-specific modulation of m^{6}A

The dual roles of most RNA modification effectors in human diseases, especially in cancers, need to be taken into consideration. For example, though FTO and ALKBH5 play oncogenic roles in the majority of cancers studied, they can also be tumor suppressors in certain types of cancers. In these cases, site-specific m^{6}A demethylation of essential targets of FTO or ALKBH5 could attenuate tumorigenesis with minimal side effects. Several CRISPR-based site-specific m^{6}A editing technologies have been developed to edit the epitranscriptome site-specifically[189]. By linking dCas13b to ALKBH5, oncogenic mRNAs including *MYC* and *EGFR* can be selectively demethylated to regulate cancer cell proliferation[190]. In addition, targeting LINE1 RNA with dCas13b-FTO in *Fto* KO mESCs could at least partially rescue the defects in differentiation and self-renewal, as well as the dysregulated chromatin state and key gene expression[79]. Similarly, a series of targeted RNA methylation (TRM) systems could stimulate the methylation on 3'UTR of *Foxm1*, a hypomethylated target in glioblastoma[191]. Given that multiple CRISPR-mediated gene editing therapy are in clinical trials so far, these targeted-m^{6}A or other RNA modification modulators also offer a versatile toolbox for epitranscriptome-associated precision medicine.

Alternatively, site-specific modulation could be achieved with ASO. Specific binding at the methylation site by ASO could mediate decay. For example, degradation of m^6A-modified LINE1 RNA in mESC with ASO changed chromatin accessibility and led to a similar phenotype as *Fto* knockout mice[28,79,192]. These provide additional methods to regulate chromatin state besides modulating histone and DNA modifications.

5.3.3 Modulating m^6A to overcome challenges in cancer immunotherapy

Only a few populations in the tumor have been studied, and how m^6A regulates many other immune cell populations remains unknown. While targeting YTHDF2 could inhibit immune suppressive cells[60], it would also suppress natural killer cell anti-tumor functions[51]. m^6A could have contradicting roles in different cell types when orchestrating tumor immune response. Therefore, the global effect of m^6A modifications on tumor immune response would dictate how inhibitors should be applied to maximize the anti-tumor immune response. Further, m^6A is also dysregulated in cancer cells. METTL3 inhibitor, STC-15, showed an overall synergistic effect in inhibiting tumor cell growth while activating anti-tumor immune response[70].

The grand success of cancer immunotherapy is hindered by many challenges. Whether m^6A could resolve any of these challenges would have significant clinical value. Several biomarkers have been identified as targets for cancer immunotherapy. However, not all patients express these biomarkers. It is important to know whether tumor and immune cells use m^6A modifications as a common mechanism in most cancer patients and across different cancer types. Given the importance of m^6A modifications, it is likely that individual patients can have opposite directions of dysregulated m^6A and to a different extent. Therefore, having a diverse range of inhibitors targeting different effector proteins would allow for fine-tuning of m^6A modifications to restore its proper functions and provide personalized treatments based on the dysregulation of m^6A.

Another challenge in cancer immunotherapy is resistance. Genomic mutations leading to these resistances have been studied extensively, but mechanisms involving epigenetic changes have not been fully evaluated[193]. The m^6A pathway has shown a profound effect in interfering with resistance to chemotherapy[63,65] and immunotherapy[37,57,194,195]. Combining m^6A targeting inhibitors with other established treatments may enhance the efficacy and prolong patient response.

While our understanding of tumor-infiltrating immune cells is growing, there are also cold tumors that lack T cell infiltration. Cold tumors often fail to recruit and activate T cells. Some tumors lack immunogenic neoantigens. Neoantigen expression is caused by not only genetic mutation, but also mutations at the transcriptome and mutated splicing[196]. While m^6A modifications on RNA do not cause mutations, they could affect alternative splicing. No connections between m^6A modifications and neoantigens have been made. However, neoantigens alone could not activate an immune response. They need to be presented to T cells, and this process is regulated by m^6A. Deletion of YTHDF1 in dendritic cells prevented the degradation of tumor antigens and enhanced the cross-priming of T cells[37]. Trafficking of T cells is also required for tumor infiltration. While the function of m^6A has not been revealed in T cell trafficking, m^6A has been shown to regulate MDSC migration after radiotherapy[60]. These show the implications of targeting m^6A to fire up cold tumors.

List of references

1. Davis, F. F. & Allen, F. W. Ribonucleic acids from yeast which contain a fifth nucleotide. *J Biol Chem* **227**, 907-915 (1957).
2. Boccaletto, P. *et al.* MODOMICS: A database of RNA modification pathways. 2021 update. *Nucleic Acids Res* **50**, D231-D235 (2022).
3. Mohammad, H. P., Barbash, O. & Creasy, C. L. Targeting epigenetic modifications in cancer therapy: erasing the roadmap to cancer. *Nat Med* **25**, 403-418 (2019).
4. Dominissini, D. *et al.* Topology of the human and mouse m6A RNA methylomes revealed by m6A-seq. *Nature* **485**, 201-206 (2012).
5. Jia, G. *et al.* N^6-Methyladenosine in nuclear RNA is a major substrate of the obesity-associated FTO. *Nat Chem Biol* **7**, 885-887 (2011).
6. He, C. Grand Challenge Commentary: RNA epigenetics? *Nat Chem Biol* **6**, 863-865 (2010).
7. Zhang, Y., Lu, L. & Li, X. Detection technologies for RNA modifications. *Exp Mol Med* **54**, 1601-1616 (2022).
8. Geula, S. *et al.* m^{6}A mRNA methylation facilitates resolution of naïve pluripotency toward differentiation. *Science* **347**, 1002-1006 (2015).
9. Mendel, M. *et al.* Methylation of Structured RNA by the m^{6}A Writer METTL16 Is Essential for Mouse Embryonic Development. *Mol Cell* **71**, 986-1000.e11 (2018).
10. Li, M. *et al.* Ythdf2-mediated m^{6}A mRNA clearance modulates neural development in mice. *Genome Biol* **19**, 69 (2018).
11. Lin, Z. *et al.* Mettl3-/Mettl14-mediated mRNA N^6-methyladenosine modulates murine spermatogenesis. *Cell Res* **27**, 1216-1230 (2017).
12. Fustin, J. M. *et al.* Two Ck1δ transcripts regulated by m^{6}A methylation code for two antagonistic kinases in the control of the circadian clock. *Proc Natl Acad Sci U S A* **115**, 5980-5985 (2018).
13. Liu, N. *et al.* N^6-methyladenosine alters RNA structure to regulate binding of a low-complexity protein. *Nucleic Acids Res* **45**, 6051-6063 (2017).
14. Roundtree, I. A. *et al.* YTHDC1 mediates nuclear export of N^6-methyladenosine methylated mRNAs. *Elife* **6**, e31311 (2017).
15. Erales, J. *et al.* Evidence for rRNA 2′-O-methylation plasticity: Control of intrinsic translational capabilities of human ribosomes. *Proc Natl Acad Sci U S A* **114**, 12934-12939 (2017).
16. Liu, F. *et al.* ALKBH1-Mediated tRNA Demethylation Regulates Translation. *Cell* **167**, 816-828.e16 (2016).
17. Shi, H. *et al.* YTHDF3 facilitates translation and decay of N^6-methyladenosine-modified RNA. *Cell Res* **27**, 315-328 (2017).

18. Pandolfini, L. *et al.* METTL1 Promotes let-7 MicroRNA Processing via m^{7}G Methylation. *Mol Cell* **74**, 1278-1290.e9 (2019).

19. Abakir, A. *et al.* *N*^{6}-methyladenosine regulates the stability of RNA:DNA hybrids in human cells. *Nat Genet* **52**, 48-55 (2020).

20. Wei, J. & He, C. Chromatin and transcriptional regulation by reversible RNA methylation. *Curr Opin Cell Biol* **70**, 109-115 (2021).

21. Wei, C. M., Gershowitz, A. & Moss, B. Methylated nucleotides block 5′ terminus of HeLa cell messenger RNA. *Cell* **4**, 379-386 (1975).

22. Bokar, J. A., Shambaugh, M. E., Polayes, D., Matera, A. G. & Rottman, F. M. Purification and cDNA cloning of the AdoMet-binding subunit of the human mRNA (*N*^{6}-adenosine)-methyltransferase. *RNA* **3**, 1233-1247 (1997).

23. Liu, J. *et al.* A METTL3-METTL14 complex mediates mammalian nuclear RNA *N*^{6}-adenosine methylation. *Nat Chem Biol* **10**, 93-95 (2014).

24. Zheng, G. *et al.* ALKBH5 Is a Mammalian RNA Demethylase that Impacts RNA Metabolism and Mouse Fertility. *Mol Cell* **49**, 18-29 (2013).

25. Shi, R. *et al.* Linking the YTH domain to cancer: the importance of YTH family proteins in epigenetics. *Cell Death Dis* **12**, 346 (2021).

26. Wang, X. *et al.* *N*^{6}-methyladenosine modulates messenger RNA translation efficiency. *Cell* **161**, 1388-1399 (2015).

27. Wang, X. *et al.* *N*^{6}-methyladenosine-dependent regulation of messenger RNA stability. *Nature* **505**, 117-120 (2014).

28. Liu, J. *et al.* *N*^{6}-methyladenosine of chromosome-associated regulatory RNA regulates chromatin state and transcription. *Science* **367**, 580-586 (2020).

29. Hsu, P. J. *et al.* Ythdc2 is an *N*^{6}-methyladenosine binding protein that regulates mammalian spermatogenesis. *Cell Res* **27**, 1115-1127 (2017).

30. Huang, H. *et al.* Recognition of RNA *N*^{6}-methyladenosine by IGF2BP proteins enhances mRNA stability and translation. *Nat Cell Biol* **20**, 285-296 (2018).

31. Liu, N. *et al.* *N*^{6}-methyladenosine-dependent RNA structural switches regulate RNA-protein interactions. *Nature* **518**, 560-564 (2015).

32. Alarcón, C. R. *et al.* HNRNPA2B1 Is a Mediator of m^{6}A-Dependent Nuclear RNA Processing Events. *Cell* **162**, 1299-1308 (2015).

33. Cheng, Y. *et al.* m6A RNA Methylation Maintains Hematopoietic Stem Cell Identity and Symmetric Commitment. *Cell Rep* **28**, 1703-1716.e6 (2019).

34. Lee, H. *et al.* Stage-specific requirement for Mettl3-dependent m^{6}A mRNA methylation during haematopoietic stem cell differentiation. *Nat Cell Biol* **21**, 700-709 (2019).

35. Weng, H. *et al.* METTL14 Inhibits Hematopoietic Stem/Progenitor Differentiation and Promotes Leukemogenesis via mRNA m^{6}A Modification. *Cell Stem Cell* **22**, 191-205.e9 (2018).

36. Zhang, C. *et al.* m^{6}A modulates haematopoietic stem and progenitor cell specification. *Nature* **549**, 273-276 (2017).

37. Han, D. *et al.* Anti-tumour immunity controlled through mRNA m^{6}A methylation and YTHDF1 in dendritic cells. *Nature* **566**, 270-274 (2019).

38. Li, H. B. *et al.* m^{6}A mRNA methylation controls T cell homeostasis by targeting the IL-7/STAT5/SOCS pathways. *Nature* **548**, 338-342 (2017).

39. Liu, Y. *et al.* *N*^{6}-methyladenosine RNA modification–mediated cellular metabolism rewiring inhibits viral replication. *Science* **365**, 1171-1176 (2019).

40. Roundtree, I. A., Evans, M. E., Pan, T. & He, C. Dynamic RNA Modifications in Gene Expression Regulation. *Cell* **169**, 1187-1200 (2017).

41. Zhao, B. S. *et al.* m^{6}A-dependent maternal mRNA clearance facilitates zebrafish maternal-to-zygotic transition. *Nature* **542**, 475-478 (2017).

42. Chaplin, D. D. Overview of the immune response. *J Allergy Clin Immunol* **125**, S3-S23 (2010).

43. Marshall, J. S., Warrington, R., Watson, W. & Kim, H. L. An introduction to immunology and immunopathology. *Allergy Asthma Clin Immunol* **14**, 49 (2018).

44. Lu, T. X. *et al.* A New Model of Spontaneous Colitis in Mice Induced by Deletion of an RNA m^{6}A Methyltransferase Component METTL14 in T Cells. *Cell Mol Gastroenterol Hepatol* **10**, 747-761 (2020).

45. Liu, Y. *et al.* The *N*^{6}-methyladenosine (m^{6}A)-forming enzyme METTL3 facilitates M1 macrophage polarization through the methylation of *STAT1* mRNA. *Am J Physiol Cell Physiol* **317**, C762-C775 (2019).

46. Gu, X. *et al.* *N*^{6}-methyladenosine demethylase FTO promotes M1 and M2 macrophage activation. *Cell Signal* **69**, 109553 (2020).

47. Tong, J. *et al.* m^{6}A mRNA methylation sustains Treg suppressive functions. *Cell Res* **28**, 253-256 (2018).

48. Zhou, J. *et al.* m^{6}A demethylase ALKBH5 controls CD4$^+$ T cell pathogenicity and promotes autoimmunity. *Sci Adv* **7**, eabg0470 (2021).

49. Wang, H. *et al.* Mettl3-mediated mRNA m^{6}A methylation promotes dendritic cell activation. *Nat Commun* **10**, 1898 (2019).

50. Zheng, Q., Hou, J., Zhou, Y., Li, Z. & Cao, X. The RNA helicase DDX46 inhibits innate immunity by entrapping m^{6}A-demethylated antiviral transcripts in the nucleus. *Nat Immunol* **18**, 1094-1103 (2017).

51. Ma, S. *et al.* The RNA m6A reader YTHDF2 controls NK cell antitumor and antiviral immunity. *J Exp Med* **218**, e20210279 (2021).

52. Zhang, Y. *et al.* RNA-binding protein YTHDF3 suppresses interferon-dependent antiviral responses by promoting FOXO3 translation. *Proc Natl Acad Sci U S A* **116**, 976-981 (2019).

53. Jiang, T. *et al.* Tumor neoantigens: from basic research to clinical applications. *J Hematol Oncol* **12**, 93 (2019).

54. Beatty, G. L. & Gladney, W. L. Immune Escape Mechanisms as a Guide for Cancer Immunotherapy. *Clin Cancer Res* **21**, 687-692 (2015).

55. Liu, Y. *et al.* Tumors exploit FTO-mediated regulation of glycolytic metabolism to evade immune surveillance. *Cell Metab* **33**, 1221-1233.e11 (2021).

56. Qiu, X. *et al.* m^{6}A demethylase ALKBH5 regulates PD-L1 expression and tumor immunoenvironment in intrahepatic cholangiocarcinoma. *Cancer Res* **81**, 4778-4793 (2021).

57. Li, N. *et al.* ALKBH5 regulates anti-PD-1 therapy response by modulating lactate and suppressive immune cell accumulation in tumor microenvironment. *Proc Natl Acad Sci U S A* **117**, 20159-20170 (2020).

58. Dong, F. *et al.* ALKBH5 Facilitates Hypoxia-Induced Paraspeckle Assembly and IL8 Secretion to Generate an Immunosuppressive Tumor Microenvironment. *Cancer Res* **81**, 5876-5888 (2021).

59. Liu, X. S. *et al.* Comprehensive Analysis of YTHDF1 Immune Infiltrates and ceRNA in Human Esophageal Carcinoma. *Front Genet* **13**, 835265 (2022).

60. Wang, L. *et al.* YTHDF2 inhibition potentiates radiotherapy antitumor efficacy. *Cancer Cell* (2023) doi:10.1016/j.ccell.2023.04.019.

61. Dong, L. *et al.* The loss of RNA N^6-adenosine methyltransferase Mettl14 in tumor-associated macrophages promotes CD8$^+$ T cell dysfunction and tumor growth. *Cancer Cell* **39**, 945-957.e10 (2021).

62. Wang, L. *et al.* m^{6}A RNA Methylation Regulator HNRNPC Contributes to Tumorigenesis and Predicts Prognosis in Glioblastoma Multiforme. *Front Oncol* **10**, 536875 (2020).

63. Chen, P. *et al.* Targeting YTHDF1 effectively re-sensitizes cisplatin-resistant colon cancer cells by modulating GLS-mediated glutamine metabolism. *Mol Ther Oncolytics* **20**, 228-239 (2021).

64. Nishizawa, Y. *et al.* Oncogene c-Myc promotes epitranscriptome m^{6}A reader YTHDF1 expression in colorectal cancer. *Oncotarget* **9**, 7476-7486 (2018).

65. Yan, F. *et al.* A dynamic N^6-methyladenosine methylome regulates intrinsic and acquired resistance to tyrosine kinase inhibitors. *Cell Res* **28**, 1062-1076 (2018).

66. Moroz-Omori, E. v. *et al.* METTL3 Inhibitors for Epitranscriptomic Modulation of Cellular Processes. *ChemMedChem* **16**, 3035-3043 (2021).

67. Dolbois, A. *et al.* 1,4,9-Triazaspiro[5.5]undecan-2-one Derivatives as Potent and Selective METTL3 Inhibitors. *J Med Chem* **64**, 12738-12760 (2021).

68. Yanagi, Y. *et al.* EBV Exploits RNA m^{6}A Modification to Promote Cell Survival and Progeny Virus Production During Lytic Cycle. *Front Microbiol* **13**, 870816 (2022).

69. Yankova, E. *et al.* Small-molecule inhibition of METTL3 as a strategy against myeloid leukaemia. *Nature* **593**, 597-601 (2021).

70. Ofir-Rosenfeld, Y. *et al.* STC-15, an oral small molecule inhibitor of the RNA methyltransferase METTL3, inhibits tumour growth through activation of anti-cancer

immune responses associated with increased interferon signalling, and synergises with T cell checkpoint blockade. *Eur J Cancer* **174**, S123 (2022).

71. Chen, B. *et al.* Development of cell-active N^6-methyladenosine RNA demethylase FTO inhibitor. *J Am Chem Soc* **134**, 17963-17971 (2012).

72. Zheng, G. *et al.* Synthesis of a FTO inhibitor with anticonvulsant activity. *ACS Chem Neurosci* **5**, 658-665 (2014).

73. Singh, B. *et al.* Important role of FTO in the survival of rare panresistant triple-negative inflammatory breast cancer cells facing a severe metabolic challenge. *PLoS One* **11**, e0159072 (2016).

74. Toh, J. D. W. *et al.* A strategy based on nucleotide specificity leads to a subfamily-selective and cell-active inhibitor of N^6-methyladenosine demethylase FTO. *Chem Sci* **6**, 112-122 (2015).

75. Su, R. *et al.* R-2HG Exhibits Anti-tumor Activity by Targeting FTO/m^{6}A/MYC/CEBPA Signaling. *Cell* **172**, 90-105.e23 (2018).

76. Huang, Y. *et al.* Meclofenamic acid selectively inhibits FTO demethylation of m^{6}A over ALKBH5. *Nucleic Acids Res* **43**, 373-384 (2015).

77. Peng, S. *et al.* Identification of entacapone as a chemical inhibitor of FTO mediating metabolic regulation through FOXO1. *Sci Transl Med* **11**, eaau7116 (2019).

78. Huang, Y. *et al.* Small-Molecule Targeting of Oncogenic FTO Demethylase in Acute Myeloid Leukemia. *Cancer Cell* **35**, 677-691.e10 (2019).

79. Wei, J. *et al.* FTO mediates LINE1 m^{6}A demethylation and chromatin regulation in mESCs and mouse development. *Science* **376**, 968-973 (2022).

80. Su, R. *et al.* Targeting FTO Suppresses Cancer Stem Cell Maintenance and Immune Evasion. *Cancer Cell* **38**, 79-96.e11 (2020).

81. Huff, S., Tiwari, S. K., Gonzalez, G. M., Wang, Y. & Rana, T. M. m^{6}A-RNA Demethylase FTO Inhibitors Impair Self-Renewal in Glioblastoma Stem Cells. *ACS Chem Biol* **16**, 324-333 (2021).

82. Malacrida, A. *et al.* 3D proteome-wide scale screening and activity evaluation of a new ALKBH5 inhibitor in U87 glioblastoma cell line. *Bioorg Med Chem* **28**, 115300 (2020).

83. Selberg, S., Seli, N., Kankuri, E. & Karelson, M. Rational Design of Novel Anticancer Small-Molecule RNA m^{6}A Demethylase ALKBH5 Inhibitors. *ACS Omega* **6**, 13310-13320 (2021).

84. Fang, Z. *et al.* Discovery of a potent, selective and cell active inhibitor of m^{6}A demethylase ALKBH5. *Eur J Med Chem* **238**, 114446 (2022).

85. Zou, Z. *et al.* FMRP phosphorylation modulates neuronal translation through YTHDF1. Preprint at *bioRxiv* https://doi.org/10.1101/2022.11.29.518448 (2022).

86. Clark, M. R., Mandal, M., Ochiai, K. & Singh, H. Orchestrating B cell lymphopoiesis through interplay of IL-7 receptor and pre-B cell receptor signalling. *Nat Rev Immunol* **14**, 69-80 (2014).

87. Mårtensson, I.-L., Almqvist, N., Grimsholm, O. & Bernardi, A. I. The pre-B cell receptor checkpoint. *FEBS Lett* **584**, 2572-2579 (2010).

88. Busslinger, M. Transcriptional Control of Early B Cell Development. *Annu Rev Immunol* **22**, 55-79 (2004).

89. Hagman, J. & Lukin, K. Transcription factors drive B cell development. *Curr Opin Immunol* **18**, 127-134 (2006).

90. Barneda-Zahonero, B., Roman-Gonzalez, L., Collazo, O., Mahmoudi, T. & Parra, M. Epigenetic Regulation of B Lymphocyte Differentiation, Transdifferentiation, and Reprogramming. *Comp Funct Genomics* **2012**, 1-10 (2012).

91. Mandal, M. *et al.* BRWD1 orchestrates epigenetic landscape of late B lymphopoiesis. *Nat Commun* **9**, 3888 (2018).

92. Wu, H. *et al.* Epigenetic regulation in B-cell maturation and its dysregulation in autoimmunity. *Cell Mol Immunol* **15**, 676-684 (2018).

93. Galloway, A. *et al.* RNA-binding proteins ZFP36L1 and ZFP36L2 promote cell quiescence. *Science* **352**, 453-459 (2016).

94. Inoue, T. *et al.* CNOT3 contributes to early B cell development by controlling Igh rearrangement and p53 mRNA stability. *J Exp Med* **212**, 1465-1479 (2015).

95. Zhou, Y. *et al.* Lin28b promotes fetal B lymphopoiesis through the transcription factor Arid3a. *J Exp Med* **212**, 569-580 (2015).

96. Coffre, M. *et al.* miRNAs Are Essential for the Regulation of the PI3K/AKT/FOXO Pathway and Receptor Editing during B Cell Maturation. *Cell Rep* **17**, 2271-2285 (2016).

97. Lai, M. *et al.* Regulation of B-cell development and tolerance by different members of the miR-17~92 family microRNAs. *Nat Commun* **7**, 12207 (2016).

98. Rodriguez, A. *et al.* Requirement of *bic/microRNA-155* for Normal Immune Function. *Science* **316**, 608-611 (2007).

99. Malin, S. *et al.* Role of STAT5 in controlling cell survival and immunoglobulin gene recombination during pro-B cell development. *Nat Immunol* **11**, 171-179 (2010).

100. Timblin, G. A. & Schlissel, M. S. Ebf1 and c-Myb Repress *Rag* Transcription Downstream of Stat5 during Early B Cell Development. *J Immunol* **191**, 4676-4687 (2013).

101. Cooper, A. B. *et al.* A unique function for cyclin D3 in early B cell development. *Nat Immunol* **7**, 489-497 (2006).

102. Mandal, M. *et al.* Ras orchestrates exit from the cell cycle and light-chain recombination during early B cell development. *Nat Immunol* **10**, 1110-1117 (2009).

103. Fu, Y., Dominissini, D., Rechavi, G. & He, C. Gene expression regulation mediated through reversible m6A RNA methylation. *Nat Rev Genet* **15**, 293-306 (2014).

104. Ochiai, K. *et al.* A self-reinforcing regulatory network triggered by limiting IL-7 activates pre-BCR signaling and differentiation. *Nat Immunol* **13**, 300-307 (2012).

105. Ping, X. L. *et al.* Mammalian WTAP is a regulatory subunit of the RNA N^6-methyladenosine methyltransferase. *Cell Res* **24**, 177-189 (2014).

106. Zhao, B. S., Roundtree, I. A. & He, C. Post-transcriptional gene regulation by mRNA modifications. *Nat Rev Mol Cell Biol* **18**, 31-42 (2016).

107. Li, Z. *et al.* Suppression of m^{6}A reader Ythdf2 promotes hematopoietic stem cell expansion. *Cell Res* **28**, 904-917 (2018).

108. Hobeika, E. *et al.* Testing gene function early in the B cell lineage in mb1-cre mice. *Proc Ntl Acad Sci U S A* **103**, 13789-13794 (2006).

109. Yoon, K. J. *et al.* Temporal Control of Mammalian Cortical Neurogenesis by m^{6}A Methylation. *Cell* **171**, 877-889.e17 (2017).

110. Phan, T. G. *et al.* B Cell Receptor-independent Stimuli Trigger Immunoglobulin (Ig) Class Switch Recombination and Production of IgG Autoantibodies by Anergic Self-Reactive B Cells. *J Exp Med* **197**, 845-860 (2003).

111. Mombaerts, P. *et al.* RAG-1-deficient mice have no mature B and T lymphocytes. *Cell* **68**, 869-877 (1992).

112. Johnson, K. *et al.* Regulation of Immunoglobulin Light-Chain Recombination by the Transcription Factor IRF-4 and the Attenuation of Interleukin-7 Signaling. *Immunity* **28**, 335-345 (2008).

113. Liu, H. *et al.* Yin Yang 1 is a critical regulator of B-cell development. *Genes Dev* **21**, 1179-1189 (2007).

114. Kim, D., Paggi, J. M., Park, C., Bennett, C. & Salzberg, S. L. Graph-based genome alignment and genotyping with HISAT2 and HISAT-genotype. *Nat Biotechnol* **37**, 907-915 (2019).

115. Trapnell, C. *et al.* Differential analysis of gene regulation at transcript resolution with RNA-seq. *Nat Biotechnol* **31**, 46-53 (2013).

116. Huang, D. W., Sherman, B. T. & Lempicki, R. A. Systematic and integrative analysis of large gene lists using DAVID bioinformatics resources. *Nat Protoc* **4**, 44-57 (2009).

117. Saldanha, A. J. Java Treeview-extensible visualization of microarray data. *Bioinformatics* **20**, 3246-3248 (2004).

118. Meng, J. *et al.* A protocol for RNA methylation differential analysis with MeRIP-Seq data and exomePeak R/Bioconductor package. *Methods* **69**, 274-281 (2014).

119. Ramírez, F. *et al.* deepTools2: a next generation web server for deep-sequencing data analysis. *Nucleic Acids Res* **44**, W160-W165 (2016).

120. Liao, Y., Smyth, G. K. & Shi, W. The R package Rsubread is easier, faster, cheaper and better for alignment and quantification of RNA sequencing reads. *Nucleic Acids Res* **47**, e47-e47 (2019).

121. Love, M. I., Huber, W. & Anders, S. Moderated estimation of fold change and dispersion for RNA-seq data with DESeq2. *Genome Biol* **15**, 550 (2014).

122. Ribas, A. & Wolchok, J. D. Cancer immunotherapy using checkpoint blockade. *Science* **359**, 1350-1355 (2018).

123. Hori, S., Nomura, T. & Sakaguchi, S. Control of regulatory T cell development by the transcription factor Foxp3. *Science* **299**, 1057-1061 (2003).

124. Vignali, D. A. A., Collison, L. W. & Workman, C. J. How regulatory T cells work. *Nat Rev Immunol* **8**, 523-532 (2008).

125. Josefowicz, S. Z., Lu, L. F. & Rudensky, A. Y. Regulatory T cells: Mechanisms of differentiation and function. *Annu Rev Immunol* **30**, 531-564 (2012).

126. Chaudhary, B. & Elkord, E. Regulatory T cells in the tumor microenvironment and cancer progression: Role and therapeutic targeting. *Vaccines* **4**, 28 (2016).

127. Onizuka, S. *et al.* Tumor rejection by in vivo administration of anti-CD25 (interleukin-2 receptor α) monoclonal antibody. *Cancer Res* **59**, 3128-3133 (1999).

128. Shimizu, J., Yamazaki, S. & Sakaguchi, S. Induction of tumor immunity by removing CD25+CD4+ T cells: a common basis between tumor immunity and autoimmunity. *J Immunol* **163**, 5211-5218 (1999).

129. Vargas, F. A. *et al.* Fc Effector Function Contributes to the Activity of Human Anti-CTLA-4 Antibodies. *Cancer Cell* **33**, 649-663 (2018).

130. Walter, S. *et al.* Multipeptide immune response to cancer vaccine IMA901 after single-dose cyclophosphamide associates with longer patient survival. *Nat Med* **18**, 1254-1261 (2012).

131. Kroschinsky, F. *et al.* New drugs, new toxicities: Severe side effects of modern targeted and immunotherapy of cancer and their management. *Crit Care* **21**, 89 (2017).

132. He, P. C. & He, C. m^{6}A RNA methylation: from mechanisms to therapeutic potential. *EMBO J.* **40**, e105977 (2021).

133. Wang, T., Kong, S., Tao, M. & Ju, S. The potential role of RNA N6-methyladenosine in Cancer progression. *Molecular Cancer* **19**, 88 (2020).

134. Chen, X. Y., Zhang, J. & Zhu, J. S. The role of m6A RNA methylation in human cancer. *Molecular Cancer* **18**, 103 (2019).

135. De Simone, M. *et al.* Transcriptional Landscape of Human Tissue Lymphocytes Unveils Uniqueness of Tumor-Infiltrating T Regulatory Cells. *Immunity* **45**, 1135-1147 (2016).

136. Magnuson, A. M. *et al.* Identification and validation of a tumor-infiltrating Treg transcriptional signature conserved across species and tumor types. *Proc Natl Acad Sci U S A* **115**, E10672-E10681 (2018).

137. Shi, H. *et al.* m^{6}A facilitates hippocampus-dependent learning and memory through YTHDF1. *Nature* **563**, 249-253 (2018).

138. Engel, M. *et al.* The Role of m6A/m-RNA Methylation in Stress Response Regulation. *Neuron* **99**, 389-403 (2018).

139. Winkler, R. *et al.* m^{6}A modification controls the innate immune response to infection by targeting type I interferons. *Nat Immunol* **20**, 173–182 (2019).

140. Frye, M., Harada, B. T., Behm, M. & He, C. RNA modifications modulate gene expression during development. *Science* **361**, 1346-1349 (2018).

141. Wang, H. *et al.* Loss of YTHDF2-mediated m^{6}A-dependent mRNA clearance facilitates hematopoietic stem cell regeneration. *Cell Research* **28**, 1035-1038 (2018).

142. Yu, R., Li, Q., Feng, Z., Cai, L. & Xu, Q. m^{6}A reader YTHDF2 regulates LPS-induced inflammatory response. *Int J Mol Sci* **20**, 1323 (2019).

143. Li, C., Jiang, P., Wei, S., Xu, X. & Wang, J. Regulatory T cells in tumor microenvironment: New mechanisms, potential therapeutic strategies and future prospects. *Molecular Cancer* **19**, 116 (2020).

144. Paluskievicz, C. M. *et al.* T regulatory cells and priming the suppressive tumor microenvironment. *Front Immunol* **10**, 2453 (2019).

145. Knutson, K. L. & Disis, M. L. Tumor antigen-specific T helper cells in cancer immunity and immunotherapy. *Cancer Immunol Immunother* **54**, 721-728 (2005).

146. Kim, H. R. *et al.* Tumor microenvironment dictates regulatory T cell phenotype: Upregulated immune checkpoints reinforce suppressive function. *J Immunother Cancer* **7**, 339 (2019).

147. Onda, M., Kobayashi, K. & Pastan, I. Depletion of regulatory T cells in tumors with an anti-CD25 immunotoxin induces CD8 T cell-mediated systemic antitumor immunity. *Proc Natl Acad Sci USA.* **116**, 4575-4582 (2019).

148. Moo-Young, T. A. *et al.* Tumor-derived TGF-β mediates conversion of CD4+Foxp3+ regulatory T cells in a murine model of pancreas cancer. *J Immunother* **32**, 12-21 (2009).

149. Cui, J. *et al.* NLRC5 Negatively regulates the NF-κB and type I interferon signaling pathways. *Cell* **141**, 483-496 (2010).

150. Kearns, J. D., Basak, S., Werner, S. L., Huang, C. S. & Hoffmann, A. IκBε provides negative feedback to control NF-κB oscillations, signaling dynamics, and inflammatory gene expression. *J Cell Biol.* **173**, 659-664 (2006).

151. Takaori-Kondo, A. *et al.* Both amino- and carboxyl-terminal domains of TRAF3 negatively regulate NF-κB activation induced by OX40 signaling. *Biochem Biophys Res Commun* **272**, 856-863 (2000).

152. Schneider, M. *et al.* The innate immune sensor NLRC3 attenuates Toll-like receptor signaling via modification of the signaling adaptor TRAF6 and transcription factor NF-κB. *Nat Immunol* **13**, 823-831 (2012).

153. Ashall, L. *et al.* Pulsatile stimulation determines timing and specificity of NF-κB-dependent transcription. *Science* **324**, 242-246 (2009).

154. Ito-Kureha, T. *et al.* The function of WTAP in N6-adenosine methylation of mRNAs controls T cell receptor signaling and survival of T cells. *Nat Immunol* **23**, 1208-1221 (2022).

155. Vasanthakumar, A. *et al.* The TNF Receptor Superfamily-NF-κB Axis Is Critical to Maintain Effector Regulatory T Cells in Lymphoid and Non-lymphoid Tissues. *Cell Rep* **20**, 2906-2920 (2017).

156. Oh, H. *et al.* An NF-κB Transcription-Factor-Dependent Lineage-Specific Transcriptional Program Promotes Regulatory T Cell Identity and Function. *Immunity* **47**, 450-465 (2017).

157. Grinberg-Bleyer, Y. *et al.* NF-κB c-Rel Is Crucial for the Regulatory T Cell Immune Checkpoint in Cancer *Cell* **170**, 1096-1108 (2017).

158. Rahman, M. K. *et al.* The Pathogen Recognition Receptor NOD2 Regulates Human FOXP3 + T Cell Survival. *J Immunol* **184**, 7247-7256 (2010).

159. Ono, M. Control of regulatory T-cell differentiation and function by T-cell receptor signalling and Foxp3 transcription factor complexes. *Immunology* **160**, 24-37 (2020).

160. Lubrano di Ricco, M. *et al.* Tumor necrosis factor receptor family costimulation increases regulatory T-cell activation and function via NF-κB. *Eur J Immunol* **50**, 972-985 (2020).

161. Zhou, J. *et al.* Dynamic m^{6}A mRNA methylation directs translational control of heat shock response. *Nature* **526**, 591-594 (2015).

162. Hao, H. *et al.* *N*^{6}-methyladenosine modification and METTL3 modulate enterovirus 71 replication. *Nucleic Acids Res.* **47**, 362–374 (2019).

163. Paris, J. *et al.* Targeting the RNA m^{6}A Reader YTHDF2 Selectively Compromises Cancer Stem Cells in Acute Myeloid Leukemia. *Cell Stem Cell* **25**, 137-148 (2019).

164. Pinna, F. *et al.* A20/TNFAIP3 Discriminates Tumor Necrosis Factor (TNF)-Induced NF-κB from JNK Pathway Activation in Hepatocytes. *Front Physiol* **8**, 610 (2017).

165. Nelson, D. E. *et al.* Oscillations in NF-κB signaling control the dynamics of gene expression. *Science* **306**, 704-708 (2004).

166. Einstein, J. M. *et al.* Inhibition of YTHDF2 triggers proteotoxic cell death in MYC-driven breast cancer. *Mol Cell* **81**, 3048-3064 (2021).

167. Dixit, D. *et al.* The RNA m^{6}A reader YTHDF2 maintains oncogene expression and is a targetable dependency in glioblastoma stem cells. *Cancer Discov* **11**, 480-499 (2021).

168. Zhang, C. *et al.* Reduced m^{6}A modification predicts malignant phenotypes and augmented Wnt/PI3K-Akt signaling in gastric cancer. *Cancer Med* **8**, 4766-4781 (2019).

169. Yu, J. *et al.* Histone lactylation drives oncogenesis by facilitating m^{6}A reader protein YTHDF2 expression in ocular melanoma. *Genome Biol* **22**, 85 (2021).

170. Li, Y. *et al.* RNA m^{6}A reader YTHDF2 facilitates lung adenocarcinoma cell proliferation and metastasis by targeting the AXIN1/Wnt/β-catenin signaling. *Cell Death Dis* **12**, 479 (2021).

171. Cui, Q. *et al.* m^{6}A RNA Methylation Regulates the Self-Renewal and Tumorigenesis of Glioblastoma Stem Cells. *Cell Rep* **18**, 2622–2634 (2017).

172. Chai, R. C. *et al.* YTHDF2 facilitates UBXN1 mRNA decay by recognizing METTL3-mediated m^{6}A modification to activate NF-κB and promote the malignant progression of glioma. *J Hematol Oncol* **14**, 109 (2021).

173. Karlsson, F., Robinson-Jackson, S. A., Gray, L., Zhang, S. & Grisham, M. B. Ex vivo generation of regulatory T cells: characterization and therapeutic evaluation in a model of chronic colitis. *Methods Mol Biol* **677**, 47-61 (2011).

174. Bolger, A. M., Lohse, M. & Usadel, B. Trimmomatic: A flexible trimmer for Illumina sequence data. *Bioinformatics* **30**, 2114-2120 (2014).

175. Anders, S., Pyl, P. T. & Huber, W. HTSeq-A Python framework to work with high-throughput sequencing data. *Bioinformatics* **31**, 166-169 (2015).

176. Yao, Y. *et al.* METTL3 inhibits BMSC adipogenic differentiation by targeting the JAK1/STAT5/C/EBPβ pathway via an m^{6}A-YTHDF2–dependent manner. *FASEB Journal* **33**, 7529-7544 (2019).

177. Heck, A. M., Russo, J., Wilusz, J., Nishimura, E. O. & Wilusz, C. J. YTHDF2 destabilizes m^{6}A-modified neural-specific RNAs to restrain differentiation in induced pluripotent stem cells. *RNA* **26**, 739-755 (2020).

178. Chen, M. *et al.* RNA N^6-methyladenosine methyltransferase-like 3 promotes liver cancer progression through YTHDF2-dependent posttranscriptional silencing of SOCS2. *Hepatology* **67**, 2254-2270 (2018).

179. Stowell, J. A. W. *et al.* A low-complexity region in the YTH domain protein Mmi1 enhances RNA binding. *J Bio Chem* **293**, 9210-9222 (2018).

180. Liu, J. *et al.* m^{6}A mRNA methylation regulates AKT activity to promote the proliferation and tumorigenicity of endometrial cancer. *Nat Cell Biol* **20**, 1074-1083 (2018).

181. Fei, Q., Zou, Z., Roundtree, I. A., Sun, H.-L. & He, C. YTHDF2 promotes mitotic entry and is regulated by cell cycle mediators. *PLoS Biol* **18**, e3000664 (2020).

182. Smale, S. T. & Fisher, A. G. Chromatin Structure and Gene Regulation in the Immune System. *Annu Rev Immunol* **20**, 427-462 (2002).

183. Smale, S. T. Transcriptional regulation in the immune system: a status report. *Trends Immunol* **35**, 190-194 (2014).

184. Schreiber, R. D., Old, L. J. & Smyth, M. J. Cancer Immunoediting: Integrating Immunity's Roles in Cancer Suppression and Promotion. *Science* **331**, 1565-1570 (2011).

185. Ross, C. A. & Poirier, M. A. Protein aggregation and neurodegenerative disease. *Nat Med* **10**, S10-17 (2004).

186. Xu, B., Liu, D., Wang, Z., Tian, R. & Zuo, Y. Multi-substrate selectivity based on key loops and non-homologous domains: new insight into ALKBH family. *Cell Mol Life Sci* **78**, 129-141 (2021).

187. Békés, M., Langley, D. R. & Crews, C. M. PROTAC targeted protein degraders: the past is prologue. *Nat Rev Drug Discov* **21**, 181-200 (2022).

188. Zou, Z., Sepich-Poore, C., Zhou, X., Wei, J. & He, C. The mechanism underlying redundant functions of the YTHDF proteins. *Genome Biol* **24**, 17 (2022).

189. Wei, J. & He, C. Site-specific m6A editing. *Nat Chem Biol* **15**, 848-849 (2019).

190. Li, J. *et al.* Targeted mRNA demethylation using an engineered dCas13b-ALKBH5 fusion protein. *Nucleic Acids Res* **48**, 5684-5694 (2020).

191. Wilson, C., Chen, P. J., Miao, Z. & Liu, D. R. Programmable m6A modification of cellular RNAs with a Cas13-directed methyltransferase. *Nat Biotechnol* **38**, 1431-1440 (2020).

192. Percharde, M. *et al.* A LINE1-Nucleolin Partnership Regulates Early Development and ESC Identity. *Cell* **174**, 391-405 (2018).

193. Bai, R. *et al.* Mechanisms of Cancer Resistance to Immunotherapy. *Front Oncol* **10**, 1290 (2020).

194. Yang, S. *et al.* m^6A mRNA demethylase FTO regulates melanoma tumorigenicity and response to anti-PD-1 blockade. *Nat Commun* **10**, 2782 (2019).

195. Wang, L. *et al.* m^6A RNA methyltransferases METTL3/14 regulate immune responses to anti-PD-1 therapy. *EMBO J* **39**, e104514 (2020).

196. Shang, S. *et al.* The role of neoantigens in tumor immunotherapy. *Biomed Pharmacother* **151**, 113118 (2022)